UNIVERSITÀ DEGLI STUDI DI TRIESTE

XXVII CICLO DEL DOTTORATO DI RICERCA IN

NANOTECNOLOGIE

NANOTECHNOLOGY AND BIOMATERIALS IN OPHTHALMIC SURGERY

Settore scientifico-disciplinare: MED/30

DOTTORANDO
PAOLO CECCHINI

COORDINATORE
CHIAR.MA PROF. LUCIA PASQUATO

SUPERVISORE DI TESI
CHIAR.MO PROF. DANIELE TOGNETTO

ANNO ACCADEMICO 2014 / 2015

Contents

1. Glaucoma

Introduction

Glaucoma is one of the leading causes of irreversible blindness worldwide, with an estimated 64.3 million people affected globally in 2013.[1] From the late 19th until the last quarter of the 20th century, glaucoma was defined as "pressure within the eye higher than the statistical normal of the population".[2] It was believed that this elevated intraocular pressure (IOP) would induce a damage to the optic nerve, which would eventually cause blindness if left untreated.[3] The American Academy of Ophthalmology now defines glaucoma as "a group of diseases with certain features including an intraocular pressure that is too high for the continued health of the eye".[2] The glaucomatous optic neuropathy is a distinct type of optic nerve damage characterized by increasing cupping of the optic nerve disc. The disease eventually leads to a progressive and irreversible loss of visual function, resulting in blindness. Nowadays, early detection and treatment may prevent serious vision loss.[4,5]

On a histological level, early glaucomatous cupping consists of loss of axons, blood vessels and glial cells. The loss of tissue seems to start at the level of the lamina cribrosa. It is most pronounced at the superior and inferior poles of the optic disc. Structural optic nerve changes may precede detectable functional loss. In advanced glaucoma forms tissue destruction extends behind the cribriform plate and the lamina bows backward.[4,5]

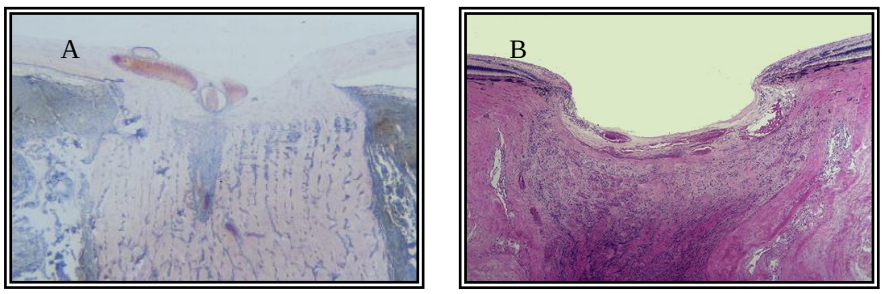

Figure 1. Histology of normal (A) and glaucomatous (B) optic nerve head

The optic nerve head appears excavated and undermined and for this reason it has been likened to a bean pot (Figures 1 and 2).

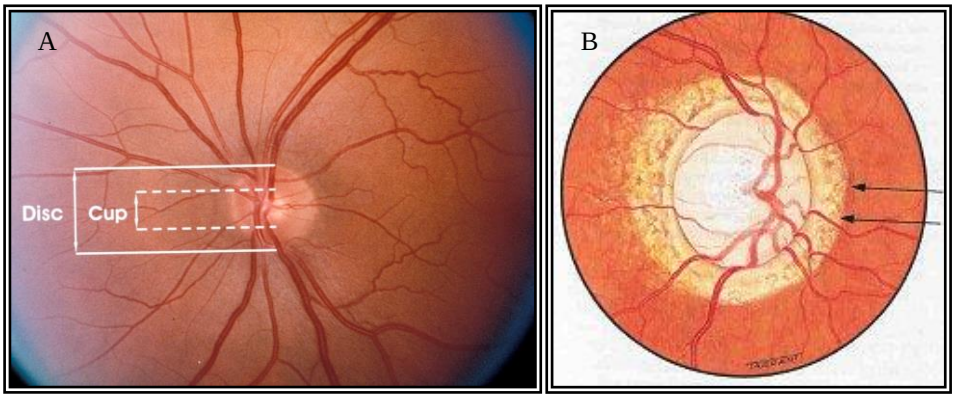

Figure 2. Normal (A) and glaucomatous (B) optic nerve head. Note the cupping of the optic disc in (B).

The glaucomatous cupping in infants and children is accompanied by an expansion of the entire scleral ring (buphthalmus).

Several studies have shown that the intraocular pressure (IOP) is one of the major risk factors for the optic nerve damage.[3] Intraocular pressure is a balance between the production of aqueous humor by the ciliary processes of the eye and its drainage through the trabecular meshwork of the irido-corneal angle (Figure 3). The production rate of the aqueous humor is about 2–3 μL/min and has a turnover time of 1.5-2 hours. The aqueous humor composition is water for over the 99%. The aqueous humor flows from the ciliary processes into the posterior chamber and subsequently through the pupil into the anterior chamber. A structure named trabecular meshwork drains the aqueous humor via Schlemm's canal into scleral plexuses and eventually into the general blood circulation.[6,7]

High IOP values even if strongly related to glaucoma onset, are neither necessary nor sufficient to induce the neuropathy. There is a dose-response relationship between the intraocular pressure and the risk of damage to the visual field. Not every person with increased intraocular pressure will develop glaucoma. Some people can tolerate higher levels of IOP better than others. In addition, a certain level of intraocular pressure might be high for one person but normal for another.[8-10]

The development of glaucoma depends on the pressure level the optic nerve can tolerate without being damaged. This level is different for each person.[8-10] The corneal thickness is a fundamental element to be considered.[11,12] Normal central corneal thickness is in the range of 545 – 550μ. The variability of corneal thickness in the population may introduce a bias in the correct IOP measurement. Eyes with thicker corneas than normal may have

IOP overestimated. Similarly, eyes with thinner than average corneas may have IOP underestimated. In addition there are several other risk factors[13] for glaucoma development:

- African Americans over age 40
- People over age 60, especially Mexican Americans
- Family history of glaucoma
- Myopia
- Shallow anterior chamber
- Systemic low blood pressure
- Other vascular defects at the optic disc microcirculation

Unfortunately, lost vision from the disease cannot be restored.

Its most prevalent form, primary open-angle glaucoma,[14] can be insidious. A significant proportion of individuals, in fact, may remain either undiagnosed or undertreated since quality of life is not significantly affected until the later stages of the disease process. Glaucoma usually begins in midlife and progresses slowly but relentlessly. If detected early, the disease progression can frequently be arrested or slowed down with drug and/or surgical treatment. A greater awareness of the deterioration of the optic nerve and/or of the visual field could prevent further damages. Early diagnosis and treatment are essential in order to reduce the progression and have a positive impact on the natural evolution of the disease.

Classification

Many classifications of glaucoma are available. Glaucoma may be classified on the basis of clinical evidence, genetics, site of damage and etiology. One of the most commonly accepted classifications is to divide glaucoma into primary or secondary forms:

I Primary

A. Congenital
B. Childhood glaucoma
C. Adult (common types)
    1. Open angle

2. Narrow angle or angle closure
3. Normal tension glaucoma

II Secondary

A. Inflammatory
B. Traumatic
C. Rubeotic
D. Phacolytic
E. Steroid induced
F. Pigmentary
G. Pseudoesfoliation (PSX)

The most common types of glaucoma are the primary open angle (POAG) and primary angle closure glaucoma (PACG).[14]

In *open-angle glaucoma*, even though the drainage angle is "open", the fluid passes too slowly through the trabecular meshwork drainage (Figure 3). It is worth to remember that POAG is totally asymptomatic, especially at an early stage. It causes no pain and vision is normal. Since the fluid builds up, the pressure inside the eye rises to a level that may damage the optic nerve. When the optic nerve is damaged, irreversible visual field defects occur, with consequent vision loss. Glaucoma can develop in one or in both eyes. Usually the second eye is affected at a later stage and the disease progresses unevenly within the two eyes. Without treatment, glaucomatous patients will slowly lose their peripheral vision, may experience difficulties in seeing objects on their side and eventually only a tunnel shaped central vision remains.

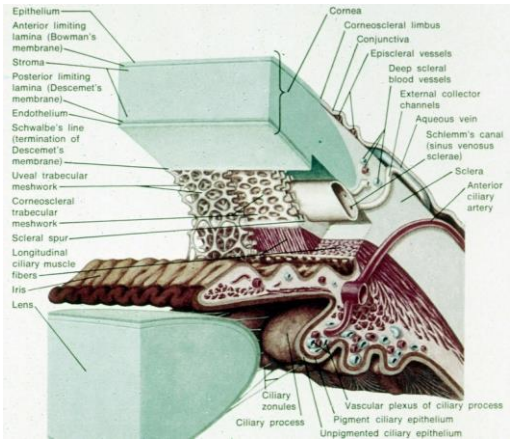

Figure 3. Irido-corneal angle

Immediate treatment for early-stage POAG can delay the progression of the disease. For this reasons, early diagnosis is critical.[14]

In *low-tension or normal-tension glaucoma* (NTG), the optic nerve and visual field defect arise in people with normal eye pressure. It is believed that in NTG a disrupted perfusion

may occur, with nighttime low blood pressure and low ocular blood flow. Some of the NTG patients benefit from an IOP lowering of at least 30%. On the contrary, other NTG patients may worsen despite low IOP values. A comprehensive medical history is important to identify other potential risk factors, such as low blood pressure, that may contribute to low-tension glaucoma. If no risk factors are identified, treatment options for NTG are similar to those for POAG.[15-17]

In *angle-closure glaucoma*, the aqueous humor cannot drain through the irido-corneal angle and leave the eye. The angle gets blocked by the outer edge of the iris that bunches up and covers the irido-corneal angle. This happens usually when the pupil enlarges, especially in darkness. People with this type of glaucoma may experience a sudden increase in the eye pressure. Symptoms include severe pain and nausea, as well as redness of the eye and blurred vision. Usually, medical therapy and prompt laser treatment can clear the blockage, lower the eye pressure, and restore vision.[18]

In *congenital glaucoma*, children were born with a defect in the angle of the eye that slows the normal drainage of the fluid. These children usually have obvious symptoms, such as cloudy eyes, sensitivity to light and excessive tearing. Surgery is the suggested treatment, since medications are not effective, can cause serious side effects and may be difficult to administer to children. If surgery is promptly performed, these children usually have a reasonable chance of having good vision.[19]

Secondary glaucoma can develop as a complication of other medical conditions. For example, a severe form of glaucoma, called *neovascular glaucoma*, can result from poorly controlled diabetes or from a central retinal vein occlusion. Other types of glaucoma sometimes occur due to hypermature cataracts, certain eye tumors, or ocular inflammations such as uveitis. Sometimes glaucoma develops after ocular surgery or serious ocular injuries. Steroid drugs used to treat eye inflammations and other diseases can trigger glaucoma in some people.

Finally, there are two eye conditions known to cause secondary forms of glaucoma.[20]

Pigmentary glaucoma occurs when pigment from the iris sheds off and blocks the trabecular meshwork, slowing fluid drainage.

Pseudoexfoliation glaucoma occurs when a whitish material, produced from the internal eye structures, sheds off, blocks the trabecular meshwork and slows down the fluid drainage.

Depending on the cause of these secondary glaucomas, treatment includes eye drops, laser surgery, or conventional surgery.[21]

Diagnosis

Glaucoma is detected through a comprehensive eye examination that includes:

- **Tonometry**. It is the measurement of intraocular pressure. The diurnal fluctuation is normally < 6 mmHg.

  There are different techniques to measure the intraocular pressure. The gold standard is the Goldmann applanation tonometry. Applanation tonometry is based on the Imbert-Fick principle, which states that the pressure inside an ideal sphere equals the force necessary to flatten its surface divided by the area of flattening (P = F/A, where P = pressure, F = force and A = area). In applanation tonometry, the cornea is flattened and the IOP is determined by varying the applanating force of the area flattened.[22] As stated earlier,[11,12] measures can be affected by the central corneal thickness, as the Goldmann tonometer was designed taking into consideration a population based central corneal thickness of 520 microns. The tonometer measures the force necessary to flatten an area of the cornea of 3.06mm diameter. The IOP, expressed in mmHg equals the flattening force, expressed in grams, multiplied by 10. Fluorescein dye is placed in the patient's eye to highlight the tear film. A split-image prism is used such that the image of the tear meniscus is divided into a superior and an inferior arc. The intraocular pressure is taken when these arcs are aligned such that their inner margins touch.

  Other tonometry techniques include the non-contact air puff tonometry, indentation tonometry and the recently introduced rebound tonometry.
- **Fundus oculi**. The exam is carried out at the slit lamp, which allows a comprehensive examination of the eye and the optic nerve, revealing possible signs of damage.
- **Visual field test.** This test measures the peripheral (side vision) and permits to study possible loss of peripheral vision.
- **Pachymetry**. It is the measurement of the cornea thickness, expressed in microns.

The optic nerve head and the retinal nerve fiber layer (RNFL) are the sites of clinically detectable glaucomatous tissue damage.[23] Photographic techniques are used to document the optic disk and the RNFL and to monitor patients with suspected primary open-angle glaucoma or to follow-up patients already suffering from the disease.

New techniques such as laser scanning tomography, scanning laser polarimetry, and optical coherence tomography have been introduced to quantify structural alterations with the aim of early detection of optic nerve or RNFL damage prior to functional loss. These novel, additional diagnostic tools are currently being evaluated in the clinical practice. Imaging and computed data processing allow for three-dimensional in vivo measurements in the range of micrometers. With regard to the structure of the optic nerve head, the evaluation of the optic disk can be based on quantitative topographic data. However, computed parameter readings should always be evaluated in a clinical context.

The goal is to improve, combine, and integrate all the different diagnostic approaches to improve patient care.

Treatment

The decrease in quality of life associated with glaucoma may occur earlier than previously thought, emphasizing the importance of early diagnosis and treatment.

The main goal of treatment in glaucoma is to lower the IOP. Therapies include medical, laser, and surgical interventions. Surgery is typically reserved for cases of progressive disease or at serious risk of progression due to uncontrolled intraocular pressure.[4]

Eye drops are the most common early treatment for glaucoma. They have different mechanisms in lowering intraocular pressure and they act on different intraocular sites. Some medicines reduce the aqueous humor production, others increase the fluid drainage from the eye, via the Schlemm´s canal or via the suprachoroidal pathways.[4]

In patients with glaucoma, long-term medical therapy leads to critical modifications of ocular surface structures and adnexa, including the conjunctiva, conjunctiva-associated lymphoid tissue, cornea, Meibomian glands, eyelids, and periocular skin.[24] Drops may cause stinging, burning, and redness of the eyes. Therefore, it is mandatory to use the fewest medications, with the minimum side effects. There are many types of drugs available in the market. The first line approach is to prescribe a prostaglandin analogue in mono-therapy. The mechanism of action is believed to be the increasing of aqueous humor drainage via the uveo-scleral pathway.[4] One of the advantages of prostaglandin analogue drugs is the once-a-day administration, thus improving the patient compliance. However, they can cause local adverse effects such as conjunctival hyperemia, elongation and darkening of eyelashes, loss of orbital fat (prostaglandin-associated periorbitopathy), iris darkening and periocular skin pigmentation.

The second most used class of drugs is the β-blockers. β-blockers need to be administered twice-a-day and they act on the adrenergic receptors. They reduce the aqueous humor production. They are contraindicated in case of asthma, history of chronic pulmonary obstructive disease or bradycardia.

Other drug classes used in glaucoma therapy include the α-adrenergic agonist and the carbonic anhydrase inhibitors.

Laser treatment

Argon laser trabeculoplasty (ALT) is a technique introduced by Wise and Witter[25] as a non-surgical strategy to lower the IOP in POAG. The ALT mechanism of action is still under debate. The mechanical theory affirms that ALT causes focal scarring of trabecular beams by means of thermal burns directed towards the trabecular meshwork, thus creating spaces through which the aqueous humor can flow more easily. Other authors believe in a chemical and biological role of inflammatory cytokines that may induce structural changes in the adjacent epithelial cells of the untreated areas. The effect of this mechanism would produce a different composition of extracellular matrix with improved outflow.[26]

In 1998, selective laser trabeculoplasty (SLT) was introduced by Latina et al.[27] The main difference is that the effect is achieved using a non-thermal laser,[28-30] without causing visible damage to the trabecular meshwork.[31]

The ideal candidate to AST or ALT is a phakic elderly patient with pigmented trabecular meshwork, in a clearly visible open angle. In the best scenario, there is an IOP reduction of 25-30% one year after ALT. The effect fades over time, at an estimated rate of about 10% per year. The advantage of SLT is that it can be repeated, since it does not induce permanent damages to the trabecular meshwork.[32]

Surgical treatment

Trabeculectomy represents the next step in the management of glaucomatous patients, when eye drops or laser treatment fail to control IOP. Trabeculectomy is the gold standard of the so-called filtering procedures.[33-35]

Trabeculectomy is suitable for most types of glaucoma. It is essential that the conjunctiva is intact without scarring processes.

The aim of trabeculectomy is to create a small opening in the anterior chamber angle to allow drainage of the aqueous fluid to the conjunctival venous vessels (Figure 4). After a conjunctival peritomy, a small 4x4mm incision is performed on the sclera. A partial thickness scleral flap is sculpted up to the clear cornea. Subsequently, the surgeon cuts a small hole into trabecular meshwork. The aqueous humor is now able to freely flow through the scleral flap into the sub-conjunctival space. The scleral flap is then closed with stitches. The position and the tightness of the stitches depend on the surgeon personal preferences. Most of time two to five stitches are applied. The fluid is supposed to filter underneath the sclera after its closure. Finally, the overlying conjunctival tissue is closed with stitches to allow the formation of a so-called "filtering bleb" which is an elevation of conjunctival tissue induced by the aqueous fluid. The preferential site of surgery is the superior portion of the eye. The upper lid, therefore, covers the bleb and protects the surgical area. The fluid from the filtering bleb is eventually absorbed by the conjunctival and episcleral blood vessels.

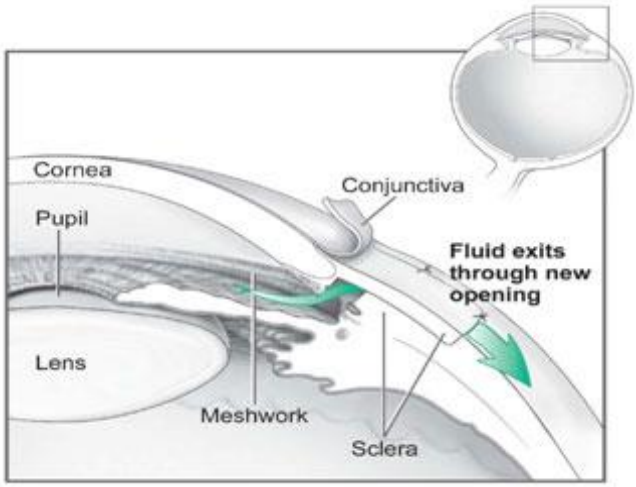

Figure 4. Trabeculectomy scheme

From the late 80's, chemotherapeutic and anti-metabolite drugs have been introduced in order to prevent failure due to bleb scarring.[36] These drugs are used to decrease the amount of tissue healing. The most commonly used drugs are 5-fluorouracil and Mitomycin C. Mitomycin C is usually applied during surgery as a 2% solution on the sclera for 2 minutes. 5-fluorouracil is often injected in the bleb postoperatively.

The surgery is performed under local anesthesia. Traditionally, a retrobulbar (behind the eye) anesthetic injection is used for local anesthesia. This involves injecting a small amount of anesthetic behind the eye under light intravenous sedation. However, it can occasionally be associated with serious complications such as hemorrhage (bleeding) or even perforation of the eye. In certain collaborating patients, a topical (eye drops) anesthesia can be used to perform trabeculectomy rather than the retrobulbar anesthesia. The advantages of the topical anesthesia are a quicker visual recovery and a decreased risk

associated with retrobulbar injection. Postoperatively, the recovery period is between 6-8 weeks. The post-operative follow-up is critical for a positive outcome of surgery. The success of the surgery strictly relies on the rate and extent of conjunctival healing and correct bleb formation. If the IOP is too low, the surgeon may reduce the amount of anti-inflammatory (or steroid) medications to allow additional healing process. If the pressure is high with evidence of a cystic bleb, a needling can be performed. A small gauge needle is used to fracture the scar tissue in the bleb in order to achieve a better filtration of the aqueous humor. The procedure is performed at the slit lamp under topical anesthesia.

The success rate of a trabeculectomy is approximately 65-70%. During the first months postoperatively the failure rate is about 10-15%. The main cause of failure is excessive scarring of the conjunctival tissue. This determines a decreased filtration of the aqueous fluid out of the eye.[33-35]

On the other hand, more rarely, the IOP may be too low, causing ocular hypotony. This event is due to the excessive filtering of the aqueous fluid or a leaking wound. Clinically a shallow anterior chamber is observed, associated with choroidal effusion or intraocular bleeding. If there is no spontaneous resolution, additional surgery may be required to drain the blood or to add additional stitches to the sclera flap or to the conjunctival bleb. The most scaring complication is the infection of the bleb, which may lead to endophthalmitis, a sight threatening infection of the eyeball. Endophthalmitis can seriously compromise vision and even the integrity of the eye itself.

While being the gold standard glaucoma procedure, trabeculectomy is not a simple technique and cannot be used in every patient.[37] Other approaches have been developed. Many of them rely on the implantation of some sort of drainage or filtering device.[38, 39]

Two main categories of implants are available. The first type is the valved implant, while the second is the non-flow-restrictive or “tube” device. The supposed advantage of the valved type of implant is the reduction of postoperative hypotony thanks to a sort of resistance to the aqueous outflow.[40]

The most commonly used valved device is the Ahmed glaucoma valve. The most widespread tube implants are the Baerveldt glaucoma implant and the Molteno implant.

It is difficult to determine, at this time, whether there are differences in success rates with different implant designs and future direct comparisons of those implants are needed.

Those surgical devices are usually implanted in intractable or advanced glaucomas with high IOP and in eyes with silicone oil tamponade. It is difficult to evaluate their success

rate due to few comparative studies available and to the advanced glaucoma stage (with critical eye condition) at which they are usually implanted. The design, material, and manufacturing quality are still under debate and biocompatibility is still an issue.

New devices

More recently, miniaturized devices have been developed, in order to achieve a minimally invasive glaucoma surgery, with fewer side effects and more reliable and consistent outcomes. The Ex-Press and the I-Stent devices are the most commonly used implants in modern minimally invasive glaucoma surgery. By far the Ex-Press glaucoma shunt appears to be the most interesting and efficient approach to filtering surgery.

The Ex-Press device has become an alternative to the traditional trabeculectomy since 2002 when was approved by the United States Food and Drug Administration.

It is a stainless steel, medical-grade, non-valved filtration device designed to shunt the aqueous humor from the anterior chamber to a subconjunctival filtration bleb. The device is 2.64mm in length and is available with either a 50 or 200μm internal lumen size.

This mini shunt is preloaded on a specially designed disposable introducer, the Ex-Press Delivery System (EDS), that helps to maintain the right orientation of the device during the implantation procedure. The Ex-Press models available are R-50, P-50 and P-200.

Originally it was designed to be placed directly underneath the conjunctiva. The success rate of this procedure was limited by serious complications such as conjunctival erosion, extrusion and ocular hypotony.[41,42] To overcome those important limitations, the Ex-Press device was implanted underneath a partial-thickness scleral flap, similarly to standard trabeculectomy.[43] The placement under the scleral flap has been widely adopted and is now the recommended technique.[44,45] Undoubtedly, using the mini glaucoma device is surgically simpler compared to trabeculectomy.[43] While trabeculectomy consists of the manual removal of a small fragment of trabecular meshwork, the Ex-Press device is positioned through an opening created with a 25-gauge needle. This approach is more straightforward and may be associated with more reproducible results. The procedure is simpler and more standardized, which may be beneficial for those surgeons who do not routinely perform glaucoma surgery.

In a retrospective study Maris et al.[35] found higher rates of complications in trabeculectomy versus the Ex-Press implantation such as early hypotony and choroidal detachments.

Anyway, many studies[39,46] in literature reported Ex-Press device-related late complications due to shunt malposition or dislocation, iris irritation and development of cataract. In addition cases of mini shunt explantation were described.[35,47]

Biocompatibility of the device was first demonstrated in rabbit eyes, with little to no inflammation found on histopathological examination.

To the best of our knowledge, few data are available regarding the structure, chemical composition, clinical behavior and biocompatibility of the Ex-Press mini glaucoma shunt.

The aim of the research project is to characterize the microscopical structure of the device, to analyze its hydrodynamics features and to improve its biological behavior by means of nanotechnology.

2. Aim of the thesis

The objectives of the present PhD thesis are:

1. Characterize the physical and chemical properties of the Ex-Press glaucoma shunt.
2. Create computational models to describe the aqueous flow through the shunt and under the scleral flap by using a finite element model.
3. Study the cell and bacteria adhesion on the surface of the device.
4. Develop different nanocoatings with possible biological activities.
5. Characterize the nanocoatings.
6. Analyse the possible biological effects of the nanocoatings in vitro.

3. Physical and chemical characterization

Little is known about the physical and chemical characteristics of the Ex-Press glaucoma shunt. The manufacturer claims it is made of high quality biomedical stainless steel (SS) 316LVM. The device is 2.64 mm in length and the inner lumen diameter is 200 or 50 μm (manufacturer data).[43]

Scanning electron microscopy (SEM) was performed. Analysis was conducted using a Quanta250 SEM (FEI, Oregon, USA) operated in secondary electron detection mode. Increasing enlargement magnifications from 50 to 5000x were used. The working distance and the accelerating voltage were adjusted in order to obtain the suitable magnification. Figures 5-9 show the dimensional characteristics of the shunt, model P-200.

The shunt appears as a tube with two front openings of 200μm. The first is at the very end of the shaft, oblique and oval in shape. The second one is close to the end but within the tube and it faces up. It is squared in shape, as seen from above, and curved as a half circle, notching the tube, as seen from the side. This is designed as a relief port that should provide an alternative pathway for aqueous humor in case of occlusion of the axial lumen due to iris apposition, fibrin or blood clogs. Opposite to the second opening there is a spur. On the opposite side there is a backplate with a vertical channel designed to enhance the posterior flow of aqueous humor. The spur prevents extrusion of the device and the flat external backplate prevents intrusion. The backplate and the spur are designed to conform to the angle anatomy and the distance between them approximates the scleral tract made by the device.

The surface appears to be smooth and well polished, while conversely and unexpectedly the inner lumen appears to be very rough, with a repetitive pattern. This feature is likely to be linked to the manufacture procedure. The pattern is around 8-9μm in width and a couple of μm in height.

The shunt is a non-valved device, meaning that the flow is not regulated by any system, but depends only on the differential pressures at its openings.

In order to verify this statement, the device was cut into two parts (Figure 10). The procedure required a peculiar handling of the Ex-Press due to the small dimensions and its particular geometry.

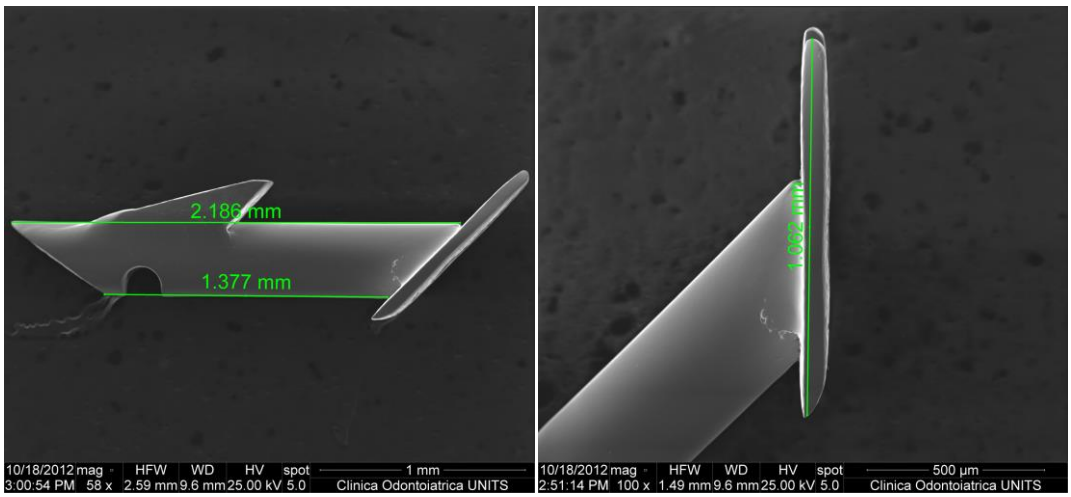

Figure 5. Dimensions of the Ex-Press glaucoma shunt

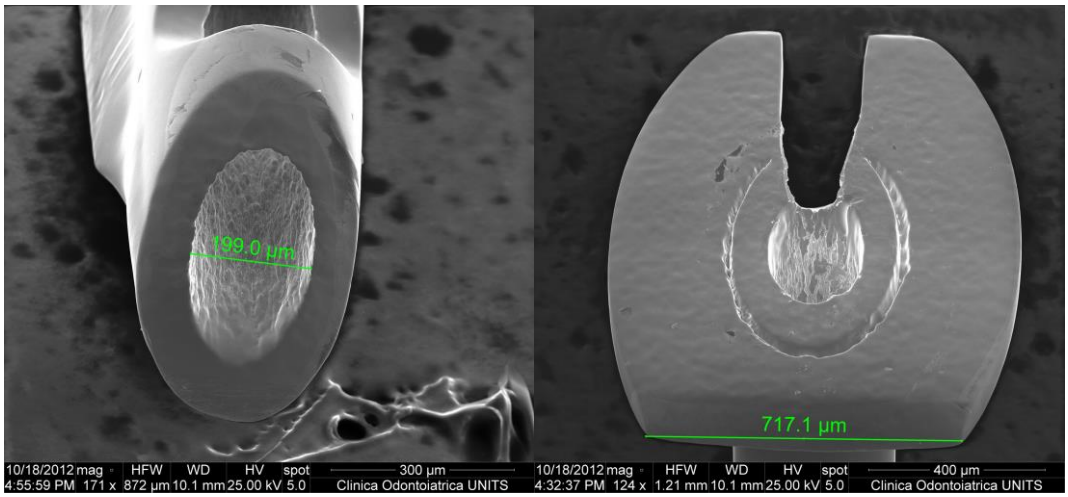

Figure 6. Inner and outer features of the Ex-Press glaucoma shunt

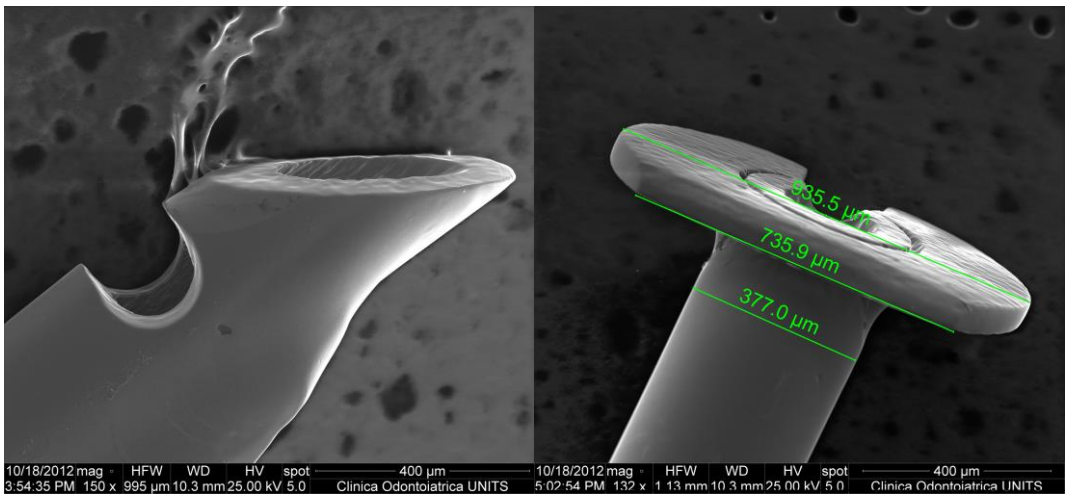

Figure 7. Front openings and backplate of the Ex-Press glaucoma shunt

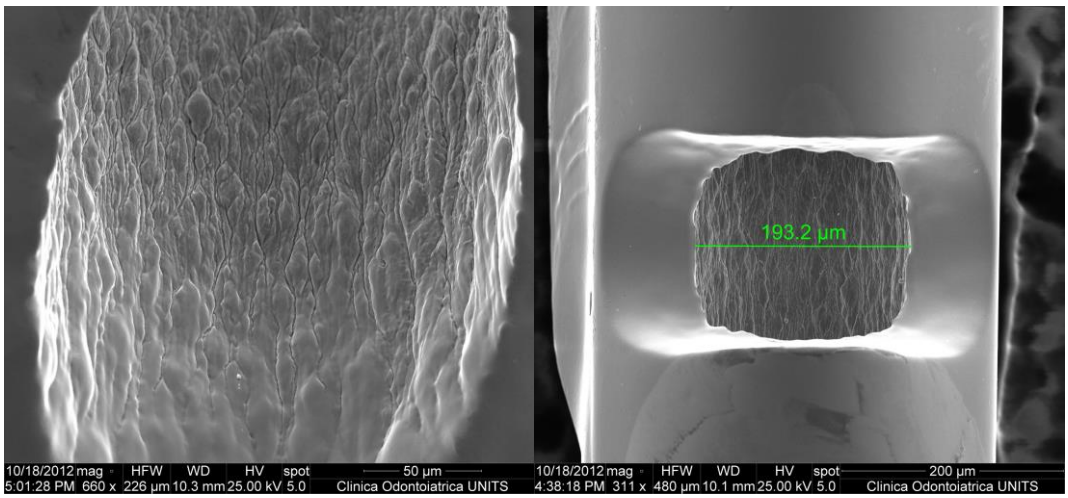

Figure 8. Internal roughness and dimension of the second opening of the Ex-Press glaucoma shunt

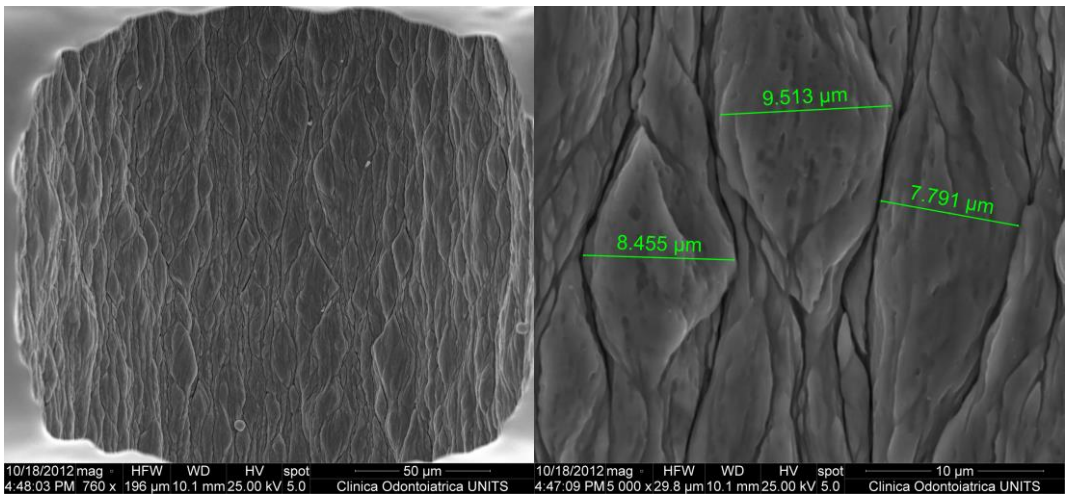

Figure 9. Internal roughness at progressively higher magnifications of the Ex-Press glaucoma shunt

The shunt was immerged and included in an epoxy resin matrix. When solid, the bloc of resin was abraded till half of the device was removed. The next step was to eliminate the resin debris from the inside of the device, which was achieved by chemical (acetone) and mechanical processes. A perfect "half pipe" was obtained. It had not been possible to fully remove the resin from the inside of the tube. Nonetheless, the evidence was that the diameter of the device was constant and that the roughness pattern was similar throughout the device. No evidence of any sort of valves or flow control systems was observed.

Postoperative inflammation and scarring after implantation are an index of the biocompatibility of the implant and may give an indication of long-term success rate. The biocompatibility of the Ex-Press device was established in rabbit models.[48,49]

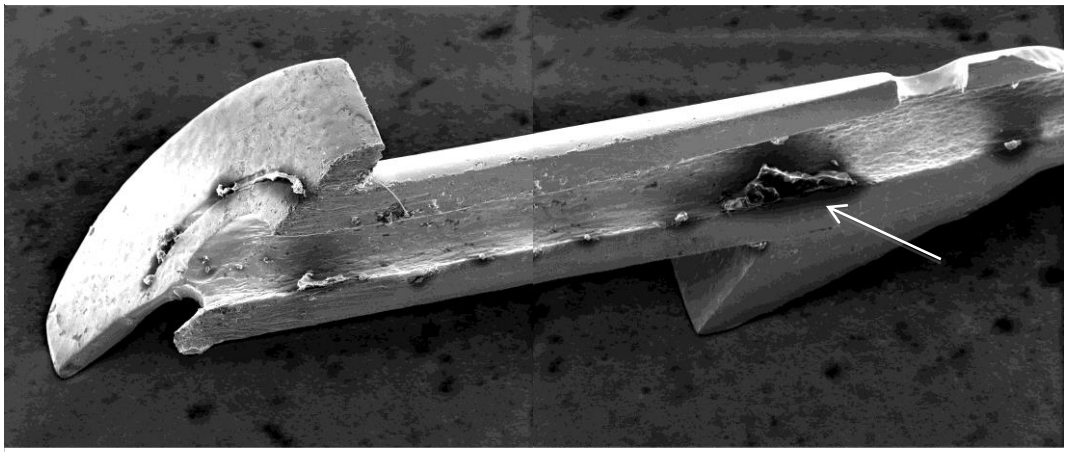

Figure 10. Ex-Press glaucoma shunt. Note the absence of valve systems. The arrow indicates resin debris

The device was implanted in the anterior chamber at the corneo-scleral junction in one eye of white New Zealand rabbits while the other eye served as a control in each of the animals. Histopathological evaluation was carried out at 3 and 6 months post implantation and it found no evidence of active inflammation and the lumen was patent in all samples at both time points. A thin, mature, fibrotic capsule of less than 0.04 mm thickness of fibroblastic nuclei without any inflammatory cells was noted in most cases; it covered up to 25% of the implant's outer surface area with the lumen remaining devoid of any obstruction in all cases.[49] There was no evidence of pathological reaction at 3 or 6 months in any ocular tissue within the proximity of the device (cornea, limbus, sclera, iris, lens, vitreous body) nor in any ocular tissues distant from the device (choroid, retina). All tests were undertaken in rabbits, which are a suitable model due to the greater fibrin formation and cellular proliferation in the rabbit eye compared to the human eye. As such, the low-grade reaction in this rabbit model bodes favorably for application to human eyes. Similar biocompatibility results were observed in humans after Ex-Press implantation.[50-51]

Nonetheless, the SS material, associated with the observed roughness of the surface, may be a good substrate for cells and bacteria adhesion. Since some postsurgical failures are believed to occur due to fibroblast proliferation, which eventually would obstruct the lumen, it was of interest to study the cells adhesion in vitro.

4. Cells and bacteria adhesion

Medical grade stainless steel 316L (SS 316L) has been widely used as a biomaterial due to its corrosion resistance and very good mechanical properties.[52] It is employed in many medical devices such as guide wires, orthopedic implants, and most commonly in the manufacture of vascular stents. Stents are used after angioplasty, a surgical method to clear the narrowing of the arteries, to prevent the re-closure of the artery. Even if this process is very successful, some complications arise due to thrombosis and neointima formation on the stents, because, like most artificial materials, SS 316L also provides a good surface for non-specific protein and cell adhesion.[53-54] In such conditions a biofilm is created and bacteria excrete a protective matrix made up of proteins, DNA, carbohydrates and polysaccharides that promote surface accumulation of bacteria.[55-56] Biofilm development facilitates bacterial survival. Bacteria within biofilms are more resistant to host immune responses and to antibiotics, making biofilm-associated infections a significant therapeutic challenge.[57]

Therefore, surface chemistry that inhibits protein and cell adhesion to the substrates and minimizes the host-implant inflammatory responses is still needed.

The cell adhesion experiments were carried out using a fibroblast cell line. Much of what is known about cell locomotion comes from studies of cell migration, especially of fibroblastic cells, on rigid, planar substrate. Cell translocation occurs through lamellipodia extension and tail retraction coordinated with formation and turnover of cell adhesions. Morphologically, the most prominent sites of cell adhesion on planar surfaces are focal adhesions located beneath the cell's leading lamellipodia and in the tail region.[58-59]

Compared with planar surfaces, much less is known about cell matrix interactions in three-dimensions. Fibroblasts incubated on top of three-dimensional matrix were observed to move more rapidly in comparison with cells on planar substrate and were shown to form three-dimensional matrix adhesions.[60] When fibroblasts are placed within three-dimensional matrices, cell locomotion results in translocation of the flexible collagen fibrils of the matrix. This remodeling process resembles matrix morphogenesis during development and wound repair. A recent paper[61] reports that nanotopography controls cell behavior, such as cell adhesion and migration, by means of mechanisms still not fully

understood. In this work, a variety of nanopores was fabricated on SS 316L to investigate the effects of spatial control on the growth and function of fibroblasts and their effects on migration. It was observed that 40 and 75 nm nanopores enhanced cell proliferation, focal adhesion formation and protein expression after 24 h of incubation. In summary, the 40 and 75 nm nanopore surfaces promoted cell adhesion and migration of fibroblasts by controlling the temporal expression of integrins and other molecules.[61] The study provided insight into the improvement of the design of stainless steel implants and parameters that affect biocompatibility. In another paper[62] femtosecond laser treatment was used to generate micro-spotted lines separated by 75, 125, or 175μm wide nanostructured interlines on SS 316L plates. The laser treated plates revealed a significant improvement in adhesion of human endothelial cells and human bone marrow mesenchymal stem cells but a significant decrease in fibroblast adhesion. Another recent paper[63] reports that creating nano-pits on the surface of SS 316L improved the wettability properties as compared with the untreated SS 316L, since the contact angles dropped from 83.0° to 45.4°. Moreover, the anodized SS 316L surfaces with 50 nm and 60 nm diameter pits dramatically enhanced initial human dermal fibroblast attachment and growth for up to 3 days in culture.[63]

Many of these characteristics are seen favorably when dealing with orthopedic implants, which need to be integrated in the bone matrix, but are a dramatically relevant problem when it comes to other implants, like the coronary stents. In the case of the Ex-Press glaucoma shunt the clinical conditions resemble those of the coronary stents, a situation in which the less cell adhesion is observed, the better the biocompatibility and life span of the implant are.

From literature, therefore, it clearly appears that the microscopical topography (both on the micro and the nano-level) of the surface may affect cell adhesion and migration. The evidence of a rough surface of the lumen of the Ex-Press device strongly suggested verifying the level and the pattern of cell adhesion.

The attempts were made using an insulin needle, which, at the SEM analysis, presented an internal roughness very similar to the device. It is likely that the two tubes are made using similar manufacturing technology. Therefore insulin needle seemed to be a good model for cell adhesion on the Ex-Press device.

Since the inner lumen is very small, it had been difficult to pour cells onto it. Solutions containing 20000 cell /mL and 50000 cell /mL were used.

Tips from needles (Microlance^{TM} 3, 27G, BD Biosciences) were cut and fixed with cyanoacrylate glue at the bottom of a 6 multiwell plate (Sarstedt). Human primary fibroblasts were seeded using medium 106 plus LSGS (both from Gibco) at a concentration of 20000 cells/well using two different approaches: 1) cells were suspended at the desired concentration in 2 ml of medium and plated; 2) cells were suspended in 200 µl of medium and spotted directly on the needle, in order to force cells entering the pipe. One hour later, the missing volume of medium (1.8 ml) was added to the plate. After three days, cells were fixed with paraformaldehyde 4% in PBS for 15' at room temperature and stored at 4°C until use.

Subsequently they were analyzed at the SEM using the previously described settings. Little to no cell adhesion was observed. In the hypothesis of a mechanical difficulty in entering the small diameter inner lumen, a new strategy was developed. Instead of passively immerging the needle in the solution, the solution itself was injected into the ostium, forcing fibroblasts to enter the device. Using the same procedure previously mentioned, specimens were then analyzed at SEM. Using this strategy, which resembles what happens in vivo as the aqueous humor flows through the device carrying inflammatory cells, proteins and other molecules, cell adhesion on the surface was observed (Figure 11). Fibroblasts took advantage of the superficial irregularities and roughness, and adhered to the surface assuming the typical elongated, spindle shape.

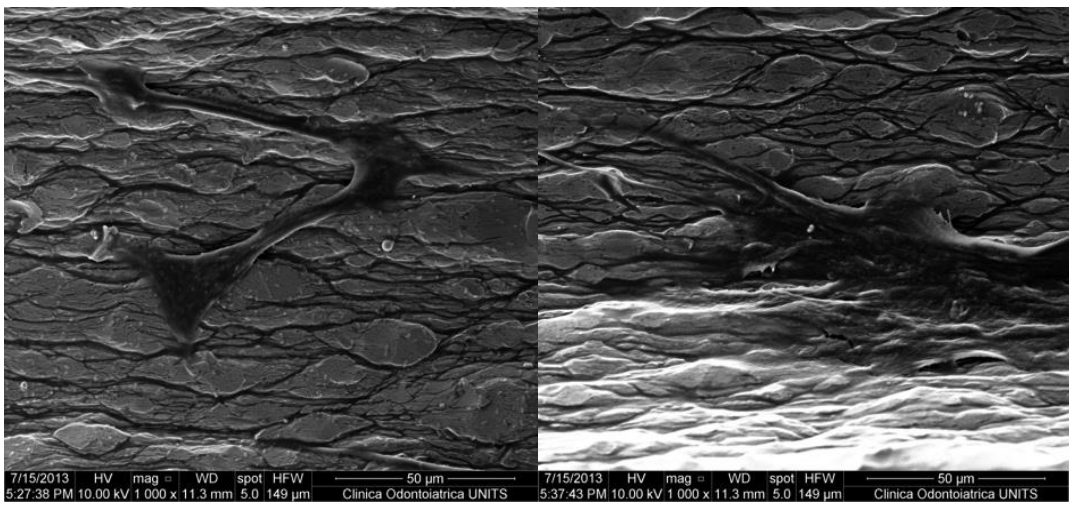

Figure 11. Fibroblasts adhesion to the inner lumen

Even if not massive, the study demonstrated a fibroblastic adhesion on SS rough surface.

It was not possible to speculate an actual clinical role of those experimental results. Further studies are needed to understand the biocompatibility of the SS316L in terms of cellular adhesion characteristics and possible clogging formation.

Interestingly, a massive bacteria contamination was observed during one of the experiments, as depicted in Figure 12.

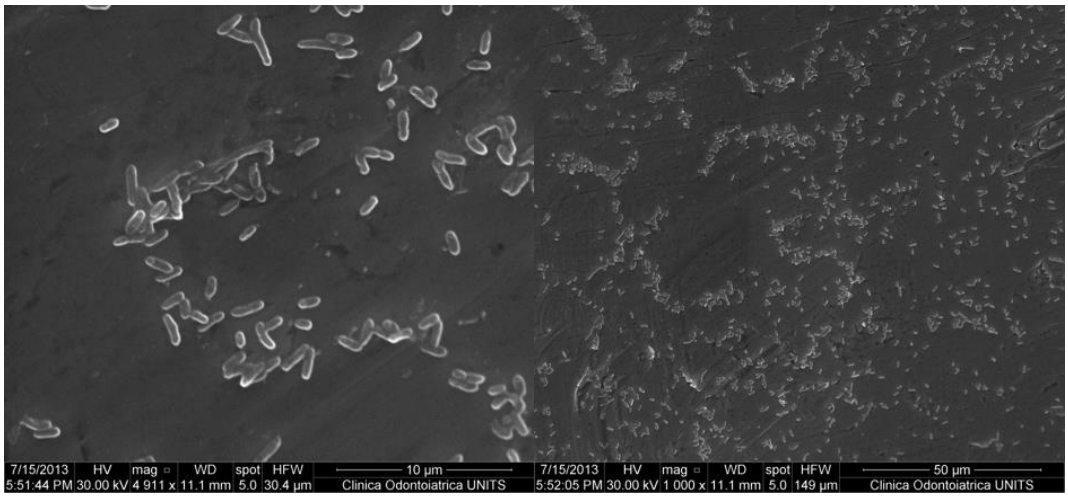

Figure 12. Bacteria adhesion to the sample

The bacteria appeared to be spread on the surface in a high-density pattern. The growth on the SS 316L is therefore fast and bacteria adhesion seems to be promoted.

5. In vivo

At the Eye Clinic of Trieste, there has been the opportunity to analyze an in vivo Ex-Press glaucoma shunt that needed to be explanted from the eye of a patient two years after surgery. The shunt was explanted due to the device extrusion initially from the scleral flap and subsequently from the conjunctiva (Figure 13). A scleral patch was used to cover and seal the area where the device was previous implanted.

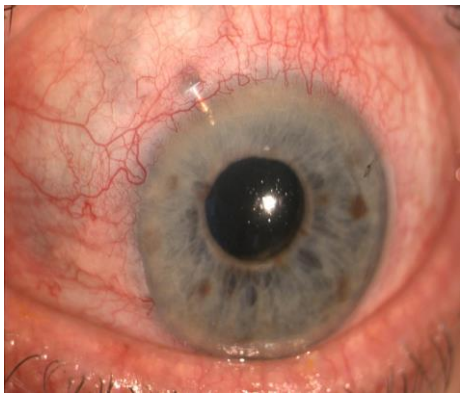

Figure 13. Extrusion of an Ex-Press shunt

To analyse the shunt by means of SEM coupled with Energy Dispersive Spectroscopy (EDS), the device was mounted on an aluminium stub that was previously covered with two sides conductive carbon adhesive tape. The specimen was then analysed by means of a Scanning Electron Microscope (Quanta 250 SEM, FEI, Oregon, USA) operated in secondary electron detection mode. Increasing enlargement magnifications from 50-1000x were used. The working distance and the accelerating voltage were adjusted in order to obtain the suitable magnification.

An EDS (EDAX Integrated GENESIS APEX 2i EDS System with Apollo X Silicon Drift Detector (SDD)) detector was used together with the SEM for elemental analysis of the sample's surface.

After explantation, images of the mini glaucoma shunt acquired by the SEM revealed the presence of small amount of debris on the device lumen (Figure 14). The device lumen appeared pervious, without major damages on its surface.

EDS analysis of the debris surface detected a peak of carbon higher than the one detected on the bare metal of the shunt (Figure 15). EDS element analyses of the device on the bare surface (left) and on the debris (right) were expressed in percentage (Figure 15).

The presence of a limited amount of debris in the lumen of the device suggested that the proliferation of cells was present but limited, thus it could hardly affect the hydrodynamics of the device and its outflow capacity. SEM images of the device obtained two years after the implantation demonstrated apparent good conditions of the tube with

small signs of extracellular matrix deposition. The surface showed, however, few superficial pits, likely due to an initial corrosion process (Figure 14).

It would be interesting to analyse the device many years after the implantation to verify the long-term biocompatibility and the extent of the corrosion.

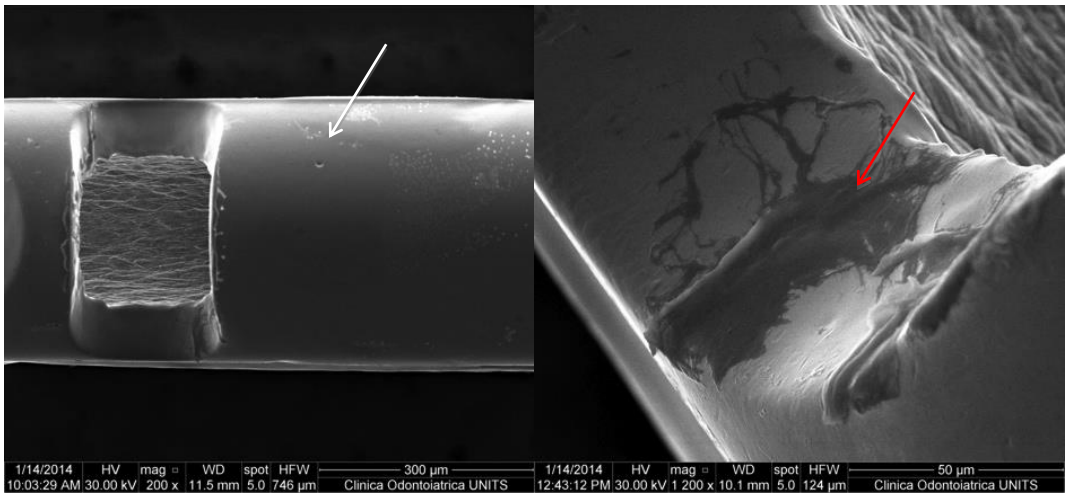

Figure 14. Corrosion pits (white arrow) and organic debris (red arrow) on the explanted shunt

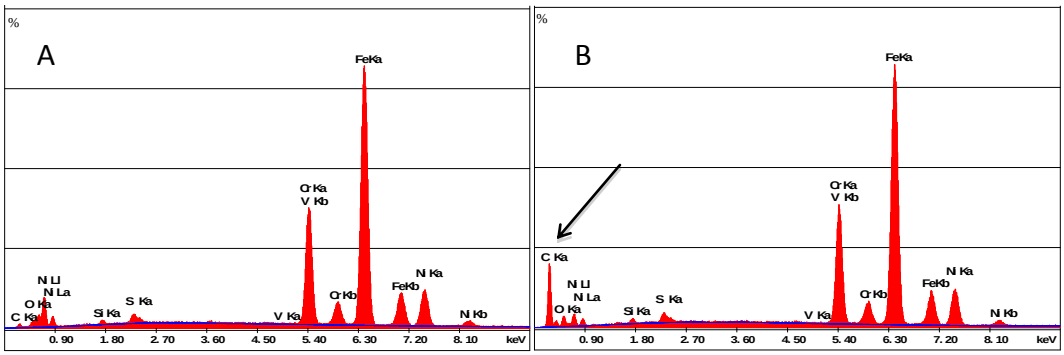

Figure 15. Energy dispersive X-ray spectroscopy of an explanted Ex-Press glaucoma shunt, (A) bare metal, (B) debris. The arrow indicates the presence of carbon when the analysis is focused on the debris (B)

6. Fluid dynamics under the scleral flap

To maintain the pressure in the eye under control when the pharmacological therapy is not sufficient, a surgical approach is needed. As described in the introduction, the ophthalmic surgeon creates a new drainage pathway for the aqueous humor to leave the anterior chamber of the eye. This is achieved by etching the sclera and obtaining a flap which functions as protection and closure of the trabeculectomy or Ex-Press glaucoma shunt implant.

The flap is usually sealed with two or more surgical stitches (Figure 16).

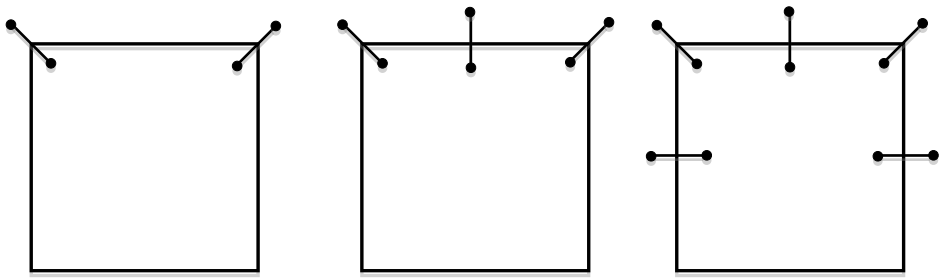

Figure 16. Typical suture positioning

Figure 17 shows the common position of the stitches (A, B). Sides AB, BC and AD are the parts of the flap engraved while the CD side remains intact and attached to the corneal limbus.

The Ex-Press glaucoma shunt is implanted in the centre of side CD and point F is schematically the site of aqueous outflow under the sclera flap. The aqueous is free to percolate under the sclera flap towards the other sides. Hydro-dynamically the problem to be resolved is a coupled fluid-structure interaction in which we can assume the scleral flap to have a membrane-like behaviour.

The hydrodynamic pattern is schematically reported in Figure 17. This part of the study has analysed the flow field under the sclera flap after Ex-Press glaucoma shunt implantation. The study takes its cue from recent observations made in vivo.

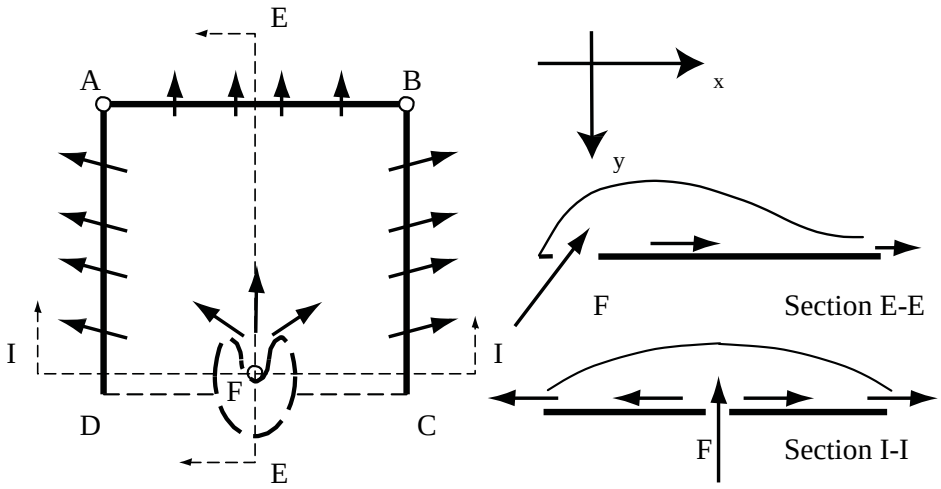

Figure 17. Pattern of trabeculectomy/Ex-Press shunt implantation: arrows indicate, in a first approximation, the flows in the gap under the sclera. The dimensions of the sides of the scleral flap are 4.0 mm

Some studies have shown the aqueous outflow routes under the sclera flap using Optical Coherence Tomography (OCT).[64-66] It has been observed that the identification of the filtering sites is difficult and that a sort of aqueous pooling may be detected. Other papers report that most of the filtration occurs on the lateral sides of the flap.[64, 67]

Model formulation

This study considers the motion of an incompressible fluid under the scleral flap after surgery. Geometric parameters are taken from literature. Table 1 shows the dimensions of the domain.

$2.5 \cdot 10^{-2}$ m	Eye radius
$4 \cdot 10^{-3}$ m	Sclera flap dimensions
$0.25 \cdot 10^{-3}$ m	Flap thickness
$10 \div 50 \cdot 10^{-6}$ m	Sclera bed thickness
$51 \cdot 10^{-6}$ m	Device lumen diameter
$6.25 \cdot 10^{-12}$ m^3/s	Aqueous outflow
$0.5 \cdot 10^{-3}$	Conjunctival thickness
28.9÷29.3 MPa m	Elastic modulus

Table 1. Dimensions of the domain for simulations

The device is considered to be positioned in the middle of side CD as reported in Figure 17. The present fluid dynamics investigation was performed numerically under steady state conditions. The Navier-Stokes equations governing the phenomena are solved to study the flow under the scleral flap.

Initially, a bi-dimensional (2D) schematization was performed. Subsequently, a more detailed and accurate three-dimensional (3D) simulation was conducted.

2D analysis of sclera flap deformation

The equation that governs the behaviour of the scleral flap is very complex. It can be referred to the theory of shells. A simplified approach was adopted to discrete with cell element method[68] (CEM), assuming a local plane stress.

The surface of the flap can be discretized into triangles as shown in Figure 18. Triangular discretization allows assuming that each triangle, under tension, remains flat and constant.

From a mechanical point of view, it is feasible to reduce the study to a plane stress analysis and to derive the stiffness matrix for each triangle in the local reference system by rotation.

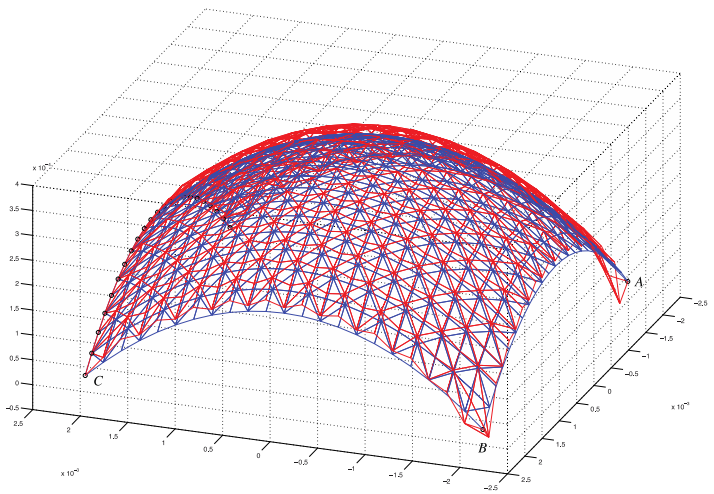

Figure 18. Discretization of the surface of the scleral flap using triangles (size in mm) taking into account the natural curvature (blue mesh). The red mesh represents the deformation of the scleral flap. The area close to the surgical stitches tends to collapse on the scleral bed

Analysis of the flow field

The flow field is represented using the Navier-Stokes equations averaged vertically, since the motion is limited to a possible elevation of the sclera flap on the z axis. No movement on the other axes (xy) is expected. The vertical movement is described by h = h(x, y). If

we assume that the flow in the z direction has a parabolic profile and the vertical velocity w (x, y, z) can be neglected, it is possible to write:

$$u = 6u_m(x,y)\left[\frac{z}{h} - \frac{z^2}{h^2}\right] \quad (1)$$

$$v = 6v_m(x,y)\left[\frac{z}{h} - \frac{z^2}{h^2}\right] \quad (2)$$

The integral with respect to z between 0 and h of the Navier-Stokes equations produces the averaged form on the vertical axis:

$$\frac{\partial hu_m}{\partial t} + \frac{6}{5}\left[\frac{\partial hu_m u_m}{\partial x} + \frac{\partial hu_m v_m}{\partial y}\right] = -\frac{1}{\rho}\frac{\partial hp}{\partial x} + v\left[\frac{\partial^2 hu_m}{\partial x^2} + \frac{\partial^2 hu_m}{\partial y^2} - \frac{12u_m h}{h^2}\right] \quad (3)$$

$$\frac{\partial hv_m}{\partial t} + \frac{6}{5}\left[\frac{\partial hu_m v_m}{\partial x} + \frac{\partial hv_m v_m}{\partial y}\right] = -\frac{1}{\rho}\frac{\partial hp}{\partial y} + v\left[\frac{\partial^2 hv_m}{\partial y^2} + \frac{\partial^2 hv_m}{\partial y^2} - \frac{12v_m h}{h^2}\right] \quad (4)$$

$$\frac{\partial hu_m}{\partial x} + \frac{\partial hv_m}{\partial y} = 0 \quad (5)$$

where u_m and v_m indicate the average value on z axis of the velocity components, while for the pressure we can assume a constant trend in the direction z, i.e. $p(x, y, z) \simeq p(x, y)$. Since the computational domain is symmetrical, it must be studied half of the field of motion. The boundary conditions to be enforced are:

Hole F. The pressure at F point is known and can be derived from the pressure of the eye. The flow rate is also known (on the semicircle of the hole F), and it is possible to impose a radial velocity such as to ensure the removal of the aqueous humor.
It is yet to be understood if the flow is affected by the geometry of the backplate and its thickness or not.

Edge CD; $u = 0,\ v = 0\ e\ \frac{\partial p}{\partial y} = 0$

Edge CB; $u = 0,\ \frac{\partial v}{\partial x} = 0\ e\ \frac{\partial p}{\partial x} = 0$

For the scope of the simulation, the effect of the backplate has been rejected.

Edges AB e AD: since the contour is open it is possible to impose the CBC (clamped boundary condition) using the equation of radiant Sommerfield:

$$\frac{\partial \emptyset}{\partial t} + U_c \frac{\partial \emptyset}{\partial n} = 0 \tag{6}$$

U_c is the speed of wave propagation in CFD. U_c value is set equal to the modulus of the velocity, while n is the coordinate normal to the boundary and $\emptyset = [u, v, p]$.
Since the motion is carried out under conditions of steady flow, it follows that:

$$\frac{\partial \emptyset}{\partial t} = 0 \rightarrow \frac{\partial \emptyset}{\partial t} = 0 \tag{7}$$

Surgery stitches $q_x = 0, q_y = 0$
Differential equations 3,4,5 are solved by means of the difference finite method, resulting in a second-order accuracy in space.

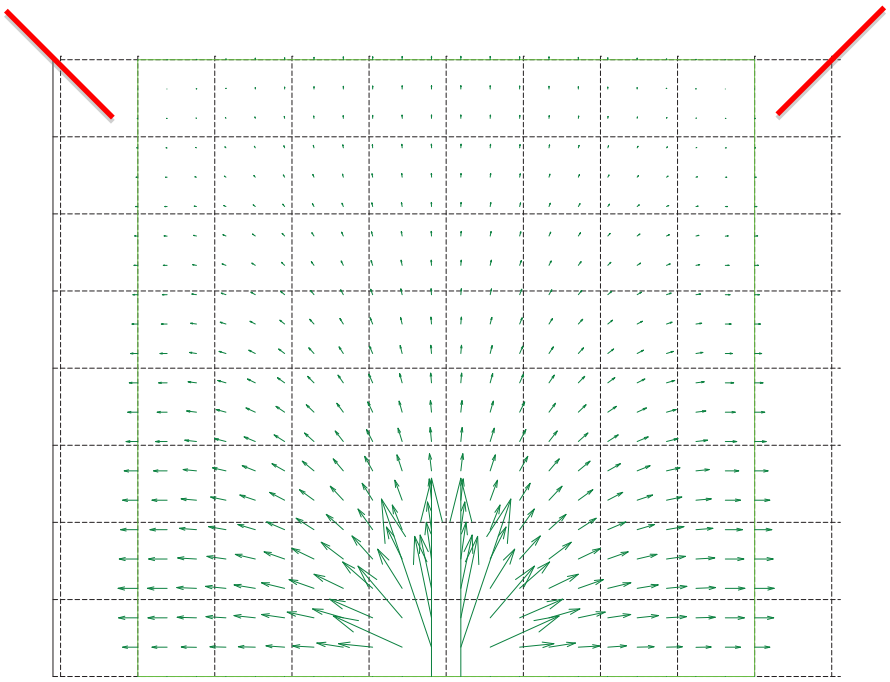

Figure 19. Motion field under the scleral flap in case of two stitches (red lines). Most of the flow takes place on the side edges

2D scleral flap deformation results

The 2D simulations have highlighted several important aspects:

- The flow is basically a creeping flow.
- The flow is mainly limited to the contours of BC and AD while the flow on the boundary AB is negligible (Figure 19).
- The lifting of the scleral flap presented maximum values around 50-70 microns which is roughly the height of the backplate of the device.
- The vertices of the scleral flap at the stitches positions A and B tend to lean against the wall underneath the flap and to compress it, reducing the capacity of flow from the edge AB (Figures 18 and 19).

Based on these results a 3D simulation model was created. The schematization was closer to the *in vivo* conditions. It was, in fact, possible to accurately study effect of the stitches positioning from a fluid dynamic point of view.

3D analysis of scleral flap deformation

The 3D model was performed by dividing the analysis into two stages:

- Study of the flow as a function of the stitches number
- Study of the flow as a function of the size of the gap between the flap and the scleral bed

Schematization of scleral flap

The scleral flap was modelled as shown in the Figure 20. The dimensions are shown in Table 1.

Schematization of device

Discretization of the device was obtained using tetrahedral finite elements[69]. The fin of the original device was not reproduced in the discretization, as it works as an anchoring element with no effect on the aqueous outflow (Figure 21).

Schematization of the stitches

The analysis was performed numerically by means of a finite element method[70] where

the space domain is discretized with tetrahedral elements (Figure 22).

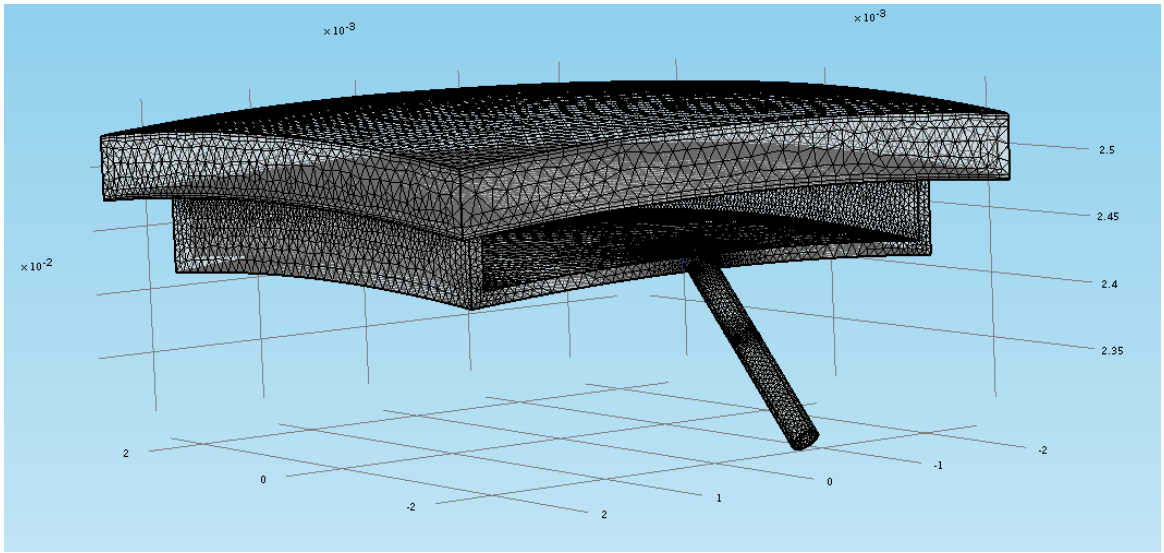

Figure 20. Discretization of the scleral flap using tetrahedral finite elements

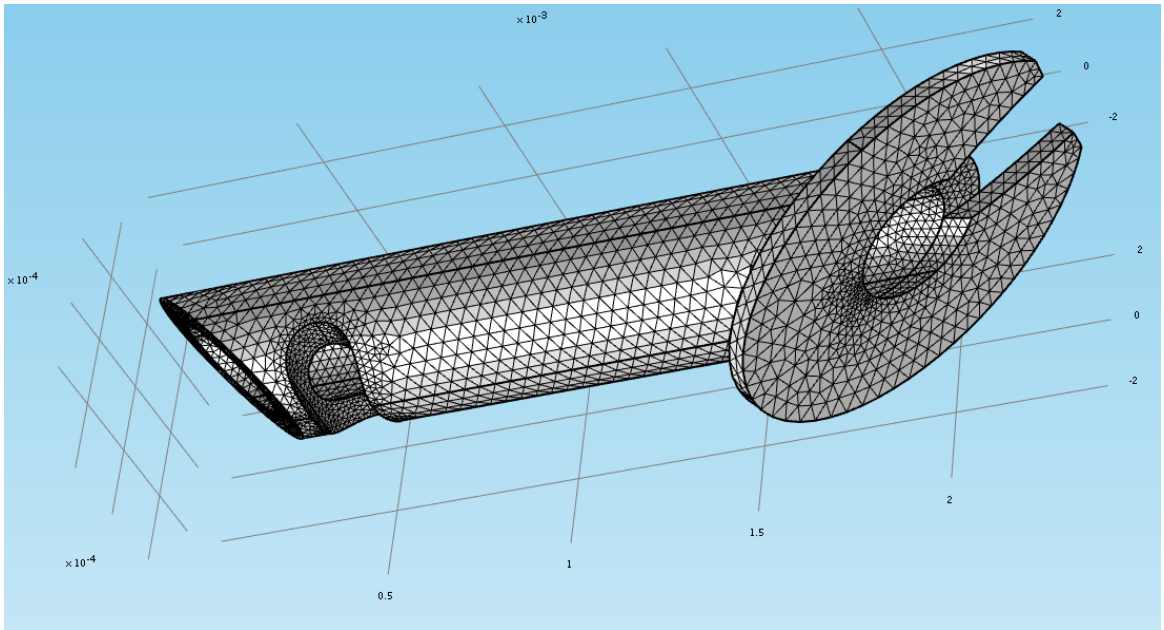

Figure 21. Discretization of the device. The anchoring fin, which appears in the original device, was not reproduced, as it has no effect on the fluid dynamics

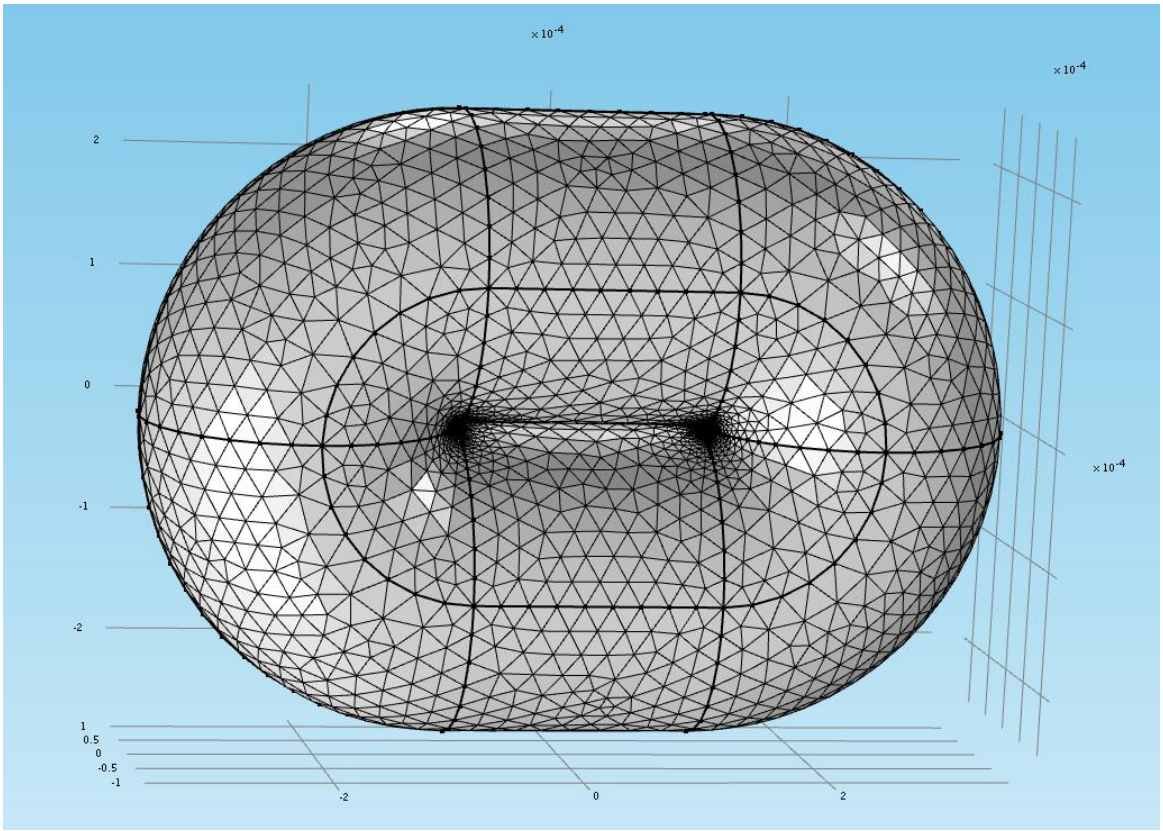

Figure 22. Discretization the surgical stitches

For maximum simplicity, the variables have been assumed to change linearly within every element. Momentum and mass balance equations were written in a dimensionless form:

$$\rho \frac{\partial \vec{u}}{\partial t} + \rho \vec{u} \cdot \nabla \vec{u} = -\nabla P + \vec{f} + \mu \Delta \vec{u} \quad (8)$$

$$\nabla \cdot \vec{u} = 0 \quad (9)$$

where $\vec{u}$ represents the velocity vector field, P the pressure field and μ the dynamic viscosity, ρ the density of fluid and $\vec{f}$ the gravitational force. Differential equations (8) and (9) were rewritten on the finite element mesh using a Galerkin residual procedure, resulting in a second-order accuracy in space.

Boundary conditions were given at the inlet by prescribing the discharge of aqueous, corresponding to Dirichlet integral conditions for all velocity components, and at the outlet of the device by imposing null total stress. No-slip condition was enforced on all

the rigid walls. Steady-state solution was achieved by time-marching the momentum equation with second-order fully implicit and variable time step. Every simulation was impulsively started from rest and marched until convergence. The steady regime was reached for each experiment, controlled by a numerical ”probe-point”. The number of elements used for the discretization was in the range of about 3×10^5 with a grid refinement near the outer walls. The typical size of the smaller elements was about 2.5 µm.

Validation test

First, an extensive grid refinement analysis was performed to verify the adequacy of the discrete representation of domain (Figure 23). The grid was refined by a cutback of two times the maximum and minimum size parameters of the mesh generator. This method allowed the number of tetrahedral elements to be approximately doubled. Figure 24 shows the variation of the streamlines for two cases ($3 \bullet 10^5$ and $6 \bullet 10^5$ elements). No significant physical difference can be detected.

The 2D simulations suggest that most f the aqueous flow occurs through the lateral sides of the sclera flap. In particular, the vast majority of drainage happens within 2 mm from the irido-corneal angle (Figure 19). According to this model, the position of the stitches is not relevant in terms of outflow position.

3D simulation results

The 3D analysis was conducted by splitting the scleral flap model from the device model, in order to avoid possible scale effects that may induce numerical problems and affect the finite elements model. The device model was simplified to a tube presenting an identical pipe in length and diameter.

Device flow analysis

Figure 25 describes the flow field of the device.

The flow rate and the pressure were imposed at the inlet and outlet openings respectively by introducing two ideal spheres. For graphic purposes only two couples of meridians have been represented in Figure 25. This strategy permits to avoid turbulences of flow close to the device.

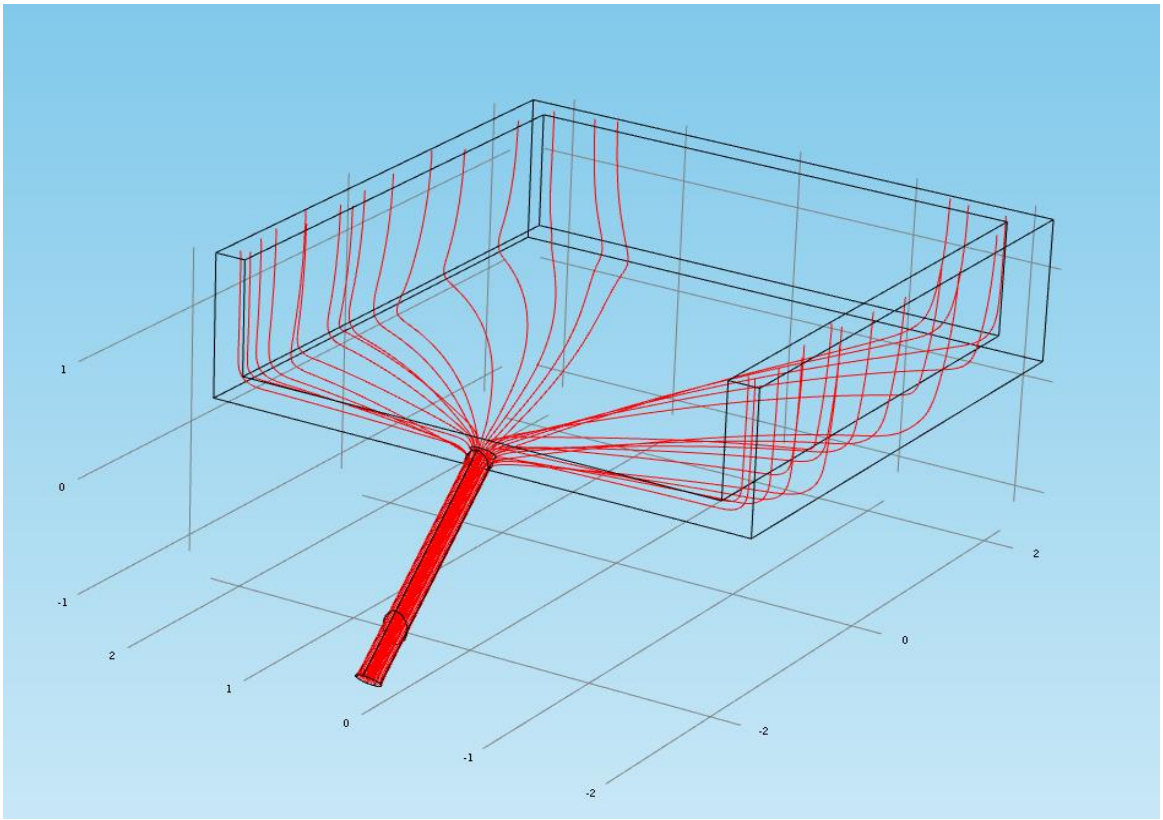

Figure 23. Domain of calculus with streamlines

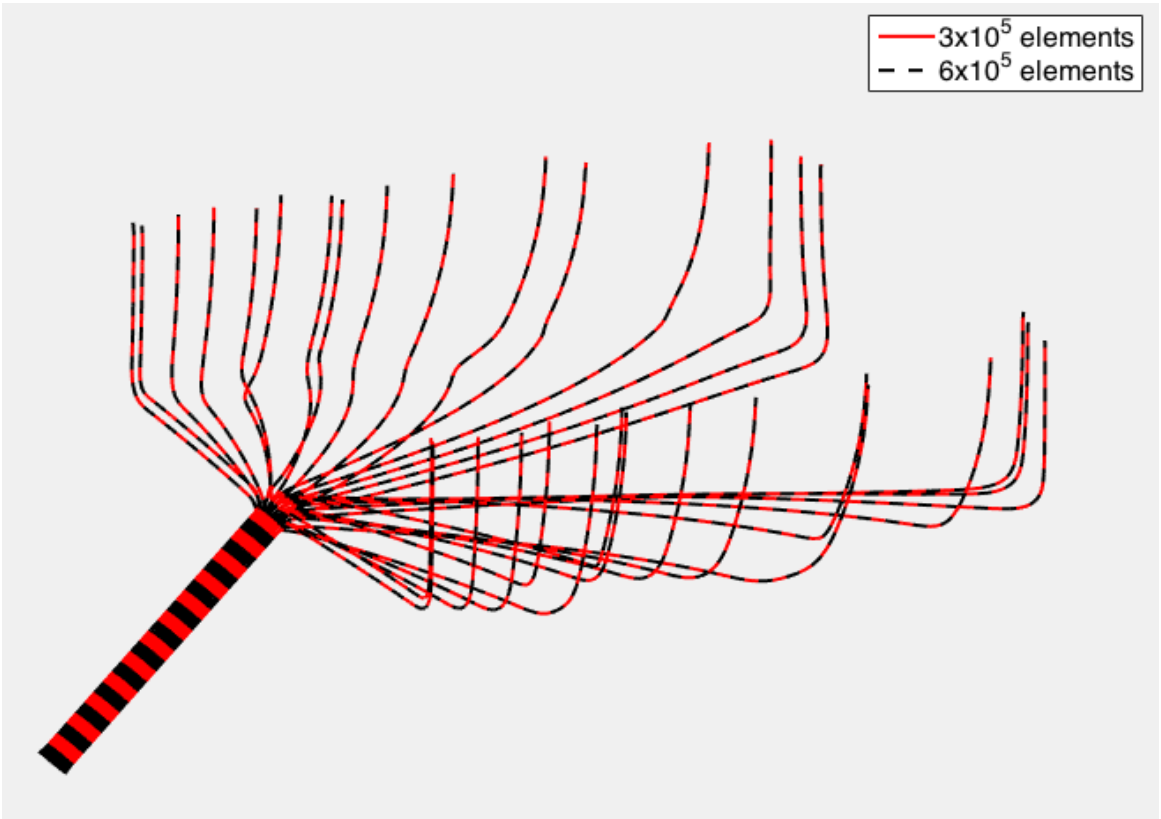

Figure 24. Streamlines with different discretizations. No significant physical difference can be detected

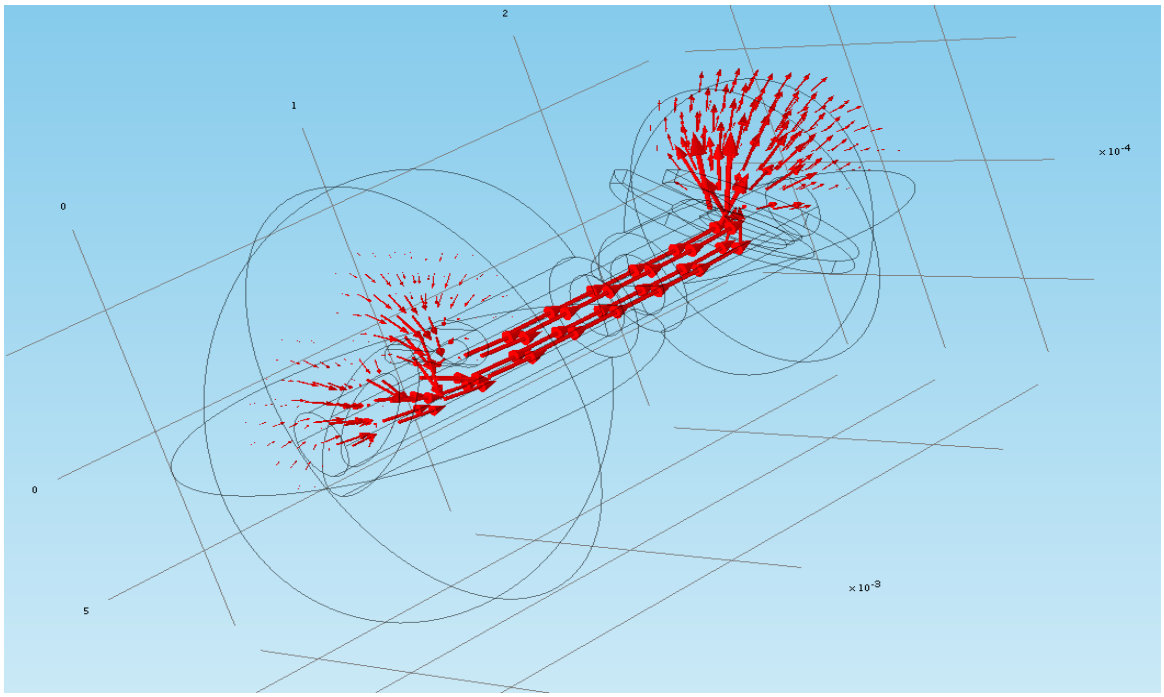

Figure 25. Flow field of the device

The flow data suggest that the aqueous flow rate through the two front openings in the device is almost identical. This is due to the reduction in the load loss at the inlets, which promotes the flow and creates a small and limited Venturi effect. The pressure loss between the inlet and outlet openings is in the range of 5 Pascal. Most of the loss occurs nearby the outlet opening and is related to the outlet loss. The presence of the backplate promotes this effect.

Analysis of the flow under the scleral flap and the conjunctiva

The 3D model confirms what was observed in the previous 2D model above described. Most of the flow is principally observed at the sides of the sclera flap. The flow rate in the superior part of the flap is very limited, in the range of 1% to 20-25% in case the patient rests in a supine position (Figure 26) and the interstitial space between the flap and the sclera bed is 10 microns (Figure 29). 80% of the outflow takes place within 2 mm from the scleral site, as shown in Figures 17 and 19, CB and AD sides. When a patient is standing, the 95-100% of the flow happens in that area, and no flow is expected from the upper side (AB).

The subconjunctival flow interferes with the flow originating from the scleral flap. The

flow is therefore compressed towards the base of the flap, thus limiting the lateral flow to a very small and restricted area. This is mostly evident when the patient is lying down on a side (Figure 27) and when is standing (Figure 28) with an interstitial space of 50 microns.

The simulation suggests that putting more stitches on the lateral sides of the sclera flap would be of limited influence on the outflow pattern, as this is conditioned by the interstitial thickness, which depends on the stiffness of the stitches. In other words, it depends on how tight the closure of the scleral flap is (Figure 27-31).

Figure 32 depicts a scenario in which the interstitial space under the sclera flap is 30 microns. In such a case, most of the pressure loss happens within the device and only minimally under the flap. The pressure loss range is between 5 and 12 Pascal. The simulations suggest that the backplate not only acts as an anchorage site, but also works as a spacer between the scleral bed and the scleral flap, reducing the risk of fibrosis and closure of the flap.

In conclusion, the 3D model suggests that the number of stitches is not relevant to affect the flow dynamics and that the flow is negligible at the superior edge of the flap (AB side in Figure 16).

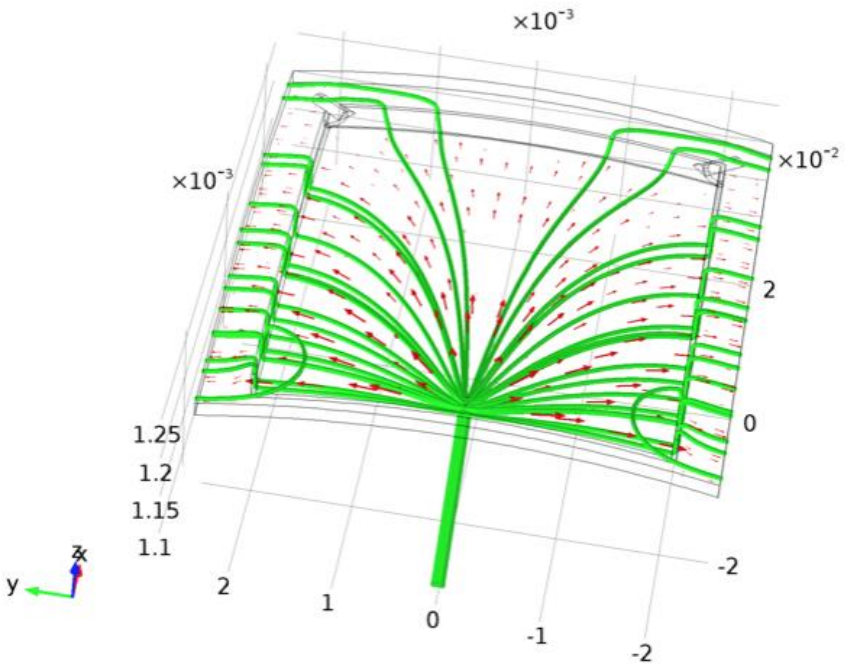

Figure 26. Flow field under the scleral flap, interstitial thickness 50 microns. The intraocular flows are affected by the spatial position of the eye and the action of the gravitational force. In this frame the patient is lying down

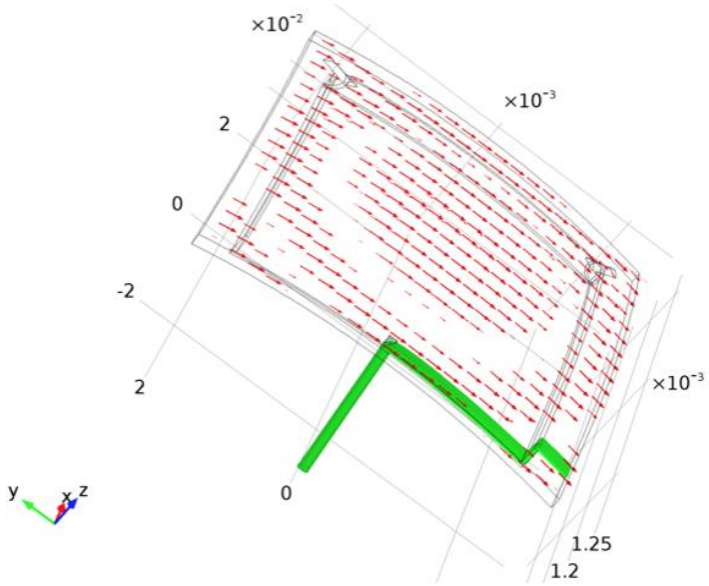

Figure 27. Flow field under the scleral flap, interstitial thickness 50 microns. The intraocular flows are affected by the spatial position of the eye and the action of the gravitational force. In this frame the patient is sleeping on left side. The flows under the sclera and under conjunctiva interact; the flow coming out of the scleral flap is concentrated near the base on left side

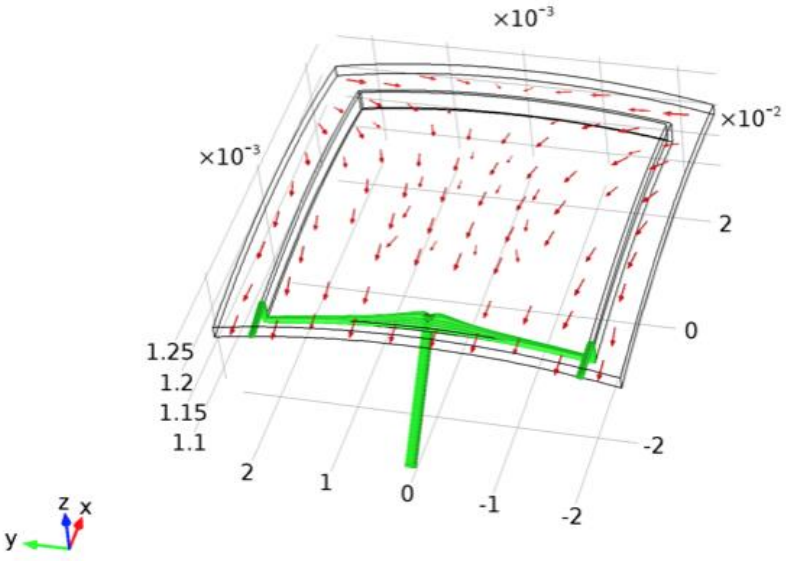

Figure 28. Flow field under the scleral flap. The intraocular flows are affected by the spatial position of the eye and the action of the gravitational force. In this frame the patient is standing. The flows under the sclera and under conjunctiva interact; the flow coming out of the scleral flap is symmetrically concentrated near the base

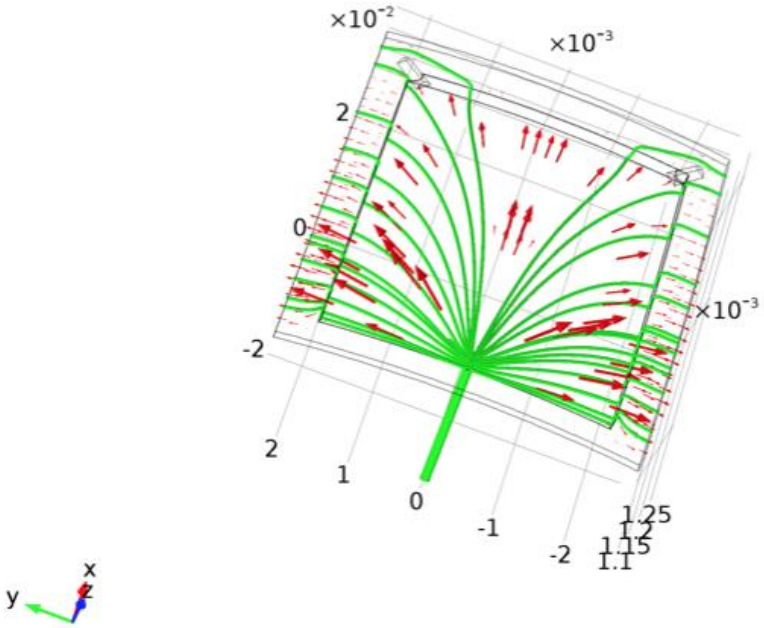

Figure 29. Flow field under the scleral flap, interstitial thickness of 10 μm. The flows are affected by the spatial position of the eye and the action of the gravitational force. In this frame the patient is lying down

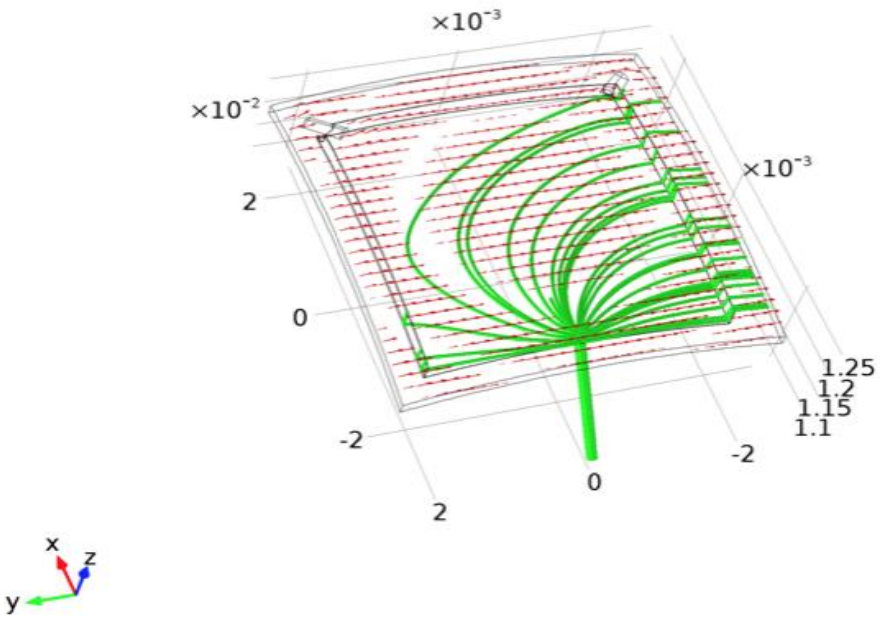

Figure 30. Flow field under the scleral flap, interstitial thickness of 10 μm. The intraocular flows are affected by the spatial position of the eye and by the action of the gravitational force. In this frame the patient is sleeping on left side. The flows under the sclera and under conjunctiva interact; the flow coming out of the scleral flap is concentrated around the base on left side

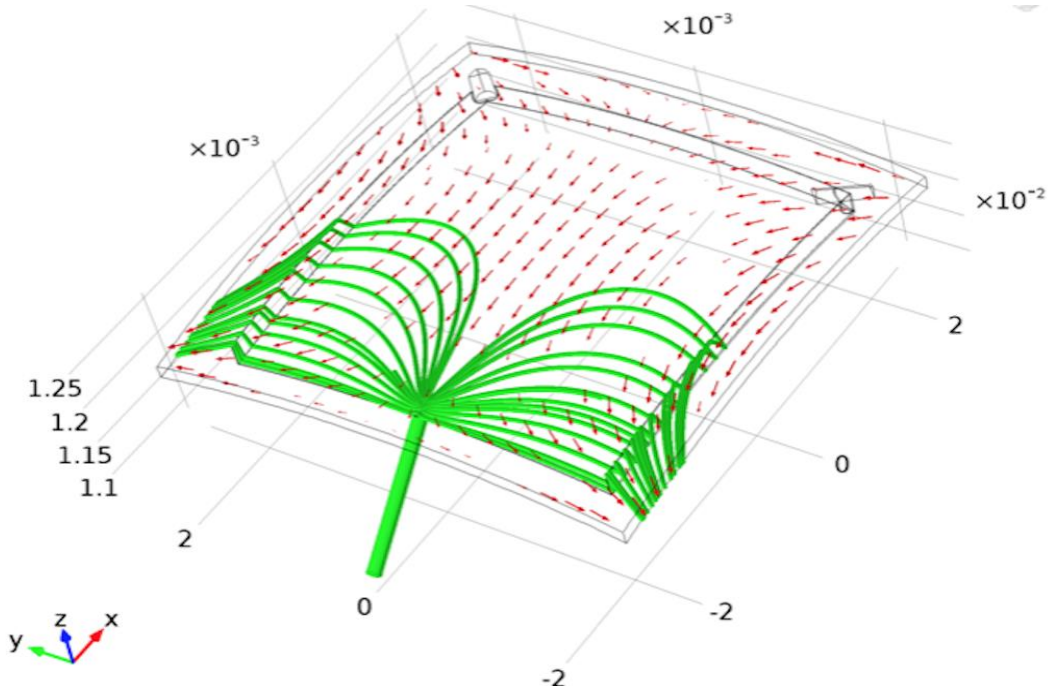

Figure 31. Flow field under the scleral flap, interstitial thickness of 10 μm. The intraocular flows are affected by the spatial position of the eye and by the action of the gravitational force. In this frame the patient is standing. The flows under the sclera and under conjunctiva interact but to a lesser extent than supine lying down (Figure 29). The flow coming out of the scleral flap is concentrated near the base

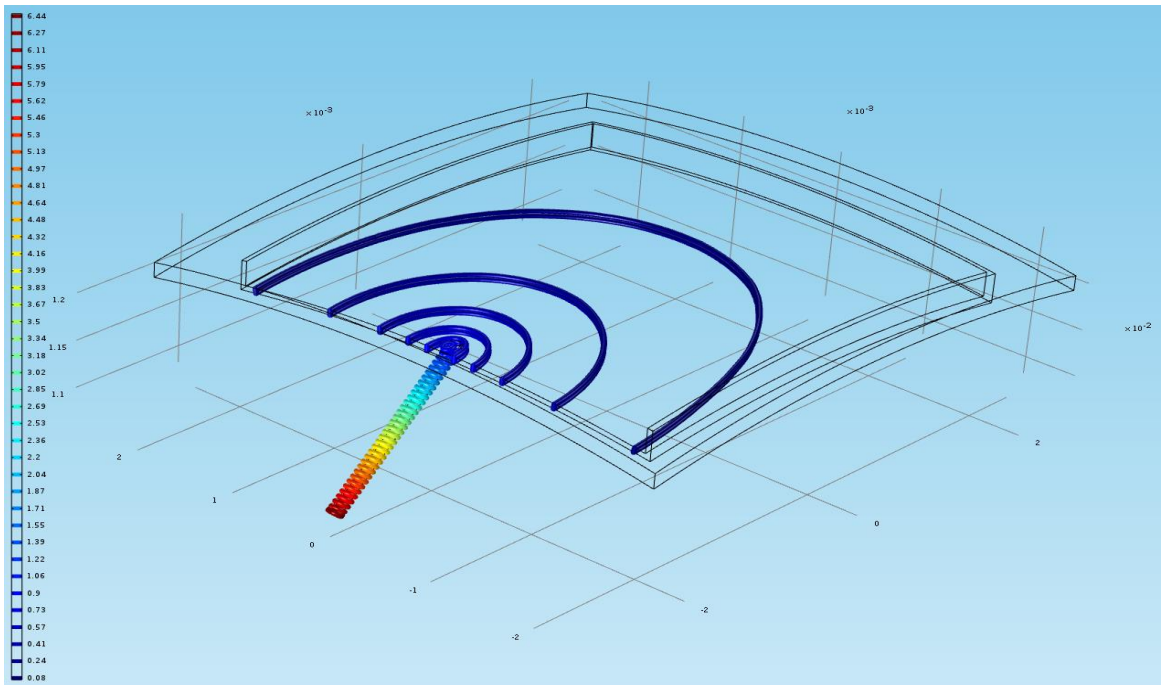

Figure 32. Pressure field under the scleral flap, interstitial thickness of 30 μm. The intraocular flows are affected by the spatial position of the eye and then the action of the gravitational force. In this frame the patient is lying down

Analysis of static deformation of the scleral flap

As already mentioned, the pressure loss associated with the flow underneath the sclera flap is negligible. Therefore, it is reasonable to investigate the deformation of the scleral flap, caused by a uniform pressure applied form below. The intra-ocular pressure, for the following experiment, is assumed to be 20 kPa. The scleral flap is modelled as a three-dimensional, linear elastic solid with the geometrical and physical characteristics reported in Table 2.

Property	**Value**
Curvature (eye's radius)	12.5 mm
Thickness	0.5 mm
Poisson's modulus	0.46 – 0.49
Elasticity modulus	$23 \cdot 10^6$ - $36 \cdot 10^6$ Pa

Table 2. Geometrical and physical properties of the sclera

Different arrangements of the stitches are considered, as shown in Figure 33. A stitch is modelled as a cylinder of diameter 1.5 mm intersecting the sclera flap and locking the intersection surface. U4P3 elements are used (mixed formulation for nearly-incompressible materials).

A set of simulations is carried out on a planar geometry, i.e., the curvature of the sclera flap is neglected. The vertical displacement obtained in the three cases is shown in Figure 34, for v=0.49 and E=36e6 Pa, Figure 35 for v =0.46 and E=36e6 Pa, in Figure 36 for v =0.49 and E=23e6 Pa, in Figure 37 for v =0.46 and E=23e6 Pa.

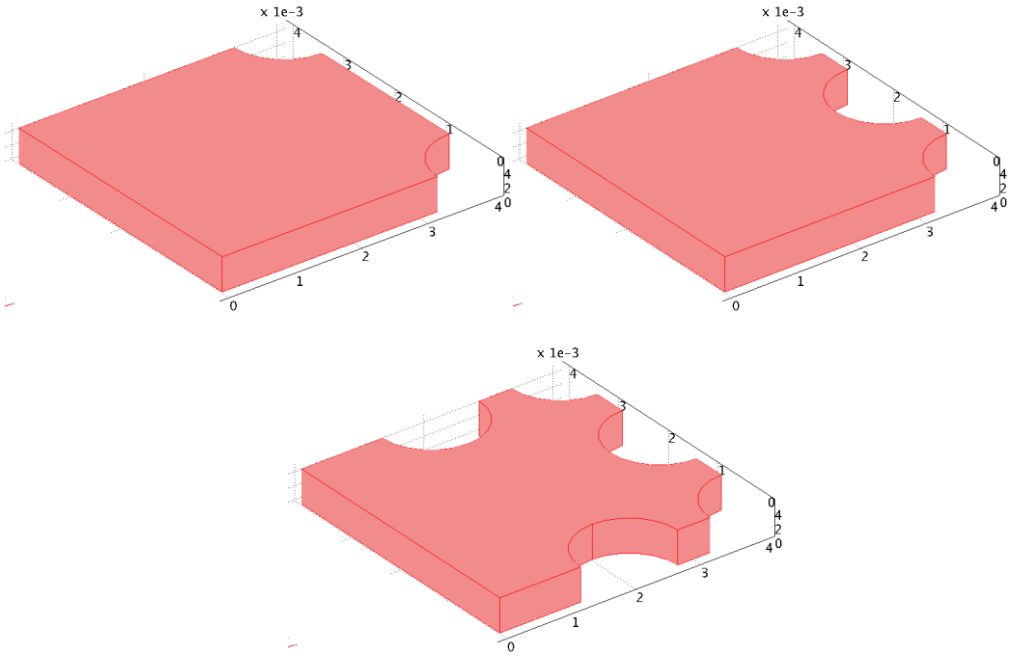

Figure 33. Arrangement of 2, 3 and 5 stitches

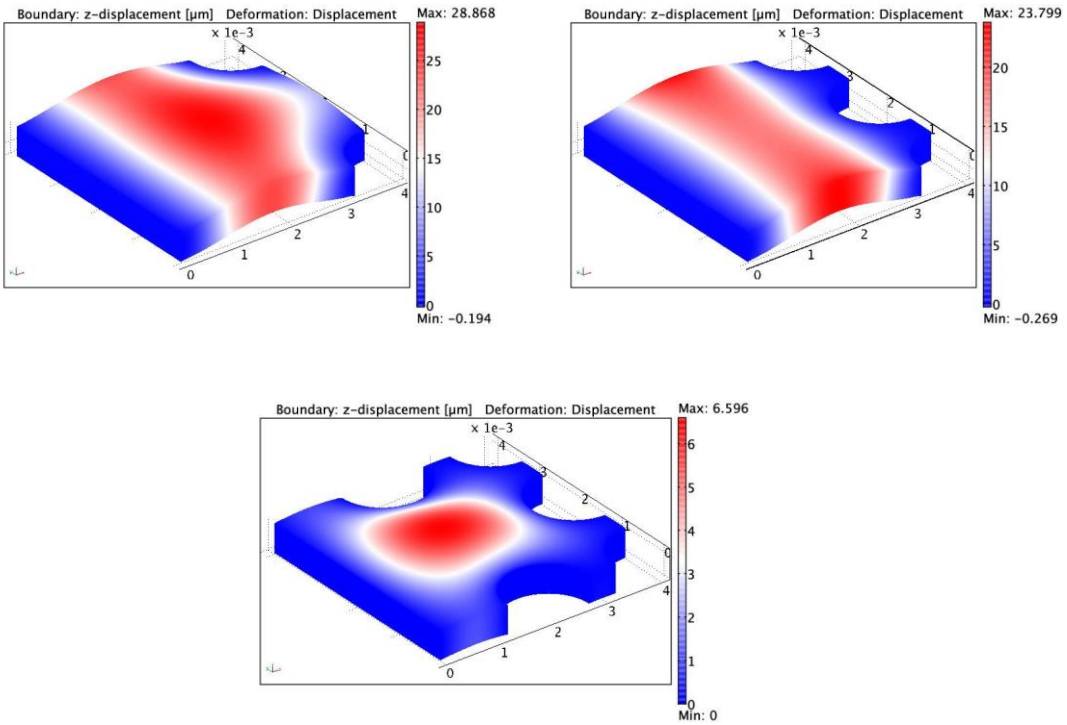

Figure 34. Vertical displacement (in microns) of the scleral flap v =0.49, E=36e6 Pa

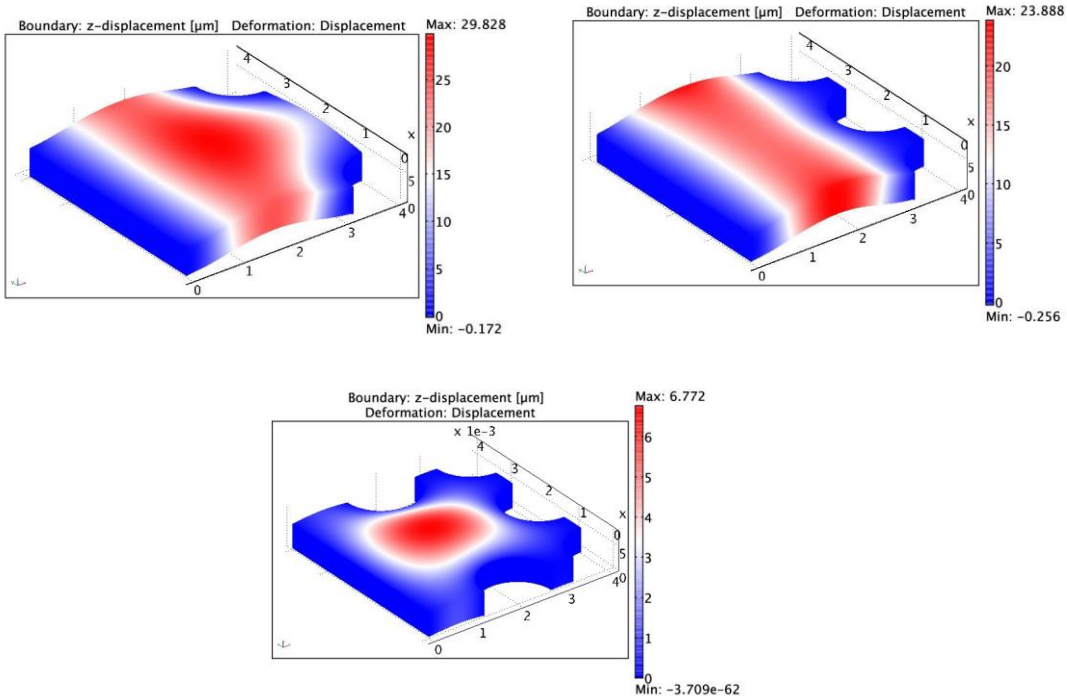

Figure 35. Vertical displacement (in microns) of the scleral flap v=0.46, E=36e6 Pa

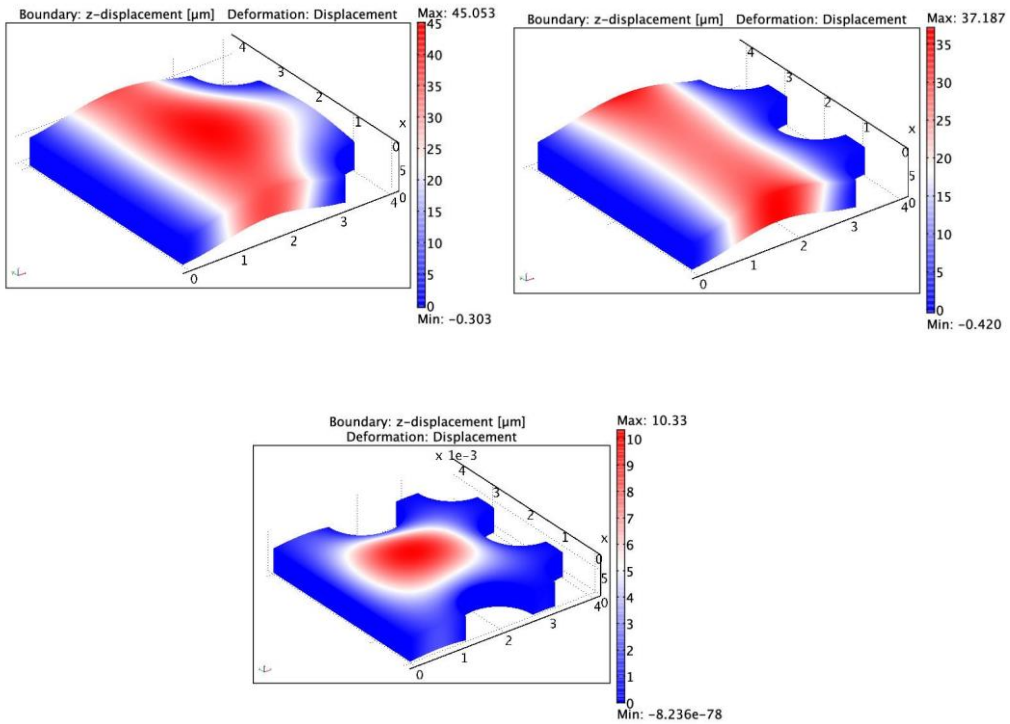

Figure 36. Vertical displacement (in microns) of the scleral flap v=0.49, E=23e6 Pa

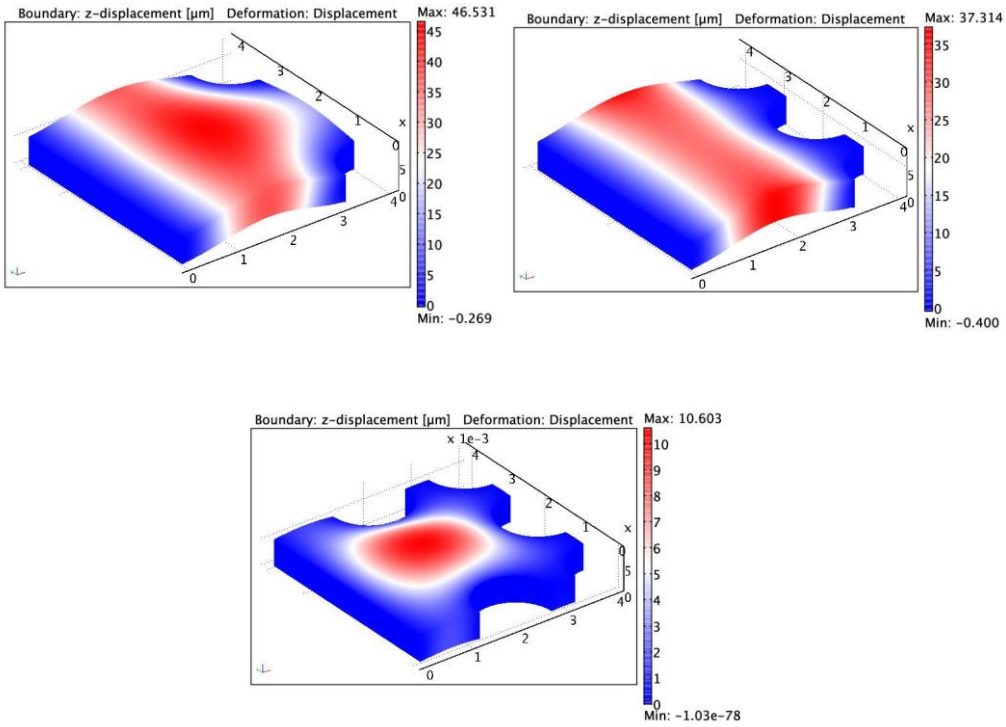

Figure 37. Vertical displacement (in microns) of the scleral flap ν=0.46, E=23e6 Pa

Table 3 yields a synthetic view of the deformation pattern of the scleral flap, under different conditions. In the following, Δw denotes max(w)-min(w), while w_c denotes mean (Δw).

Nr. Stitches	Constrained	$\frac{\partial w}{\partial q}\frac{\bar{q}}{\bar{w}}$	w_c (mm)
2	ν=0.46	-0.993	38.3995
2	ν=0.49	-0.994	37.209
2	E=23e6 Pa	-0.496	**46.0775**
2	E=36e6 Pa	-0.322	29.531
3	ν=0.46	-0.996	30.929
3	ν=0.49	-0.996	30.8375
3	E=23e6 Pa	-0.0450	37.6605
3	E=36e6 Pa	-0.0320	24.106
5	ν=0.46	-1.001	8.6875
5	ν=0.49	-1.001	8.463
5	E=23e6 Pa	-0.413	10.4665
5	E=36e6 Pa	-0.266	**6.684**

Table 3. Deformation pattern of the scleral flap

Von Mises stress

The same trend could be observed for all combinations of mechanical properties: maximum von Mises stress is near the stitches. Five stitches induce less than half Von Mises stress compared with two stitches.

$$\sigma_v^2 = \frac{1}{2}[(\sigma_{11} - \sigma_{22})^2 + (\sigma_{22} - \sigma_{33})^2 + (\sigma_{11} - \sigma_{33})^2 + 6(\sigma_{23}^2 + \sigma_{31}^2 + \sigma_{12}^2)\,]$$

Nr. stitches	ν	E (MPa)	σ von Mises (min/max, MPa)
2	0.46	36	0.00073/1.41
3	0.46	36	0.0010/1.12
5	0.46	36	0.00073/0.56
2	0.46	23	0.00029/1.46
3	0.46	23	0.00084/1.18
5	0.46	23	0.00073/0.57
2	0.49	36	0.00013/1.45
3	0.49	36	0.00045/1.19
5	0.49	36	0.00071/0.58

Table 4. Von Mises stress according to the number of stitches

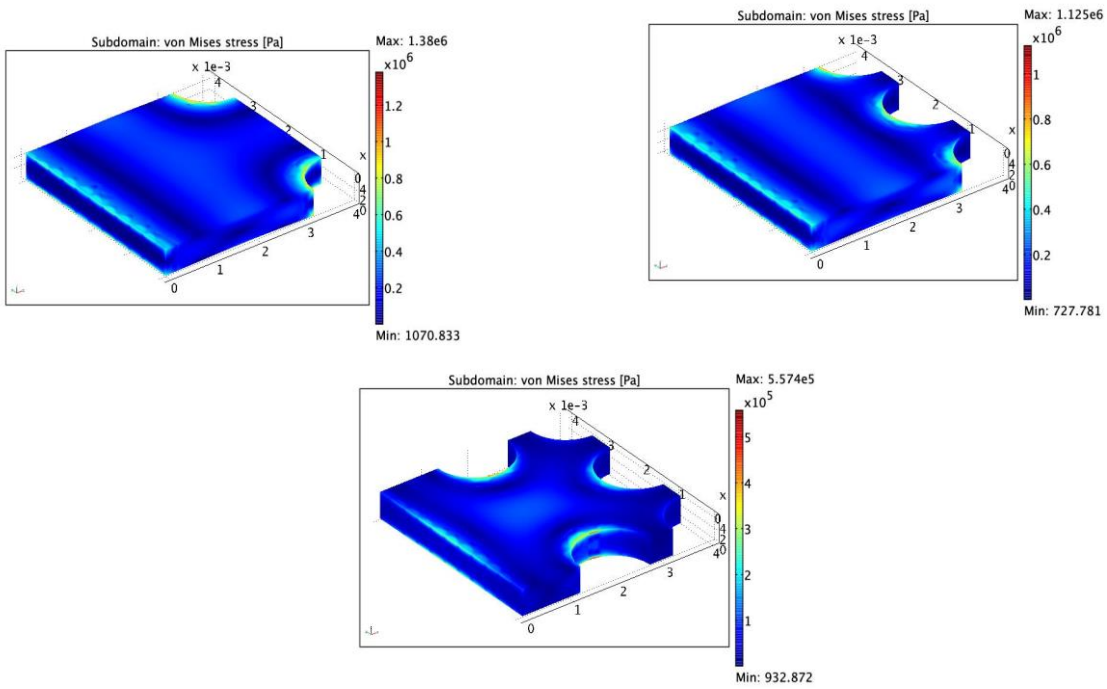

Figure 38. Von Mises stress v=0.46, E=36e6 Pa

Curvature effects

The scleral flap with 5 sutures, v=0.49 and E=36e6 is now modelled, taking into account its curvature (1.25 cm external radius). Results are reported below (Figure 39). Maximum vertical displacement is 6.355 microns, to be compared with 6.596 microns for the corresponding planar geometry (-3.8% difference, compatible with numerical error). Maximum von Mises stress is 5.91 Pa, to be compared with 5.825e5 Pa for the corresponding planar geometry (+1.4% difference, compatible with numerical error).

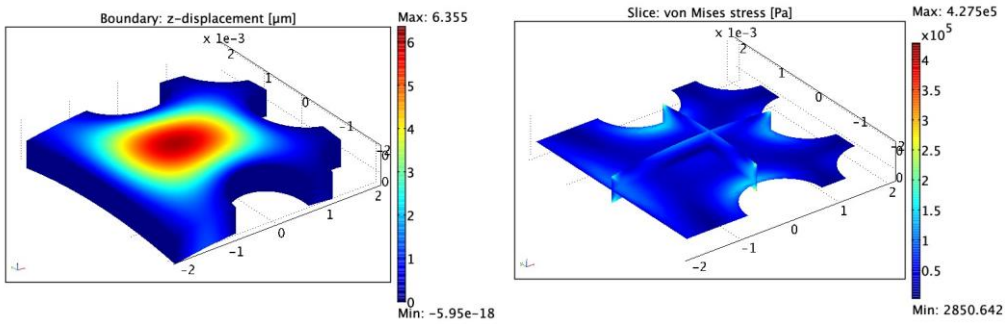

Figure 39. Vertical displacement (in microns) and Von Mises stress of the scleral flap. ν=0.46, E=23e6 Pa. Five stitches simulation

Shrinkage of the removed portion of scleral flap due to relaxation of initial stress state

Shrinkage of the surgical cut is a well-known phenomenon. Thus, the scleral flap is expected to undergo a small shrinkage after being sculpted. It is reasonable to admit that a small gap between its lateral boundary and the scleral bed is created. In order to reproduce the aforementioned shrinkage phenomenon, the scleral flap is depicted with an applied initial stress. Figure 40 shows the final configuration of the scleral flap after the release from the initial stress, without the application of stitches and without the effect of the intra-ocular pressure acting from below. The initial stress is set to a rather unrealistically large value of 10 bar ($\sigma_{xx} = \sigma_{yy} = 10^6 Pa$, while the other stresses are zero).

An alternative model for stitches positioning

In this section, E=36e6 Pa and v=0.49 for the scleral flap are considered.

1.5mm long, 1.5 caliber (=0.15 mm diameter) stitches are modeled by constraining portions of the upper surface of the scleral flap ("fixed" boundary condition).

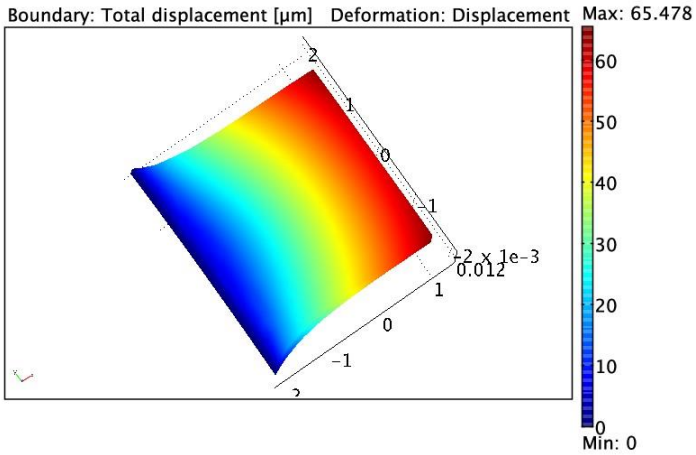

Figure 40. Total displacement of the scleral flap, expressed in microns

The resulting vertical displacement and von Mises stress are shown in Figure 41.

The initial stress, previously defined, is set to $\sigma_{xx} = \sigma_{yy} = 10^5 Pa$. The minimum and maximum vertical displacements are -5.432 and +38.58 microns respectively.

The distribution of the vertical displacement is qualitatively similar to that obtained using the rough representation of the stitches, used in the former calculations, but the min and max vertical displacements were, in that case, -0.269 and +23.80 microns. Thus, the scleral flap was significantly more stiffly constrained with the rough model.

The min and max values of the von Mises stress are 4187.79 Pa and 2.78e6 Pa.

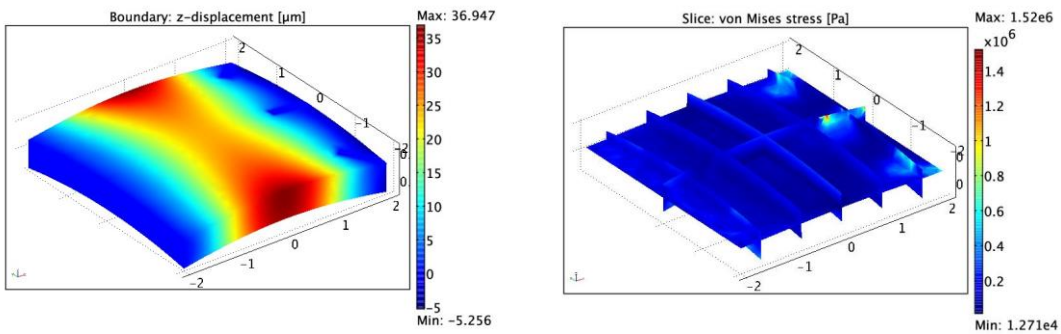

Figure 41. Vertical displacement and Von Mises stress (see text)

7. Nanocoating

One of the most dangerous and sight threatening post surgical complication is the infection of the conjunctival bleb and eventually the infection of the eye, which is called endophthalmitis. Endophthalmitis requires prompt surgical and systemic antibiotic treatment. Even if correctly treated, visual function may be seriously impaired, without recovery.

The evidence of cell adhesion and massive bacteria proliferation on the surface strongly suggested a surface functionalization in order to reduce those events.

Biofilm formation and biocorrosion are critical problems to face in many fields such as food industry, infrastructures and especially in medicine, where a sterile environment is essential. Biofilms[70] are composed of microorganisms, which tend to stick to each other embedded in an extracellular matrix, with a strong tendency to adhere to and populate surfaces. Surface deterioration was defined as microbiologically influenced corrosion.[71] In particular, body fluid and physiological solutions are considered to be extremely corrosive to metals due to high salt concentration and protein adhesion. These processes may lead to metal deterioration and consequent release of potentially dangerous substances in the organism. For instance, stainless steel corrosion releases iron, chromium and nickel ions, which are definitely non-biocompatible. Nickel, indeed, is widely known as a strong allergenic. The high concentration of chloride anions (Cl-) in body fluid is thought to increase the corrosion rate on metal implants.[72]

Long-term implants require a high standard of biocompatibility, in order to guarantee the success of the surgery. Biocompatibility also depends on the environmental conditions. The same material may present different level of biocompatibility according to the site of implantation in the human body.

The Ex-Press glaucoma shunt is built in stainless steel (SS) 316LVM, an alloy widely used in surgical implants. The use of SS in surgical applications began in 1926, mainly in orthopedic surgery where it was used for implant fixations, due to its corrosion resistance and mechanical strength.[73]

Pioneering SS contained ~18 wt% Cr and ~8 wt% Ni with Iron as major component. However Ni was found to be one of the principal causes of allergy. Later on it was found

that SS properties could be tuned by the addition of other components such as Molybdenum. 316 SS containing a small quantity of Molybdenum was found to have more corrosion resistance, which is further improved in the 316L SS alloy by reducing the quantity of Carbon from 0,08% to 0,03%. More details about 316L SS are reported in Table 5.

In this alloy a passivation film composed by Chromium, Molybdenum and Iron oxides provides corrosion resistance.[74]

The Ex-Press glaucoma shunt is claimed to be manufactured in an almost identical alloy, called SS316LVM (low carbon vacuum melt). The low carbon vacuum melt technology permits to achieve high levels of purity and cleanliness. It has excellent resistance to both general and intergranular corrosion, and pitting and crevice corrosion. Breaking down the name, this is a low-carbon version of 316 that has been vacuum arc remelted to reduce impurities. Beyond removing impurities, this process, in combination with the unique nickel and chromium content of 316, tends to facilitate the formation of the surface chromium oxide layer that makes stainless steel corrosion resistant.

There is some belief that 316 LVM forms a more substantial surface layer, and that this plays a strong role in protecting the host body from reactions to the nickel content of the material. Nonetheless, in the explanted Ex-Press shunt some superficial corrosion pits were observed, suggesting that this allow may not be immune to corrosion by biological fluids.

Component	%	Component	%
Cr	16-18	P	0.045
Ni	10-14	S	0.03
C	0.03	N	0.1
Mn	2	Mo	2-3
Si	0.75		

Table 5. 316L SS composition

Polymers

Biocompatible polymers are extensively used in medicine. Polymer properties depends on the functional groups, chain length, flexibility, chemical and physical properties.[75-77] The potential use of those molecules is extremely wide, ranging from tissue reparation to drug

delivery systems and biodegradable implants.[75] Poly-lactic, poly-glycolic and polylactic-co-glycolic acid are biodegradable polymers widely studied and used in drug delivery systems.[77] A hydrolytic process fragments the polymeric matrix, and the drug is progressively released.

Grafting polymers on metals

Many industrial and medical applications would take advantage of combining the chemical and physical properties of metallic alloys to the biological activity of polymers. Composite/hybrid materials could guarantee the resistance and mechanical strength of metals and the functionality and versatility of polymers. SS surface modification has been widely studied.[71,72] Joining polymers to metal can be achieved either through adsorption or covalent bonding. In the first case interaction such as Van der Waals forces are present. When polymers are jointed to a surface they can adopt many conformations and architectures depending on factors such as chain length, flexibility, steric hindrance and graft density. The last property is defined as the number of chains attached per unit area. It has to be noted that polymers are attached to the surface by one chain end and conformations are completely different from those adopted by a free polymer in solution. One of the possible behaviors is the *brush regime* where the polymer chains are protruded. The brush regime is favored by high graft density because of steric repulsions between neighboring grafting points. Otherwise, when the graft density is lower, polymer chains are most likely to fold assuming the so-called *mushroom regime*. Chains conformation is fundamental in determining which regime is favored. Chain length and stiffness are the most influencing factors for conformational mobility and dynamic volume of the brush. This volume is a cone where the chain is free to move thanks to thermal motions. Long and flexible chains will have a bigger dynamic volume than short and stiff chains. Graft density is strictly related to these aspects. There must be a compromise between the steric repulsion and the graft density.

Figure 42 presents an illustration of the steric hindrance and the relation between graft density and molecular weight of the polymer brush.

Two main strategies can be employed in order to graft polymers to surfaces: the *grafting to* and the *grafting from* approaches (Figure 43). The first consists in the anchoring of pre-synthesized polymers via either physisorption or covalent bond formation.

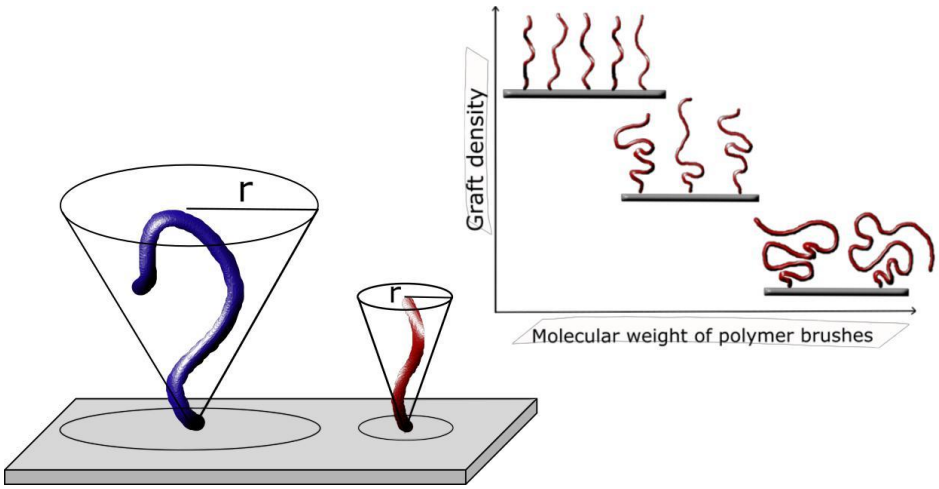

Figure 42**.** Effects of chain length and stiffness on steric hindrance (left) and his consequence on graft density (right).

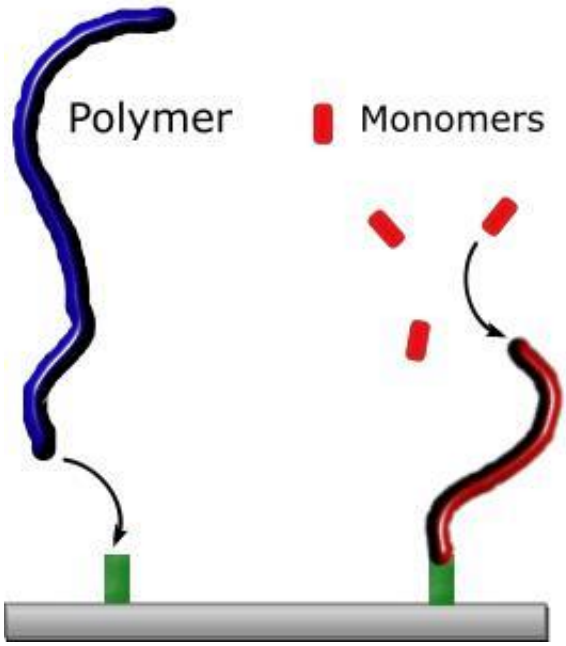

Figure 43. *Grafting to* (left) and *grafting from* (right) methods.

The second involves the polymerization directly initiated from the surface, previously functionalized with the proper initiator agent. The *grafting to* strategy suffers from several limitations, which prevent the formation of thick and dense polymer brushes. As the

molecular weight of the polymers increases, the reaction between the end-group of the chain and the complementary group on the surface becomes more and more difficult due to steric repulsion.

On the contrary the *grafting from* approach is more versatile and able to get a higher graft density, but shorter chains.

Controlled/"living" polymerization techniques allow accurate control over brush thickness, composition and morphology. Anionic and cationic polymerization, ring-opening polymerization and free-radical polymerization are some of the most diffused. Among the different controlled/"living" polymerizations, radical based strategies are the most widely used, due to their advantages in terms of compatibility with organic and aqueous media as well as for a large number of functional groups.

Among the polymer grafting techniques, the reversible addition-fragmentation chain transfer (RAFT)[78-80] was applied for the purposes of the present study.

Grafting procedure

For the present study, 316L SS 1x1cm plates were used. *Grafting from* technique is based on the growth of polymers directly from the surface, previously functionalized with proper species. In this case the species was a RAFT agent. Monomers employed were styrene, methylmethacrylate and N,N-dimethylacrylamide. This technique proved to be more efficient and easier with respect to the *grafting to* approach, which requires more synthetic steps.

Samples were polished with silicon carbide abrasive papers 800, 1000, 1200 grit respectively and with aluminum oxide abrasive spray with 3μm and 1μm particles. Mirror surfaces were obtained at this point.

Samples were then cleaned with de-ionized (DI) water, ethanol, acetone and DI water with sonication for 10 minutes. After this procedure piranha solution was employed to remove all the organic traces still present on the surface. Piranha solution is a mixture 3:1 vol. of sulfuric acid (H_2SO_4, 98%) and hydrogen peroxide (H_2O_2). The strongly oxidizing solution obtained has to be handled carefully and the volume percentage of hydrogen peroxide should never be higher than 30%, otherwise explosions may occur. Piranha solution is able either to remove all the organic traces and to provide a hydroxyl enriched surface (Figure 44). Samples were immersed for 30 min in the mixture. An ice bath was

employed to prevent an excessive increase of temperature due to the highly exothermic process. The active hydroxyl groups are fundamental for the next functionalization steps.

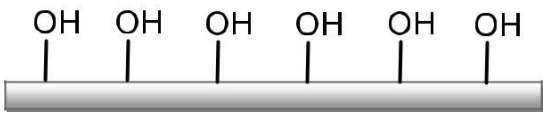

Figure 44. Hydroxyl enriched surface.

Subsequently, a coupling agent is needed to act as an intermediary for further functionalization. This first coating can have different functions such as protecting from corrosion or providing the proper functional groups to promote the attachment of further molecules in case they are not capable to directly bound to the surface. Generally silanes are versatile compounds widely used to form layers of different types (Figure 45). They are known as silanes coupling agents (SCA). The reaction is a condensation.

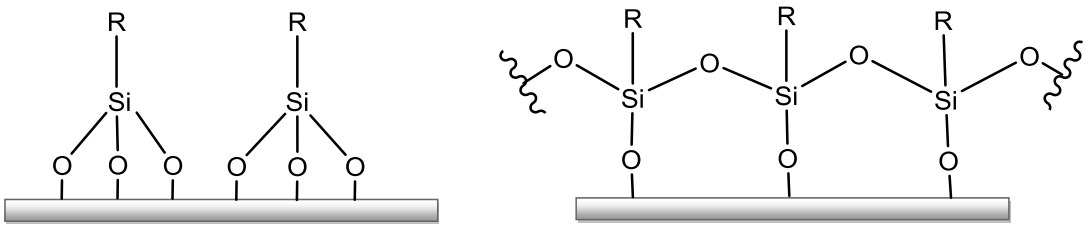

Figure 45. Silane adhesion on the SS surface

RAFT agent S-benzyl-S'-(trimethoxysylil) propyl trithiocarbonate (BTMePT) was anchored to the surface through a condensation (Figure 46).

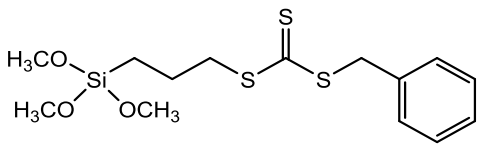

Figure 46. S-benzyl-S'-(trimethoxysylil) trithiocarbonate (BTMePT).

The reaction was conducted in toluene at 60°C for 24h. Samples were than cleaned in different solvents with sonication (Figure 47).

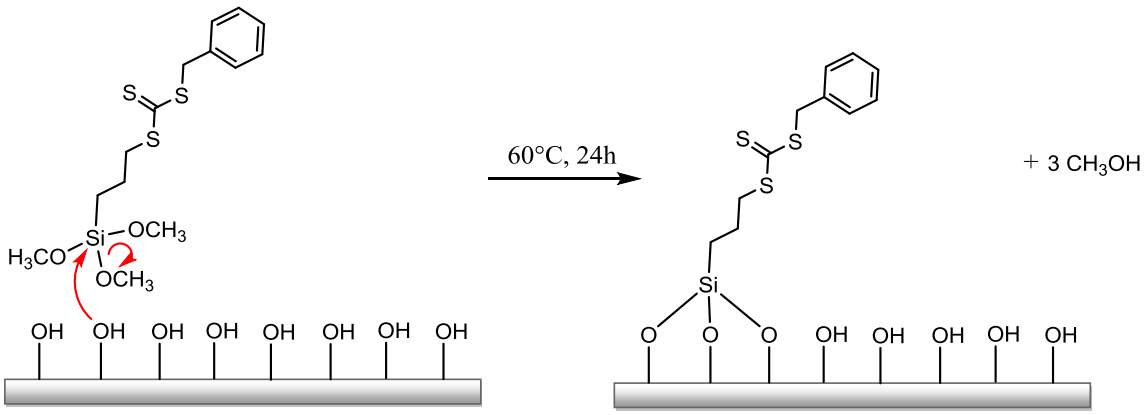

Figure 47. Silanization process

Polymerization was initiated from the surface. SS plates were immersed in an anhydrous N,N-dimethylformamide (DMF) solution containing monomer and initiator. The reaction proceeded for three days at 70°C under stirring. Samples were than cleaned in different solvents with sonication to remove absorbed polymer.

Figure 48 describes, as an example, the polystyrene growth.

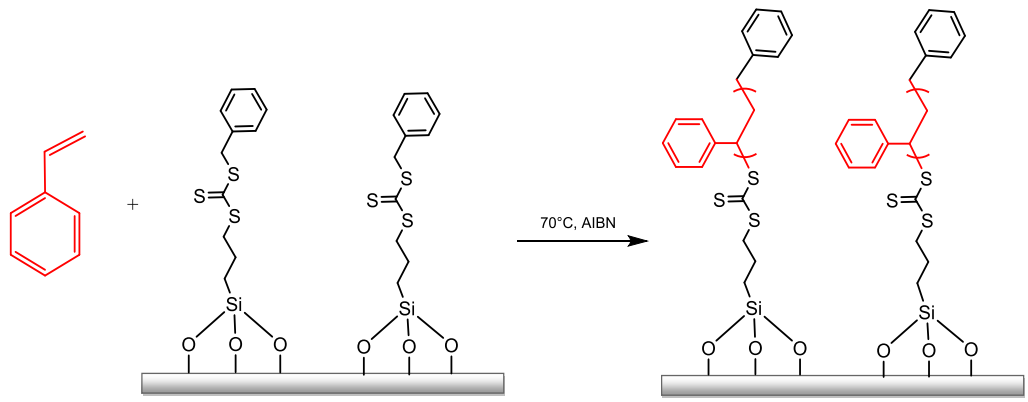

Figure 48. Polystyrene growth on the silane functionalized SS plates

Figure 49 shows the plates functionalized with Polystyrene (PS), Polymethilmetacrylate (PMMA), and PolyN,N-dimethylacrylamide (PDMA) respectively.

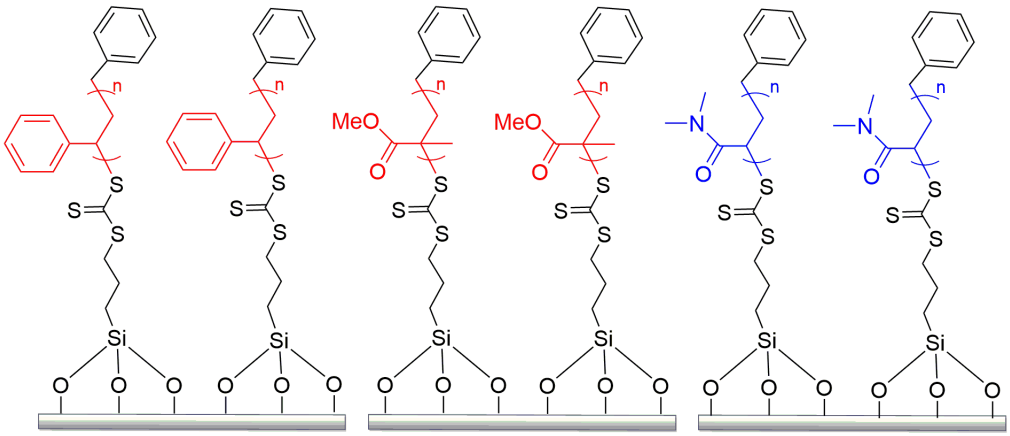

Figure 49. SS samples functionalized with PS, PMMA and PDMA.

Surface characterizations

Contact angle

Contact angle is a thermodynamic measurement that can be used to study the wettability of a surface, and permitting to distinguish between hydrophilic and hydrophobic materials. Usually surfaces with contact angles higher than 90° are said to be hydrophobic, those with contact angles higher than 140° are known as super hydrophobic and those with contact angle smaller than 90° are considered hydrophilic (Figure 50).

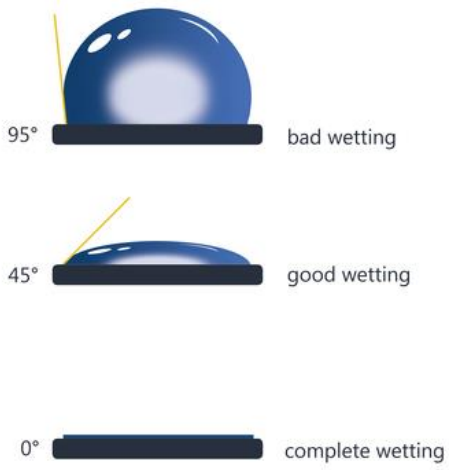

Figure 50. Contact angle

Pristine surfaces

Surfaces polished and cleaned with piranha solution are the element of comparison for the next functionalization steps. Interestingly it was found that the contact angle was different

if the measurement was made immediately after piranha treatment or more than one day after. Specifically, the contact angle was really low (highly hydrophilic surface) if measurements were taken few hours after the procedure. Conversely, days after, the contact angle was higher. This may be due to dehydration of the hydroxyl groups on the surface to give an oxide layer. Therefore any functionalization with silanes has to be made immediately after piranha treatment to guarantee the largest number of active hydroxyls on the surface. Similar results were found in literature[72] where contact angle is different before and after piranha solution treatment. Typically the contact angle values immediately after the piranha solution is in the range of 20-25° while a few days after is in the range of 58-64°.

Functionalization with S-benzyl-S'-(trimethoxysilyl) propyl trithiocarbonate (BTMePT)

This silane is specifically projected for *grafting from* techniques. Indeed it is a chain transfer agent (CTA), with a trithiocarbonyl group. Thiocarbonyl group remains anchored to the surface during the polymerization.

The contact angle after functionalization was in the range of 80-94°. As expected, surfaces become more hydrophobic thanks to the benzyl group of the silane (Figure 51).

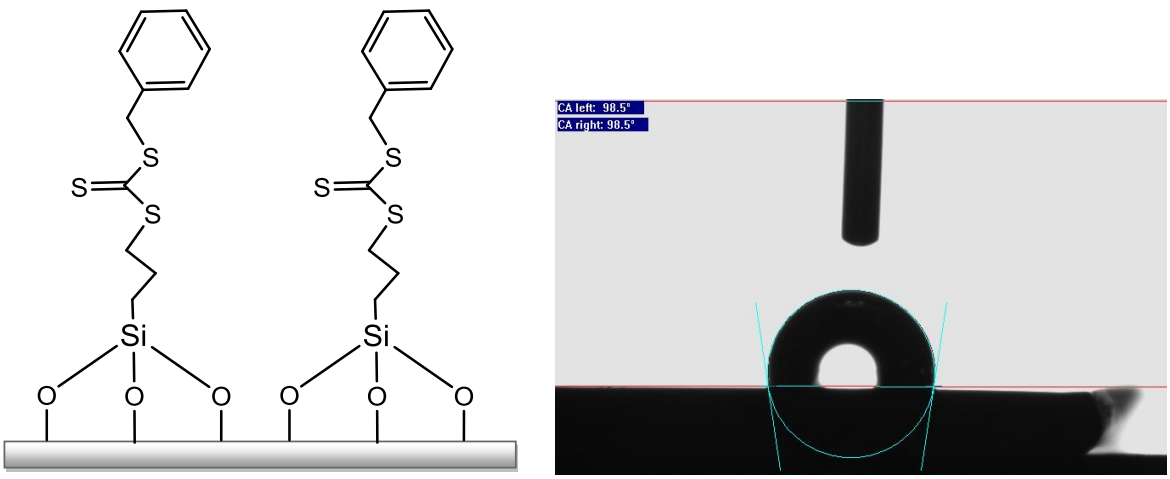

Figure 51. Contact angle (80-94°) after BTMePT functionalization

Functionalization with polymers

Values of contact angle (range 83-93°) are comparable to the BTMePT functionalized surface. The result suggests that a single layer of silane is able to influence the contact angle and that a major thickness related to the polymer chains may not increase the values (Figure 52).

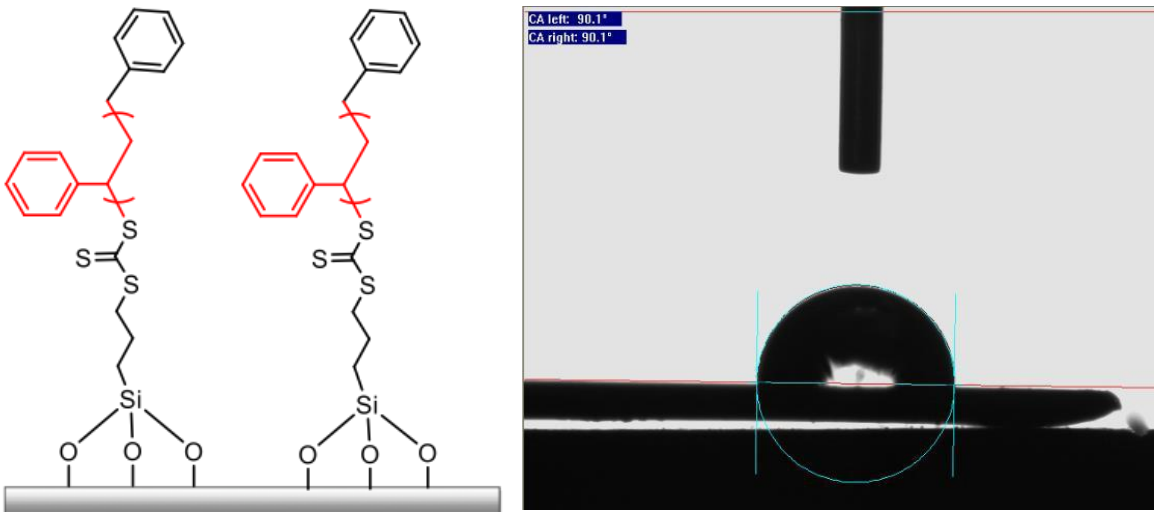

Figure 52. Contact angle (80-94°) after BTMePT and polystyrene functionalization

Atomic force microscopy (AFM)

This technique is able to provide information about the morphology of the surface. Morphology is expected to change from pristine samples to polymer functionalized samples. The polishing process particularly affects superficial roughness. AFM measurements allow comparing the same surface at different functionalization steps, making the comparison more reliable. AFM measurements were performed using the tapping mode with RTESP tip.

Pristine surfaces

As for the other measurements, pristine surfaces were polished and cleaned with piranha solution. Figure 53 shows some examples of surface appearance after the polishing process in pristine samples.

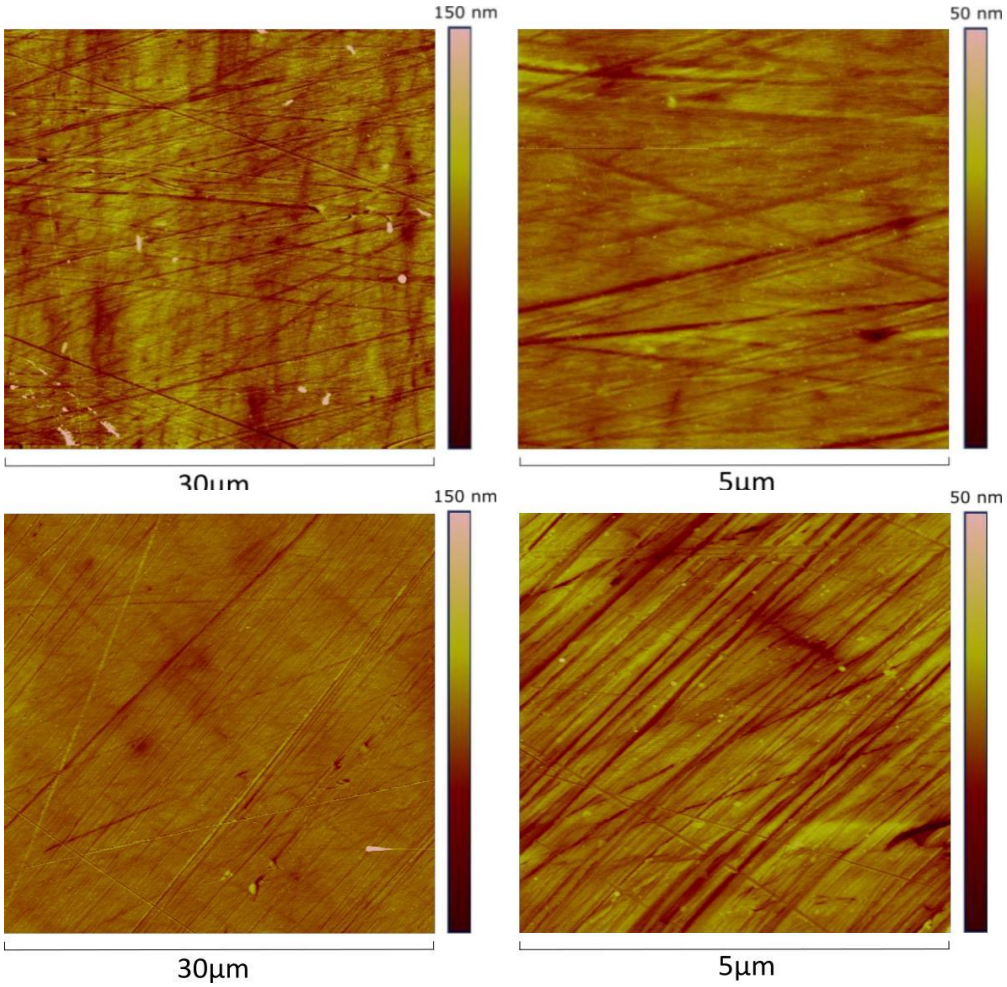

Figure 53. AFM images of the surface of pristine samples

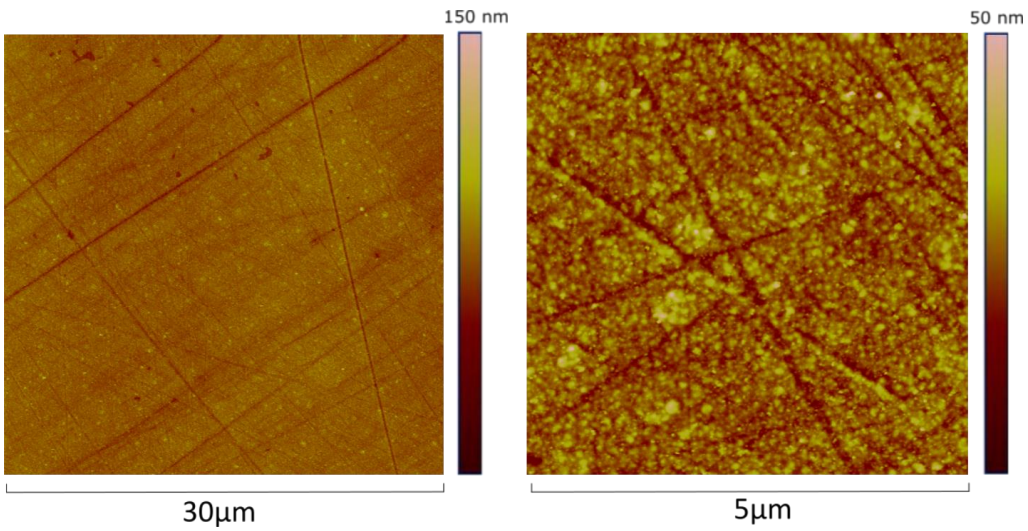

Figure 54. AFM images of the surface of polystyrene functionalized samples

Functionalization with polymers

Figure 54 shows the AFM images of PS functionalized samples.

The surface of the PS modified plate clearly differs from that one of the pristine plate. It shows a particular roughness, which is absent in the pristine samples, confirming the deposition and growth of the polymer layer on the surface of the SS plate.

X-Ray photoelectron spectroscopy (XPS)

X-ray Photoelectron Spectroscopy (XPS) provides valuable quantitative and chemical state information from the surface of the material being studied. The average depth of analysis for an XPS measurement is approximately 5 nm and is therefore better suited for the compositional analysis of ultra-thin layers and thin microscale sample features.

XPS is typically accomplished by exciting a sample surface with x-rays causing photoelectrons to be emitted from the sample surface. An electron energy analyser is used to measure the energy of the emitted photoelectrons. From the binding energy and intensity of a photoelectron peak, the elemental identity, chemical state, and quantity of a detected element can be determined.

Internal standards are often used for quantitative measures. Typical relative precisions are in the range of 5%. Generally, for qualitative determinations, the element has to be present in a percentage major than 0,1%, while for quantitative determination it has to be higher than 5%. The instrument employed for these measurements is an M-probe (Surface Science Instruments). X-ray monochromatic source was Al Kα with 1486.6 eV of photon energy. 1s Carbon peak at 284,6 eV was used to correct energy levels. Spot size in analysis was 400µmx1000µm. Wide scans and high-resolution measurements were performed.

In order to set a benchmark, SS plates were firstly analyzed. The surface provided a term of comparison for the other measurements. SS plates were only polished and cleaned with sonication in DI water, acetone and dichloromethane. No piranha solution treatment was applied.

The results showed the typical stainless steel composition (iron, chromium, carbon and silicon) with the presence of an oxide layer composed of oxygen (Figure 55).

Figure 56 shows the spectrum of Polystyrene SS functionalized plate. PS is anchored to S-benzyl-S'-(trimethoxysylil) trithiocarbonate (BTMePT).

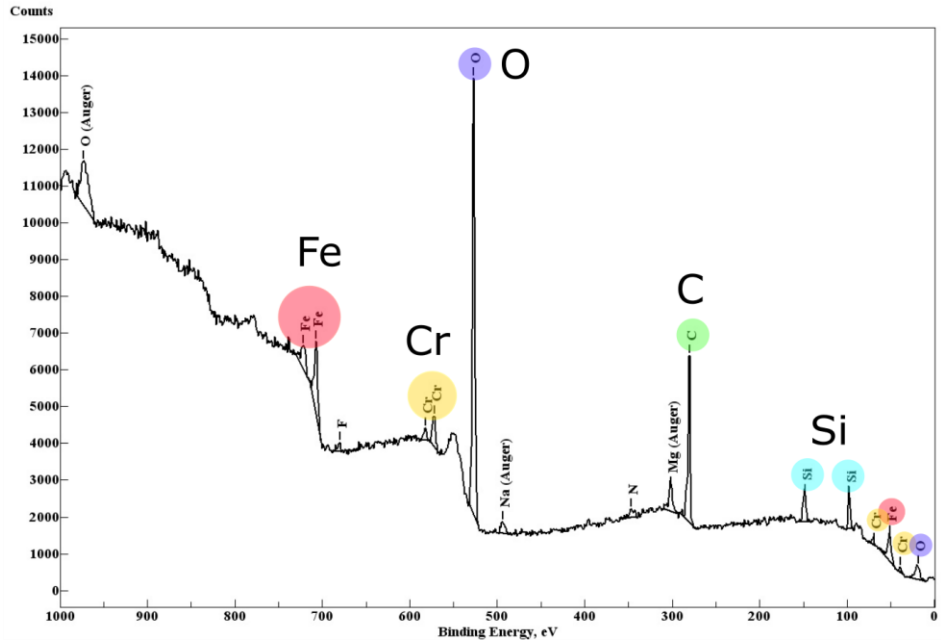

Figure 55. XPS spectrum of pristine sample

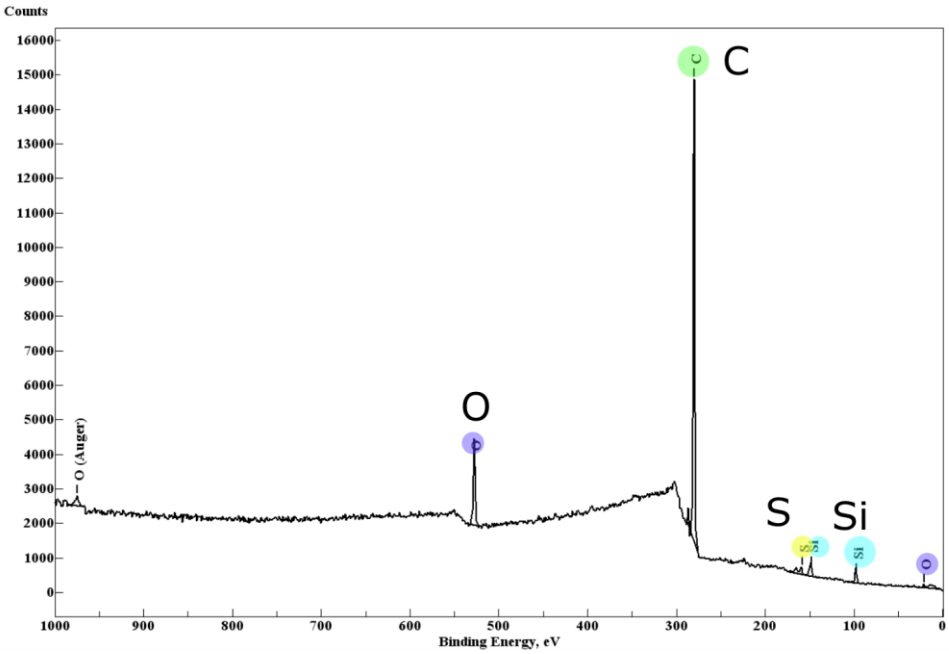

Figure 56. XPS spectrum of pristine polymer functionalized sample. Note the carbon peak

The spectrum is completely different from the pristine one. Peaks of the SS typical elements are totally absent. This means that a uniform layer completely covered the surface.

The polymer layer thickness has to be higher than 5nm, which is the penetrating depth of XPS analysis. The high percentage of carbon confirms the presence of polystyrene chains grafted to the surface. The XPS spectra demonstrate and confirm the presence of the coating.

In conclusion, it was demonstrated that *grafting from* techniques, combined with RAFT polymerization, are suitable for SS modification to improve interfacial properties. Contact angle, AFM and XPS measurements were used to verify the functionalization process. Hydrophobicity had changed as well as the surface morphology. AFM and XPS results demonstrated that a nanolayer of polymer had been attached to the SS surface. The typical 316L SS elements (Iron, Chromium, Molybdenum) were not detected after grafting process. The layer resulted uniform and dense, providing an extensive covering of the surface.

The in vitro effects on bacteria and cellular adhesion are to be verified, in order to better understand if the nanocoating is effective and which polymer is the most promising in terms of infection and fibrosis prevention.

8. Biological nanocoating activity

A sight threatening post surgical complication of trabeculectomy and/or Ex-Press implant is the possibility of infection of the bleb (blebitis) and eventually of the whole eye globe (endophthalmitis). The aim of the superficial nanocoating was to reduce bacteria and cell adhesion and/or vitality in order to reduce the possible infection rate of the device once implanted.

In order to verify the anti adhesion/vitality properties, samples were compared with pristine stainless steel (SS) plates. Pristine samples were polished with silicon carbide abrasive papers and treated with piranha solution as previously mentioned. The functionalization process is described previously. Samples were then cleaned with DI water, ethanol, acetone and DI water with sonication for 10 minutes.

Twelve samples were divided into four groups of three plates each according to the different functionalizations. The first group consisted of 316L SS pristine plates, the second consisted of plates functionalized with Polymethilmetacrylate (PMMA), the third was made up of samples functionalized with PolyN,N-dimethylacrylamide (PDMA) and the last one was composed of samples functionalized with Polystyrene (PS). Plates were numbered and each group was identified with the abbreviations previously mentioned. The examiner was blind to the treatment applied to the samples. One sample of each group was tested at each experiment. The anti-adhesive and/or vitality effect of functionalized disks was evaluated by a microbiological assay which provides viable counts of bacteria adhering to the various types of samples, comparing them with the results obtained on a control disk without any functionalization.[81] Briefly, a mid-log phase bacterial culture of *Staphylococcus Aureus* ATCC 25923 in Mueller-Hinton (MH) broth was centrifuged at 1000 x g for 5 min and re-suspended in phosphate buffered saline (PBS) up to a value of optical density (OD) at 600 nm equal to 0.1 (~ 10^7 cells/ml). The suspension thus obtained (T0) was plated, after appropriate dilutions, on MH agar to obtain the cellular concentration (expressed as Colony Forming Units/ml, CFU/ml) of the initial suspension in which the various disks were then immersed. Two ml of this suspension were aliquoted in a 12-multiwells plate in which were subsequently immersed the functionalized and control disks after UV sterilization. The multiwells plate was incubated in a thermostat at

37°C for 3 hours under static conditions to allow bacterial adhesion to the disks. After incubation, the disks were collected with sterile tweezers, subjected to a weak washing with PBS (soft washing to remove non-adherent bacteria) and then transferred to a Falcon tube containing 2 ml of PBS, in which they were vortexed vigorously for 30 sec to allow the detachment of bacteria from the support (strong washing). After appropriate serial dilutions in PBS, the bacterial suspensions were plated on MH agar and the Petri plates were incubated overnight at 37°C to allow the viable colony counts. The values reported are the mean ± standard deviation of three independent experiments. One set of plates was then washed and sterilized again and the experiment was repeated as described above.

For statistical purposes, the mean value of CFU recovered from pristine samples was used as a baseline against which the functionalized samples were compared (Table 6). The delta among them was expressed as a percentage (Table 7). Data obtained from four different experiments were subjected to computer-assisted analysis using Graph Pad Instat 3. Statistical significance was assumed at $p < 0.05$ (ANOVA, Student-Newman-Keuls post test).

Results are summarized in Tables 6 and 7 and graphically presented in Graphs 1 and 2.

	E1	**E2**	**E3**	**E4**	**Mean**	**SD**
T0	3.60E+07	2.40E+07	7.00E+07	3.30E+07	4.08E+07	20155644.4
SS	2.30E+06	1.50E+06	1.60E+06	1.90E+06	1.83E+06	359397.6
PMMA	2.00E+06	1.80E+06	1.50E+06	1.60E+06	1.73E+06	221735.6
PDMA	1.70E+06	1.40E+06	1.30E+06	1.50E+06	1.48E+06	170782.5
PS	1.20E+06	7.00E+05	9.10E+05	1.10E+06	9.78E+05	220661.9

Table 6. Results are expressed in CFU/mL. T0 = initial bacteria suspension. E1 to E4 = number of experiments

	E1	**E2**	**E3**	**E4**	**Mean**	**SD**
SS	100	100	100	100	100	0
PMMA	87.0	120.0	93.8	84.2	96.2	16.3
PDMA	73.9	93.3	81.3	78.9	81.9	8.2
PS	52.2	46.7	56.9	57.9	53.4	5.1

Table 7. Percentage of viable bacteria recovered after adhesion on functionalized plates compared to pristine samples. E1 to E4 = number of experiments

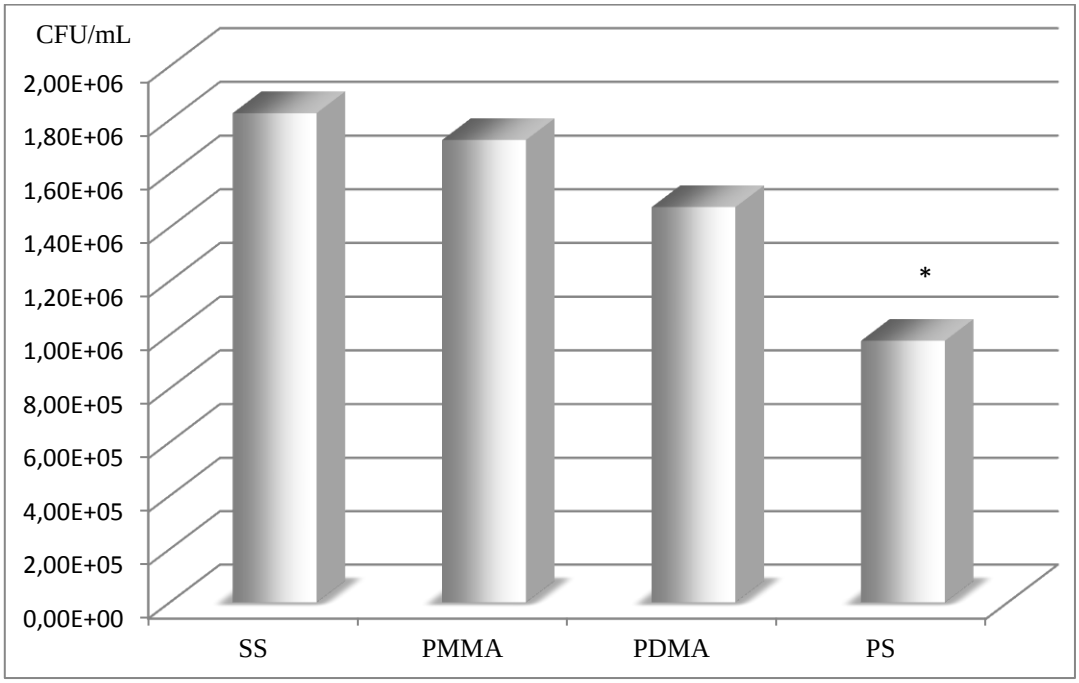

Graph 1. CFU/mL for SS pristine, PMMA, PDMA and PS samples (* $p<0.05$)

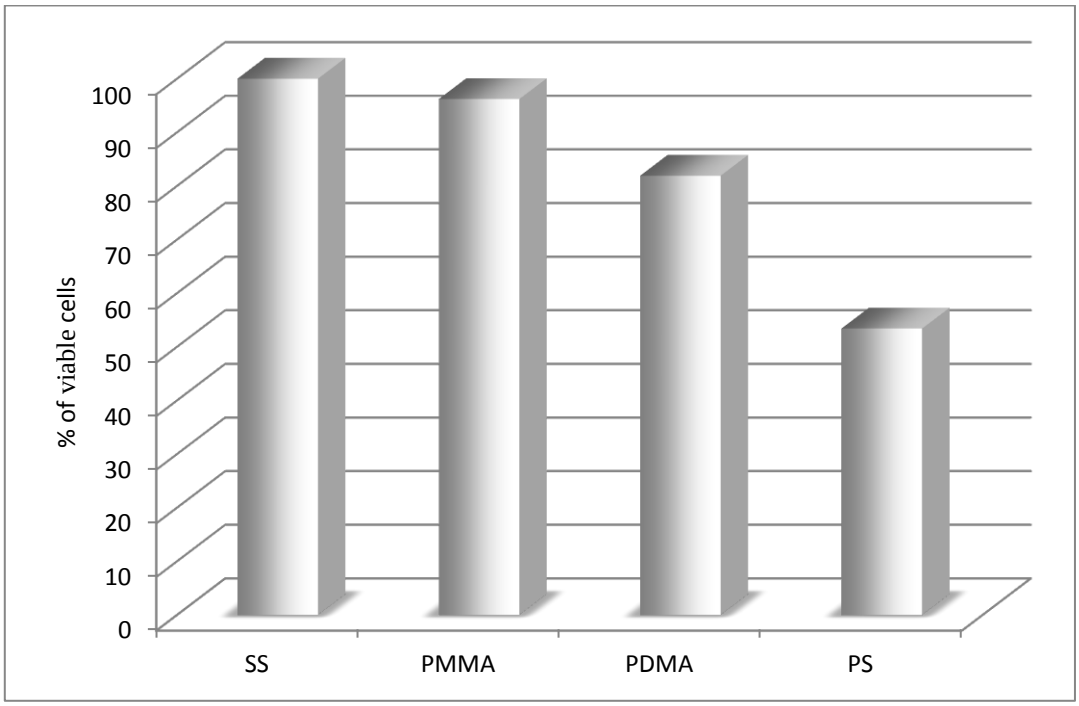

Graph 2. Percentage of viable bacteria recovered after adhesion on PMMA, PDMA and PS samples compared to Pristine (SS) samples

A statistically significant difference (p=0.007) was observed between the PS functionalized plates and the SS pristine samples. The percentage of reduction of viable bacteria was 3.8% in PMMA group, 18.1% in PDMA group and 46.6% in the PS group when compared to SS pristine samples.

The results demonstrated that the samples treated with polystyrene showed the highest efficacy in reducing bacteria adhesion or bacteria vitality. The other groups showed similar results with no statistically significant difference among them. Nonetheless, the pristine plates presented the highest bacteria adhesion/vitality followed by the PMMA group. The experimental approach used is based on the vitality of recovered bacteria after adhesion on the samples. This technique considers the viable bacteria, and therefore it is not possible to differentiate between an anti-adhesive or a bactericide-like effect. In other words, less viable bacteria could be found due to less adhesion on the samples, or due to an effect on the vitality of bacteria, which may adhere to the surface but are not vital anymore.

Scanning electron microscopy (SEM)

The aim of the SEM analysis was to qualitatively observe whether the treatment had any visible impact on bacteria adhesion. For this preliminary study, two plates of each type were used, divided into two groups (A and B) of 4 plates each. Each group was therefore composted of 1 pristine SS (non functionalized) plate, 1 PS, 1 PMMA and 1 PDMA functionalized plates.

Plates of both groups were immersed in the bacteria broth as aforementioned. Subsequently, samples in group A were fixed as described here after, while samples in group B were put in a vortex for 30 seconds in order to detach the non adherent bacteria before the fixing procedure (similarly to the procedure adopted for the viable bacteria count previously described).

Samples were prepared for SEM according to the following procedure: plates were air dried and fixed in 2.5% glutaraldehyde in PBS for 1 hour at room temperature. At the end of the fixation step, samples were rinsed three times with PBS for 15 min, and dehydrated in ethanol solutions of increasing concentrations (30%, 50%, 70%, 80% and 100%) for 10 min at each concentration. After removal of absolute ethanol, all samples were covered with an appropriate volume of hexamethyldisilazane (HMDS) as a drying agent.

Figures 57 and 58 show the bacteria residual adhesion on the SS pristine and functionalized plates, with and without the vortex procedure. From a merely speculative point of view, it seems that the bacteria adhesion was similar in all samples in the two groups. After the vortex procedure the residual amount of bacteria adhered to the surface seems to be reduced (Figure 57). This reduction appears to be qualitatively similar in all the samples.

This assumption has to be further verified, as this was a preliminary experiment taking into account a limited number of plates. If confirmed, it would suggest that polystyrene nanocoating is very effective in reducing *Staphylococcus Aureus* vitality to almost 50%, rather then acting on bacteria adhesion.

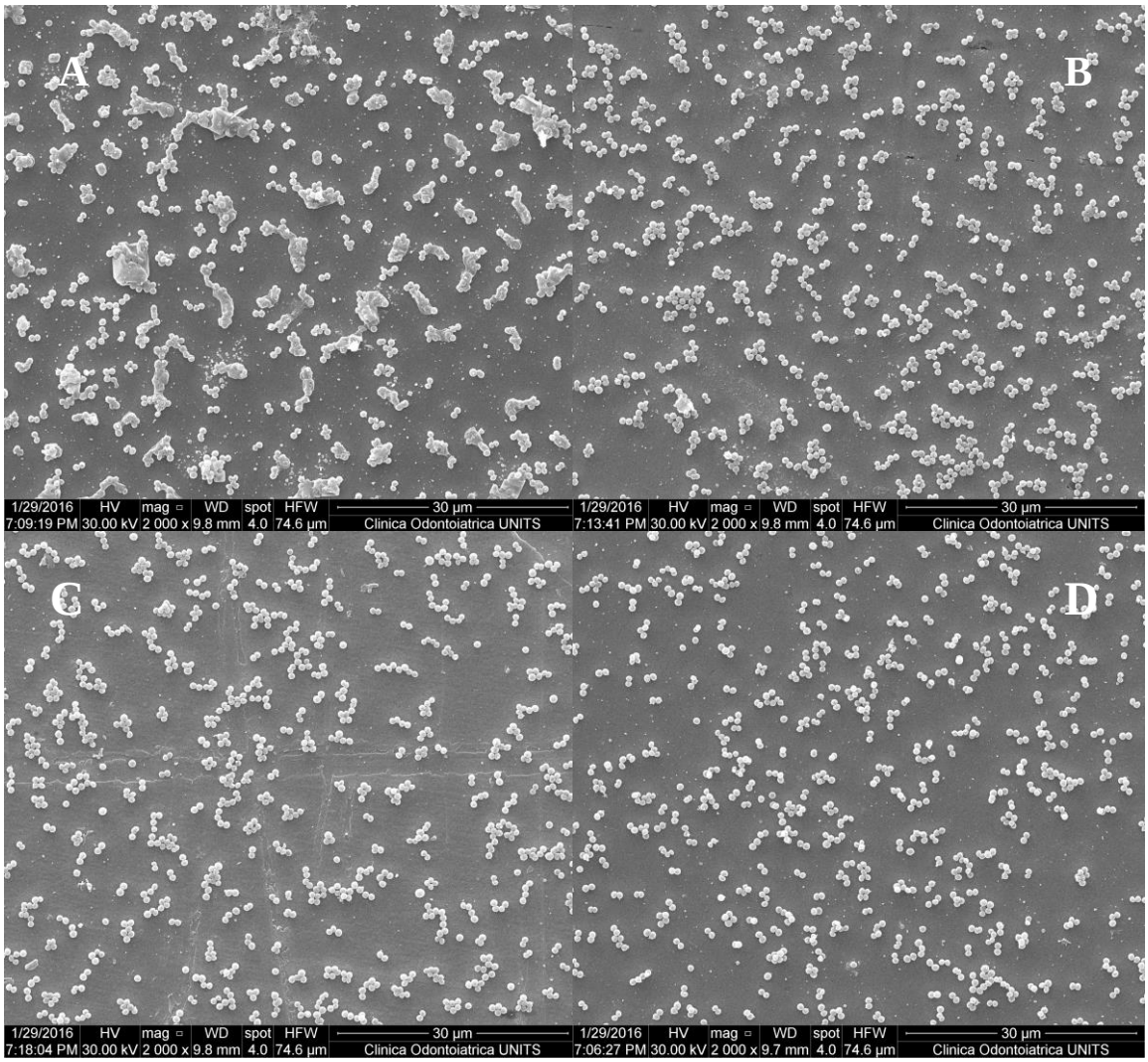

Figure 57. SEM images of bacteria adhesion on pristine (A), PMMA (B), PDMA (C) and PS (D) samples.

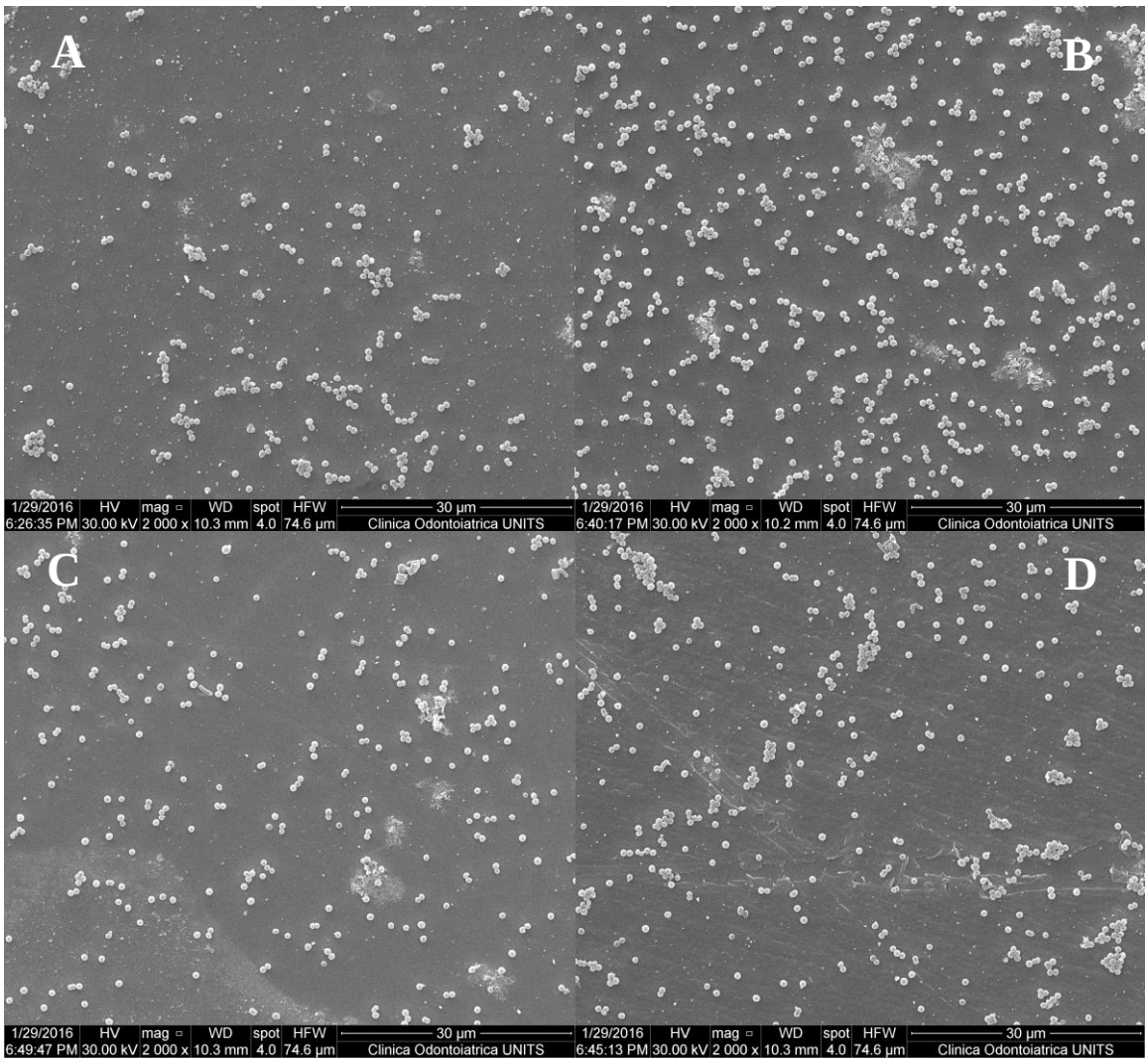

Figure 58. SEM images of bacteria adhesion after vortex procedure on pristine (A), PMMA (B), PDMA (C) and PS (D) samples.

9. Conclusions

The Ex-Press glaucoma shunt is the most promising alternative to trabeculectomy. It appears as a small stainless steel device that is implanted in the irido-corneal angle under a sclera flap. At SEM imaging a high degree of roughness was observed on the surface of the internal lumen. This was the first attempt to analyze the finishing of the Ex-Press shunt and to verify the internal lumen. It proved to be of constant diameter and no valve system was observed. The internal roughness may cause cell adhesion and fibrin deposition, eventually leading to obstruction of the device and failure of the surgery. Cell adhesion was studied with the use of cell cultures of fibroblasts. A limited degree of cell adhesion was demonstrated on the inner lumen of the device. On an explanted Ex-Press device a discrete amount of biological extracellular matrix was observed. Energy-Dispersive X-ray Spectroscopy was used to demonstrate the presence of carbon on the device, confirming the biological origin of the debris. The explanted device showed some superficial pits, which are a sign of initial corrosion. These observations would suggest that the shunt construction material and finishing process might not be adequate for a high-standard biocompatibility.

It is worth mentioning that a massive bacterial contamination occurred during the experiments and that the device may represent a possible vehicle for infection transmission in vivo.

The outflow pathways after trabeculectomy and Ex-Press implant are still under debate. In this work, multiple computational models were created in order to study the effect of the scleral flap and the sutures position on the filtration rate. A 2D model and a 3D model were studied to simulate the outflow of aqueous humor from the eye. The role of the suture placing in determining the pathways of outflow was demonstrated. The 3D model was useful to better understand the deformation of the scleral flap and suggested a role of the head position on the outflow pattern. Most of the outflow was estimated to occur at the sides of the scleral flap, within 2 mm from the corneal side.

Up to few years ago, there was no possibility to study “in vivo” the draining site through the scleral flap and the bleb formation. The anterior segment optical coherence tomography (AS-OCT) has recently allowed for a more detailed comprehension of the

novel aqueous humor pathways formed after surgery. Recent computational models[82-84] reported that most of the time there is only one outflow pathway on one side of the scleral flap, whereas, in a minority of cases, both sides present a drainage point. In these studies, a triangular shape flap was considered. Other reports, have modelled the trabeculectomy procedure. An interesting paper,[83] focused on modelling the bleb function after trabeculectomy. The aim was to correlate the filtering bleb outcome seen clinically to a predictive model. The authors found that small, thick wall blebs were likely to be less effective and possibly to allow less fluid to be absorbed by tissue. These results suggested that small blebs expose tissue to high pressures, particularly directly above the bleb, inducing an ischemic tissue remodeling response. This event may lead to a non-functioning bleb and surgical failure. Conversely, large blebs were less likely to undergo to this remodeling process but may lead to an excessive filtration rate. These results were consistent with bleb characteristics seen clinically. Other authors[84] have investigated the best shape and dimension of the scleral flap in order to ideally obtain a diffuse conjunctival bleb with effective drainage. Their conclusion was that a 4x4 mm rectangular flap was more effective than any triangular shape flap. Our study aimed to understand the outflow patterns that occur under the flap, assuming that the rectangular shape flap is the most widely used in clinic and the most promising also in computational simulations. This is the first attempt that has taken into account the patient position, simulating the outflow both by standing and supine positions. This gives new clues of what may happen during nighttime. The other goal was to understand the role of stiches in limiting the aqueous flow. Usually surgeons rely on their experience in deciding where to put stitches and how many stitches are required. Our simulation is consistent with what can be observed in vivo with AS-OCT. Most of the flow occurs close to the cornea, and very little posteriorly. This is relevant as the maximum flow is seen very close to the conjunctival suture, and may interfere with the healing process. A more posterior flow may be an advantage. The simulation also suggests that an outflow device with a drainage site placed centrally under the flap would be an improvement in terms of an even distribution of the flow and pressure fields.

Subsequently, a nanocoating system was planned in order to reduce cell and bacterial adhesion or their vitality on the device. The procedure allowed for the grafting of different polymer layers with potential biological activity. Monomers employed were styrene, methylmethacrylate and N,N-dimethylacrylamide. The experiments were carried out on

stainless steel (SS) 316L 1x1 cm plates, in order to test the same material of the device, but with easier handling. *Grafting from* technique was used. Samples were characterized with contact angle measures, atomic force microscopy and X-ray Photoelectron Spectroscopy.

As many artificial materials, SS316L may provide a good substrate for bacteria and cell proliferation. Surface chemistry modification that could prevent such events and reduce the material corrosion is therefore desirable. In the literature it is under debate whether hydrophobicity may increase or decrease cell adhesion. Some authors[85] proposed that more proteins adhere on hydrophobic surfaces due to the hydrophobic effect. Briefly, proteins would be expelled from the aqueous solution and displace water from the hydrophobic surface, being adsorbed. Conversely, other papers[86,87] showed that a hydrophobic coating was effective in reducing cell adhesion. Similarly,[88] in cataract surgery, it has widely demonstrated that hydrophobic intraocular lenses have a lower rate of posterior capsule opacification (PCO). PCO is due to the growth and abnormal proliferation of lens epithelial cells (LECs) on the posterior capsule, with the deposition of extracellular matrix. These events promote the clouding of the posterior lens capsule. In our experiments, an increase in hydrophobicity, a modification in the XPS and a diffuse deposition of the nanolayer were observed, demonstrating the effectiveness of the procedure.

Subsequently, the biological effects of the functionalization with different polymers were tested by means of bacteria adhesion and vitality experiments.

The results showed that the Polystyrene treated plates demonstrated the lowest bacterial count expressed as CFUs, while the effect of Polymethylmethacrylate and PolyN,N-dimethylacrylamide was less evident. The reduction in CFU was nearly 50% when compared to pristine SS samples. It is not possible to know if the effect observed was directly due to less bacteria adhesion on the PS samples, or if the PS nanocoating determined a substantial decrease in bacteria vitality. The SEM images would support an effect on vitality rather then on adhesion, but the limited number of samples considered, the small area studied for each sample, and the qualitative results obtainable are not sufficient to clearly validate this alternative.

In conclusion it has been demonstrated that it is feasible to build a biologically active nanocoating using different polymers on SS 316L plates. The nanocoatings appeared to be

stable and uniform. The biological experiments were consistent in demonstrating a statistically significant reduction in the viable bacteria after polystyrene functionalization. The exact effect of PS on bacteria is yet to be understood. Further studies are required to differentiate if the PS biological activity is to be ascribed to an anti-adhesive effect or conversely if PS acts on bacteria vitality.

Appendix A

Materials used in nanocoating experiments

Department nitrogen, dried with zeolites traps was used for inert atmosphere reactions.

Solvents

Anhydrous N,N-dimethylformamide from Sigma Aldrich 99,8%; anhydrous toluene from Sigma Aldrich99,8 %; tetrahydrofurane from Sigma Aldrich; chloroform D from Sigma Aldrich 99,96 atom% D stored at 4°C; Diethyl ether from Sigma Aldrich

Reagents

316L stainless steel with standardized properties and composition; Poly (ethylene glycol) methyl ether acrylate (PEGA) from Sigma-Aldrich; Di-(ethylene glycol) ethyl ether acrylate (DEGA) >90% from Sigma-Aldrich; 3-(trimethoxysilyl) propyl methacrylate >98% from Fluka; 2,2'-Azo-bis-isobutyronitrile (AIBN) 98% from Sigma Aldrich recrystallized in methanol and stored at 4°C; Chloro trimethylsilane >97% from Sigma Aldrich; Chloro-decyl-dimethylsilane >97.0% (GC) from Sigma Aldrich; S-dodecyl-S'-(α,α'-dimethyl-acetic acid) trithiocarbonate synthesized and characterized in laboratory; Hydrogen peroxide from Sigma Aldrich 30 wt% in H20 ; Sulfuric acid 98% .

Instruments

Varian Cary 50 UV-Visible spectrophotometer, Perkin Elmer Spectrum 100 FT-IR spectrometer, Veeco Nanoscope V multimode AFM, Gel permeation chromatograph WATERS 1515 isocratic equipped with a HPLC Pump; Surface Science M-Probe XPS/ESCA. Dataphysics OCA 20 for contact angle. METTLER TOLEDO DSC 3+; NMR 500 MHz Bruker Avance wide bore.

Appendix B

Constitutive scleral flap 3D model

Geometry

The geometric model of a 4mm×4mm×0.5mm flap is shown in Figure 59. The flap is cut out from a hollow sphere, with inner and outer radii 12mm and 12.5mm, respectively. The model geometry is highly idealized and does not take into account the inherent inaccuracy of any surgical cut. It will become apparent that the removal of some tissue from the sides and the bed of the scleral flap could be relevant in the formation of a flow pathway. This could be ascribed to the surgical cutting along the perimeter of the flap and to the *forth-and-back* cutting pattern generally used to *sculpt* the flap from the tissue underneath. These geometrical *defects*, caused by the surgeon, are substantially unpredictable but could be represented as relatively simple modifications to the base shape shown in Figure 59. Thus, a parameterization of the defects is feasible but not pursued in the present work.

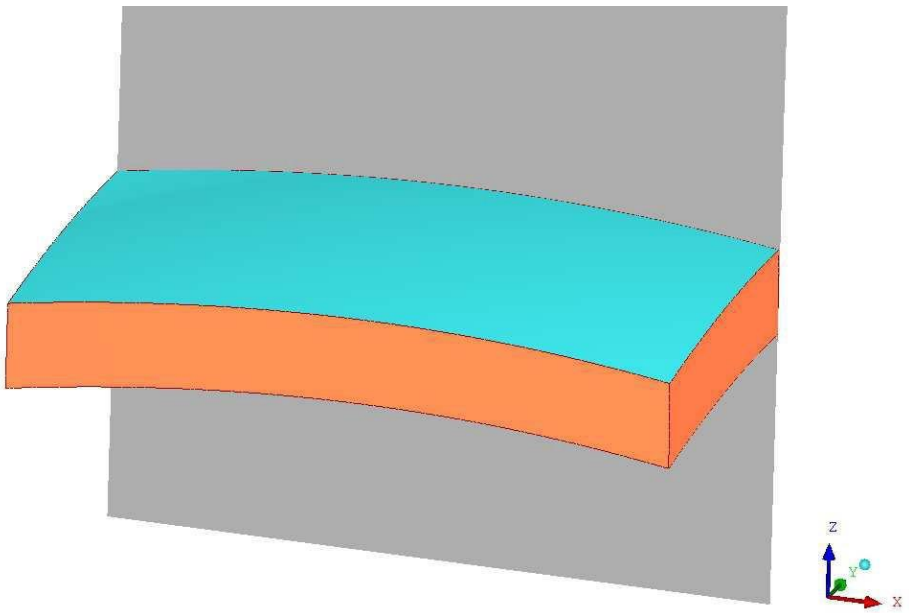

Figure 59. Geometric model of the scleral flap. Due to geometric and load symmetries, only half model is shown, the symmetry plane appearing in grey.

Constitutive model

Wollensak and Spoerl[89] and Spoerl et al.[90] measured the Young's modulus of human scleral

tissue using uni-axial techniques, reporting values of 22.82MPa and 28.9MPa, respectively. Due to the complex behavior of most tissues, such as anisotropy and non-linearity, data from uni-axial tests cannot fully describe the mechanical properties of tissue specimens, even if the stress-strain relationship is measured in different directions. Therefore, other techniques are also used for studying the material properties of scleral tissue. Woo et al.[91] pressurized the posterior segment of the human eye mounted on a metal chamber and used a flying spot scanner system to measure the scleral surface deformation as a result of increasing internal pressures. A non-linear stress-strain behavior is reported for the scleral tissue and a tri-linear model for scleral elasticity is suggested, in which the effective modulus varies from 0.9 to 2.7 MPa. Using a similar technique Kobayashi et al.[92] measured an elastic modulus of 5.5 MPa for human scleral tissue. In a recent study, Girard et al.[93] showed non-linear stiffness behavior in porcine scleral samples using a two-dimensional surface mapping technique. Their results suggest that scleral stiffness is low at IOPs less than 10 mmHg but dramatically increases beyond this pressure. Battaglioli and Kamm[94] measure the radial stiffness of human scleral tissue using unconfined compression. The measured compressive radial modulus is more than two orders of magnitude less than the average elastic modulus reported from extensional tests for human scleral tissue and varies in the range 0.027-0.041 MPa. They also measured the Poisson ratio of the scleral samples and found a range of 0.46-0.5, suggesting an almost incompressible behavior for human sclera tissue. Eilaghi[95] showed that the rheological behavior of the scleral tissue is well approximated by an isotropic, five-coefficient, hyper-elastic Mooney-Rivlin model.

Experimental tests of scleral biomechanical properties, although limited in number, showed significant variability in results, which could be due, at least partly, to variations in methodology, sample preparation, testing protocols (i.e. range of the applied load or strain) and inter-donor variations.

Due to the extremely limited deformation of the flap encountered in the present investigation, a linear-elastic, isotropic material is assumed, yielding the stress-strain relationship:

$$\sigma_{ij} = \frac{E}{1+v}\left\{\varepsilon_{ij} + \frac{v}{1-2v}\varepsilon_{kk}\delta_{ij}\right\} - \frac{E\alpha\Delta T}{1-2v}\delta_{ij} + \sigma_{ij}^{0} \qquad (1)$$

where σ^0 denotes the initial stress. Representative values of the Young's modulus and Poisson's ratio are used: E = 36MPa, ν = 0.49.

The flap is modelled as a three-dimensional solid. Plane-stress approximations (i.e., plate theory assumptions) are not applied. The ensuing equilibrium equations and boundary conditions are:

Equilibrium equations

The equilibrium equations in differential form are:

$$\frac{\partial \sigma_{ij}}{\partial x_j} + f_i = 0 \tag{2}$$

where f_I denotes a generic body force. In the present model the only considered body forces are due to the surgical stitches, equation (8). The action of gravity is neglected, as the total weight of the flap is approximately $\rho V g = 1000\ kg/m^3 \times 4\ mm \times 4\ mm \times 0.5\ mm \times 9.81\ m/s^2 \approx 8 \times 10^{-5}$ N, to be compared with the pressure force on the bottom side of the flap, given by $pA = 2\ kPa \times 4\ mm \times 4\ mm = 3.2 \times 10^{-2}$ N.

Constraints

The flap is constrained on its left boundary $\Gamma 0$, where it is attached to the surrounding tissue. In the physical model, this boundary is considered as fixed, i.e., the displacement of the material points on it is identically zero:

$$\mu\,(x) = 0\ \forall x \in\ \Gamma_0 \tag{3}$$

This simplification does not take into account the deformation of the surrounding tissue.

The lateral and the bottom sides of the flap, $\Gamma 1$ and $\Gamma 2$, respectively, are considered as free boundaries:

$$\sigma(x) \cdot n\,(x) = 0 \forall x \in\ \Gamma_1 \cup\ \Gamma_2 \tag{4}$$

As the mathematical model encompasses only half of the flap, symmetry conditions are enforced on the symmetry plane $\Gamma 3$, located at $y = 0$. The general rule for a symmetry

displacement condition is that the displacement vector component perpendicular to the plane is zero and the rotational vector components parallel to the plane are zero, i.e.:

$$u(x) \cdot n(x) = 0 \; \forall x \in \Gamma_3 \tag{5}$$

$$R(x) \cdot \tau_{1,2} = 0 \; \forall x \in \Gamma_3 \tag{6}$$

where $\tau_{1,2}$ denote two linearly-independent tangential directions to the symmetry plane.

Loads

The bottom side of the flap, $\Gamma 2$, is loaded by the fluid pressure, while the action of viscous forces is neglected:

$$n(x) \cdot \sigma(x) \cdot n(x) = -p(x) \forall x \in \Gamma_2 \tag{7}$$

Furthermore, the flap is also under the strain generated by the surgical stitches, which are modeled as concentrated body forces. Surgical stitches are represented by a rough, yet simple and computationally efficient, three-dimensional, spring-like body force, with very narrow support:

$$f(x) = \max(-K\tau \cdot u, 0)\, G(x)\, \tau \tag{8}$$

where

$$G(x) = \frac{1}{2\pi t \sigma^2} \exp\left[-\frac{\left[(x-x_S)^2 + (y-y_S)^2\right]}{2\sigma^2}\right] \tag{9}$$

and

$$\int_{R^3} G(x)\, dx = 1 \tag{10}$$

The coordinates x_S and y_S define the horizontal position of the junction points on the flap. K represents the spring stiffness, while the *standard deviation* σ defines the size of the influence region of the body force about (x_S, y_S). The units vector τ defines the line of action of the force and is conceived as follows:

$$\tau' \equiv \begin{cases} x_s' - x_s \\ y_s' - y_s \\ -\omega \end{cases}; \quad \tau \equiv \frac{\tau'}{\|\tau\|} \tag{11}$$

Three common configurations of the surgical stitches are considered, using two, three and five stitches to constrain the flap.

Pre-stressing

A planar-isotropic pre-stress state is considered:

$$\sigma^0 = \begin{bmatrix} \sigma^0 & 0 & 0 \\ 0 & \sigma^0 & 0 \\ 0 & 0 & 0 \end{bmatrix} \tag{12}$$

A reasonable estimate for σ^0 is achieved by considering the deformation of a thin disk of linear elastic material, uniformly and radially loaded at its outer boundary.

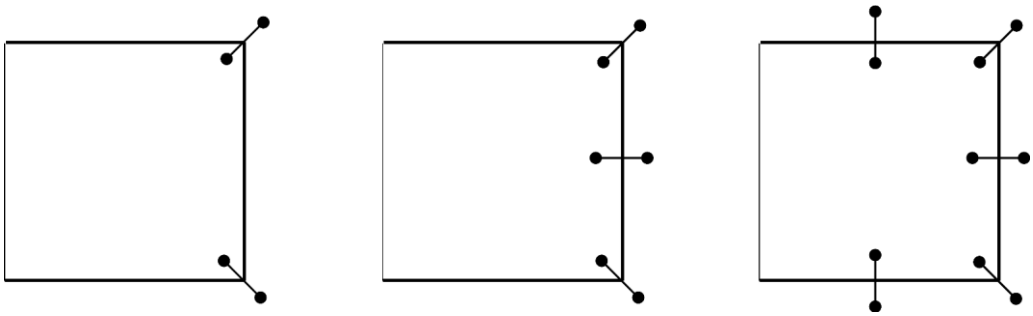

Figure 2: Three common configurations of the surgical stitches.

Assuming a plane-stress state, while taking into account the axial symmetry of the problem, the following radial equilibrium and compatibility equations are obtained, respectively:

$$\frac{d\sigma_{rr}}{d_r} + \frac{\sigma_{rr}}{r} - \frac{\sigma_{\vartheta\vartheta}}{r} = 0 \tag{13a}$$

$$\frac{d\varepsilon_{\vartheta\vartheta}}{dr} = \frac{1}{r}[\varepsilon_{rr} - \varepsilon_{\vartheta\vartheta}] \quad (13b)$$

The boundary condition on the outer boundary of the disk, $r = re$, is:

$$\sigma_{rr}\ (r = r_e) = \sigma^0 \quad (13c)$$

Solving equations (13) yields:

$$\sigma_{rr} = \sigma_{\vartheta\vartheta} = \sigma^0 \quad (14a)$$

$$\varepsilon_{rr} = \varepsilon_{\vartheta\vartheta} = \frac{1-v}{E}\sigma^0 \quad (14b)$$

While the radial displacement at the outer boundary is

$$u(r) = \frac{1-v}{E}\sigma^0 r_e \quad (14c)$$

$u(re)$ = 50 μm is assumed as a representative value for the shrinking of a circular disk 4mm in diameter, made of scleral tissue, after surgical cut. Substituting E = 36MPa, v = 0.49, re = 2mm, $u(re)$ = 50 μm in equation (14c) yields the prestress $\sigma^0 \approx$ 1.76MPa, which is applied in the reported simulations.

Finite element structural model

The equilibrium equations (2) are solved numerically by a finite-element method, implemented in the commercial software COMSOL Multiphysics. A mixed $u-p$ algorithm is used, which is known to avoid problems of *locking* when dealing with nearly incompressible materials, as in the present simulations. Tetrahedral $U3P2$ elements are used, where the components of displacement are approximated by third-order, interpolating polynomials while the pressure is approximated by quadratic, interpolating polynomials. Each simulation has been repeated on three progressively finer meshes, in order to ascertain grid independence.

Fluid dynamics model

The considered flow configuration is shown in Figures 26-32. Under some load

configurations, a gap forms between the deformed flap and the intact tissue, allowing for the flow of aqueous humor. Due to the very low expected volume, flow rates and fluid velocities, a laminar, stationary flow model is assumed. A single-phase flow is assumed, as the aqueous humor flows under the conjunctiva.

Constitutive equations

The aqueous humor is modeled as an incompressible, Newtonian fluid with the constant kinematic viscosity of water at 37◦C: ν = 0.696 × 10−6 m2/s. The well-known stress-rate of strain relationship for non-polar, isotropic fluids is used:

$$\sigma_{ij} = -p\delta_{ij} + 2\mu\varepsilon_{ij} \tag{15a}$$

where the rate of strain tensor is defined as

$$\varepsilon_{ij} = \frac{1}{2}\left[\frac{\partial u_i}{\partial x_j} + \frac{\partial u_j}{\partial x_i}\right] \tag{15b}$$

Governing equations

The well-known Navier-Stokes equations for incompressible, Newtonian fluids are solved under stationary conditions:

1. Mass conservation:

$$\frac{\partial u_j}{\partial x_i} = 0 \tag{16a}$$

2. Momentum conservation:

$$\frac{\partial(u_i u_j)}{\partial x_j} + \frac{\partial \sigma_{ij}}{\partial x_j} + f_i = 0 \tag{16b}$$

Substituting (15) into (16b) yields the governing equations for the present flow configuration:

$$\frac{\partial(u_i u_j)}{\partial x_j} + \frac{1}{\rho}\frac{\partial p}{\partial x_i} - v\frac{\partial^2 u_i}{\partial x_j \partial x_i} + f_i = 0 \tag{17}$$

Gravity is the only body force considered in the present investigation:

$$f_{i=g_i} \tag{18}$$

As the fluid is incompressible, a modified pressure $p' \equiv p - \rho\, g_i\, x_i$ can be used in place of the thermodynamic pressure equation (17), yielding:

$$\frac{\partial(u_i u_j)}{\partial x_j} + \frac{1}{\rho}\frac{\partial p}{\partial x_i} - \nu\frac{\partial^2 u_i}{\partial x_j \partial x_i} + = 0 \tag{19}$$

Boundary conditions

No-slip conditions apply on the solid boundaries of the flap and of the intact, surrounding tissue, Γw:

$$u(x) = 0\ \forall x \in\ T_\omega \tag{20}$$

The average static pressure is set on the boundaries open to the atmosphere, Γa, while the stagnation pressure is assigned on the inlet boundary, Γ u:

$$p'(x) = 0\ Pa\ \forall x \in\ T_a \tag{21}$$

$$p_0'(x) = 2000\ Pa\ \forall x \in\ T_u \tag{22}$$

where

$$p_0\ \equiv p + \frac{1}{2}\rho u^2 \tag{23}$$

Symmetry conditions are applied at the y = 0 boundary, Γs:

$$u(x) \cdot n(x) = 0;\ u(x) \cdot \tau(x) = 0 \forall x \in\ T_s \tag{24}$$

where n and τ denote the unit vector normal to the surface and a generic unit vector tangent to the surface.

Finite volume fluid dynamics model

The commercial, finite-volume software ANSYS-Fluent is used for solving the fluid dynamics problem. The following spatial-discretization schemes are adopted:

- second-order upwind scheme for the advection term
- least-squares scheme, based on linear approximation functions, for the viscous stress term
- linear interpolation of pressure onto the control volume faces from the two surrounding stitches, to approximate the pressure gradient in the momentum equations

The momentum and mass-conservation equations are decoupled via the Semi-Implicit Method for Pressure-Linked Equations (SIMPLE) approach.

Due to the co-located arrangement of the velocity components, the onset of non-physical oscillations is prevented by approximating the mass-flow rates at the control volume faces in the continuity equation by the method proposed by Rhie and Chow[96]. The computational mesh is generated with the open source software snappyHexMesh and is composed of cubes and (relatively) few polyhedrons.

References

1. Tham YC, Li X, Wong TY, et al. Global prevalence of glaucoma and projections of glaucoma burden through 2040: a systematic review and a meta-analysis. Ophthalmology. 2014;121:2081–2090.
2. Demea H, Demea S, Holonee R, et al. Glaucoma risk-correlations between measurements from optical coherence tomography and ocular response analyzer. IFMBE Proceedings. 2014;44:63-68.
3. The AGIS Investigators. The Advanced Glaucoma Intervention Study (AGIS): 7. The relationship between control of intraocular pressure and visual field deterioration. The American Journal of Ophthalmology. 2000;130:429–440.
4. Weinreb RN, Aung T, Medeiros FA. The Pathophysiology and Treatment of Glaucoma. A Review JAMA. 2014;31:1901–1911.
5. Weinreb RN, Khaw PT. Primary open-angle glaucoma. Lancet. 2004;363:1711–1720
6. Johnson M, Erickson K. Mechanisms and routes of aqueous humor drainage. In: Albert DM, Jakobiec FA, editors. Principles and practice of ophthalmology. Philadelphia: WB Saunders; 2000.
7. Goel M, Picciani RG, Lee RK, et al. Aqueous Humor Dynamics: A Review. Open Ophthalmol J. 2010;4:52–59.
8. Leske MC, Heijl A, Hyman L, et al. Predictors of long-term progression in the Early Manifest Glaucoma Trial. Ophthalmology. 2007;114:1965–72.
9. Lichter PR, Musch DC, Gillespie BW, et al. Interim clinical outcomes in the Collaborative Initial Glaucoma Treatment Study comparing initial treatment randomized to medications or surgery. Ophthalmology. 2001;108:1943–53.
10. Medeiros AF, Alencar LM, Zangwill LM, et al. The Relationship between Intraocular Pressure and Progressive Retinal Nerve Fiber Layer Loss in Glaucoma. Ophthalmology. 2009;116:1125–33.
11. Gordon MO, Beiser JA, Brandt JD, et al. The Ocular Hypertension Treatment Study: baseline factors that predict the onset of primary open-angle glaucoma. Arch Ophthalmol. 2002;120:714.

12. Bhan A, Browning AC, Shah S, et al. Effect of corneal thickness on intraocular pressure measurements with the pneumotonometer, Goldmann applanation tonometer, and Tono-Pen. Invest Ophthalmol Vis Sci. 2002;43:1389-92.
13. Kersey T, Clement CI, Bloom P, et al. New trends in glaucoma risk, diagnosis & management. Indian J Med Res. 2013;137:659–668.
14. Kapetanakis VV, Chan MPY, Foster PJ, et al. Global variations and time trends in the prevalence of primary open angle glaucoma (POAG): a systematic review and meta-analysis. Br J Ophthalmol. 2016;100:86–93.
15. Levene RZ. Low tension glaucoma: a critical review and new material. Surv Ophthalmol. 1980;24:621–664.
16. Flammer J, Orgül S, Costa VP, et al. The impact of ocular blood flow in glaucoma. Prog Retin Eye Res. 2002;21:359-93.
17. Cho HK, Lee J, Lee M, et al. Initial central scotomas vs peripheral scotomas in normal-tension glaucoma: clinical characteristics and progression rates. Eye. 2014;28:303–311.
18. Devereux JG, Foster PJ, Baasanhu J, et al. Anterior chamber depth measurement as a screening tool for primary angle-closure glaucoma in an East Asian population. Arch Ophthalmol. 2000;118:257-63.
19. Tamçelik N, Atalay E, Bolukbasi S, et al. Demographic features of subjects with congenital glaucoma. Indian J Ophthalmol. 2014;62:565–569.
20. Shen CC, Salim S, Du H, et al. Trabeculectomy versus Ahmed Glaucoma Valve implantation in neovascular glaucoma. Clin Ophthalmol. 2011;5:281–286.
21. Plateroti P, Plateroti AM, Abdolrahimzadeh S, et al. Pseudoexfoliation Syndrome and Pseudoexfoliation Glaucoma: A Review of the Literature with Updates on Surgical Management J Ophthalmol. 2015. 2015:370371.
22. Bao F, Huang Z, Huang J, et al. Clinical Evaluation of Methods to Correct Intraocular Pressure Measurements by the Goldmann ApplanationTonometer, Ocular Response Analyzer, and Corvis ST Tonometer for the Effects of Corneal Stiffness Parameters. J Glaucoma. 2015. [Epub ahead of print]
23. Gossman CA, Christie J, Webster MK, et al. Neuroprotective Strategies in Glaucoma. Curr Pharm Des. 2016. [Epub ahead of print]

24. Mastropasqua R, Agnifili L, Fasanella V, et al. Corneoscleral limbus in glaucoma patients: in vivo confocal microscopy and immunocytological study. Invest Ophthalmol Vis Sci. 2015;56:2050-8.
25. Wise JB, Witter SL. Argon laser therapy for open-angle glaucoma. A pilot study. Arch Ophthalmol. 1979.97:319-22.
26. Samples JR, Singh K, Lin SC, et al. Laser trabeculoplasty for open-angle glaucoma: a report by the american academy of ophthalmology. Ophthalmology. 2011;118:2296-302.
27. Latina MA, Sibayan SA, Shin DH, et al. Q-switched 532-nm Nd:YAG laser trabeculoplasty (selective laser trabeculoplasty): a multicenter, pilot, clinical study. Ophthalmology. 1998.105:2082-8.
28. Juzych MS, Chopra V, Banitt MR, et al. Comparison of long-term outcomes of selective laser trabeculoplasty versus argon laser trabeculoplasty in open-angle glaucoma. Ophthalmology. 2004;111:1853-9.
29. Kent SS, Hutnik CM, Birt CM, et al. A Randomized Clinical Trial of Selective Laser Trabeculoplasty Versus Argon Laser Trabeculoplasty in Patients With Pseudoexfoliation. J Glaucoma. 2013;24:344-7.
30. Holló G. Argon and low energy, pulsed Nd:YAG laser trabeculoplasty. A prospective, comparative clinical and morphological study. Acta Ophthalmol Scand. 1996;74:126-31.
31. Kramer TR, Noecker RJ. Comparison of the morphologic changes after selective laser trabeculoplasty and argon laser trabeculoplasty in human eye bank eyes. Ophthalmology. 2001;108:773-9.
32. Katz LJ, Steinmann WC, Kabir A, et al. Selective laser trabeculoplasty versus medical therapy as initial treatment of glaucoma: a prospective, randomized trial. J Glaucoma. 2012;21:460-8.
33. Dahan E, Ben Simon GJ, Lafuma A. Comparison of trabeculectomy and Ex-PRESS implantation in fellow eyes of the same patient: a prospective, randomised study. Eye. 2012; 26:703-10.
34. De Jong LA. The Ex-PRESS glaucoma shunt versus trabeculectomy in open-angle glaucoma: a prospective randomized study. Adv Ther. 2009;26:336-45.
35. Maris PJ, Ishida K, Netland PA. Comparison of trabeculectomy with Ex-PRESS miniature glaucoma device implanted under scleral flap. J Glaucoma. 2007;16:14-9.

36. Al Habash A, Aljasim LA, Owaidhah O, et al. A review of the efficacy of mitomycin C in glaucoma filtration surgery. Clin Ophthalmol. 2015;9:1945-51.
37. Buys YM. Trabeculectomy with ExPRESS: weighing the benefits and cost. Curr Opin Ophthalmol. 2013;24:111-8.
38. Saheb H, Ahmed II. Micro-invasive glaucoma surgery: current perspectives and future directions. Curr Opin Ophthalmol. 2012;23:96-104.
39. Salim S. Ex-PRESS glaucoma filtration device-surgical technique and outcomes. Int Ophthalmol Clin. 2011;51:83-94.
40. Peter A. Success and failure of glaucoma drainage implant surgery the ahmed glaucoma valve in neovascular glaucoma (an aos thesis). Trans Am Ophthalmol Soc. 2009;107:325-342.
41. Wamsley S, Moster MR, Rai S, et al. Results of the use of the Ex-PRESS miniature glaucoma implant in technically challenging, advanced glaucoma cases: a clinical pilot study. Am J Ophthalmol. 2004;138:1049–1051.
42. Traverso CE, de Feo F, Messas-Kaplan A, et al. Long term effect on IOP of a stainless steel glaucoma drainage implant (Ex-PRESS) in combined surgery with phacoemulsification. Br J Ophthalmol. 2005;89:425–429.
43. Dahan E, Carmichael TR. Implantation of a miniature glaucoma device under a scleral flap. J Glaucoma. 2005;14:98-102.
44. Good TJ, Kahook MY. Assessment of bleb morphologic features and postoperative outcomes after Ex-PRESS drainage device implantation versus trabeculectomy. Am J Ophthalmol. 2011;151:507-13.
45. Tavolato M, Babighian S, Galan A. Spontaneous extrusion of a stainless steel glaucoma drainage implant (Ex-PRESS). Eur J Ophthalmol. 2006;16:753-5.
46. Li JY, Lim MC, Mannis MJ. Traumatic cataract associated with mini glaucoma shunt. J Cataract Refract Surg. 2011;37:1360-2.
47. Teng CC, Radcliffe N, Huang JE, et al. Ex-PRESS glaucoma shunt dislocation into the anterior chamber. J Glaucoma. 2008;17:687-9.
48. Laing AE, Seibold LK, SooHoo JR, et al. Evaluation of bleb characteristics after implantation of the EX-PRESS™ glaucoma filtration device. Mol Vis. 2012;18:10-3.
49. Nyska A, Glovinsky Y, Belkin M, et al. Biocompatibility of the Ex-PRESS miniature glaucoma drainage implant. J Glaucoma. 2003;12:275-80.

50. Aziz H, Fantes F, Dubovy S. Histopathology of the Ex-PRESS Shunt. Ophthalmic Surg Lasers Imaging. 2011;42: 94-6.
51. De Feo F, Jacobson S, Nyska A, et al. Histological biocompatibility of a stainless steel miniature glaucoma drainage device in humans: a case report. Toxicol Pathol. 2009;37:512-6.
52. Ratner, B.; Hoffman, AS.; Schoen, FJ.; et al. Biomaterials science: an introduction to materials in medicine. 3rd Ed. Elsevier; London: 2012
53. Campoccia D, Montanaro L, Arciola CR. Biomaterials. 2006;27:2331–9.
54. Sampedro MF, Patel R. Infectious Disease Clinics of North America. 2007;21:785–819.
55. Hall–Stoodley L, Stoodley P. Evolving concepts in biofilm infections. Cell Microbiol. 2009; 11:1034–1043.
56. Sauer K. The genomics and proteomics of biofilm formation. Genome Biology. 2003; 4:219
57. Konig C, Schwank S, Blaser J. Factors compromising antibiotic activity against biofilms of Staphylococcus epidermidis. Eur J Clin Microbiol Infect Dis. 2001; 20:20–26.
58. Ballestrem C, Wehrle-Haller B, Hinz B, Imhof BA. Actin-dependent Lamellipodia Formation and Microtubule-dependent Tail Retraction Control-directed Cell Migration. Salmon T, ed. Molecular Biology of the Cell. 2000;11:2999-3012.
59. Raucher D, Sheetz MP. Cell Spreading and Lamellipodial Extension Rate Is Regulated by Membrane Tension. The Journal of Cell Biology. 2000;148:127-136.
60. Cukierman E, Pankov R, Stevens DR, Yamada KM. Taking cell-matrix adhesions to the third dimension. Science. 2001;294:1708-9
61. The spatial and temporal control of cell migration by nanoporous surfaces through the regulation of ERK and integrins in fibroblasts. Pan HA, Liang JY, Hung YC, et al. Biomaterials. 2013;34:841-53
62. Femtosecond laser treatment of 316L improves its surface nanoroughness and carbon content and promotes osseointegration: An in vitro evaluation. Kenar H, Akman E, Kacar E, Demir A, Park H, Abdul-Khaliq H, Aktas C, Karaoz E. Colloids Surf B Biointerfaces. 2013;108:305-12.

63. A mechanism for the enhanced attachment and proliferation of fibroblasts on anodized 316L stainless steel with nano-pit arrays. Ni S, Sun L, Ercan B, Liu L, Ziemer K, Webster TJ. J Biomed Mater Res B Appl Biomater. 2014;102:1297-303.
64. Precise identification of filtration openings on the scleral flap by three-dimensional anterior segment optical coherence tomography. Inoue T, Matsumura R, Kuroda U, Nakashima K, Kawaji T, Tanihara H. Invest Ophthalmol Vis Sci. 2012;53:8288-94
65. Effect of laser suture lysis on filtration openings: a prospective three-dimensional anterior segment optical coherence tomography study. Cho HK, Kojima S, Inoue T, Fukushima A, Kee C, Tanihara H. Eye. 2015;29:1220-5
66. Clinical applications of anterior segment optical coherence tomography. Lim SH.. J Ophthalmol. 2015;2015:605729
67. Filtering Blebs Using 3-Dimensional Anterior-Segment Optical Coherence Tomography. A Prospective Investigation. Kojima S, Inoue T, Nakashima K, Fukushima A, Tanihara H. JAMA Ophthalmol. 2015;133:148-56
68. Algebraic Formulation of Elastostatics: the Cell Method. Tonti E, Zarantonello F. Computer Modeling in Engineering & Science (CMES). 2009;39:201-236.
69. The Finite Elements Method, 4rd Edn. Zienkiewicz, OC. McGraw-Hill. 1977
70. Biofilm in implant infections: its production and regulation. Costerton JW, Montanaro L, Arciola CR. Int J Artif Organs. 2005;28:1062-8
71. Grafting of ionic liquids on stainless steel surface for antibacterial application. Pang LQ, Zhong LJ, Zhou HF, Wu XE, Chen XD. Colloids Surf B Biointerfaces. 2015;126:162-8
72. Corrosion degradation and prevention by surface modification of biometallic materials. Singh R, Dahotre NB. J Mater Sci Mater Med. 2007;18:725–751
73. Stainless steel in bone surgery. Disegi JA1, Eschbach L. Injury. 2000;31 Suppl 4:2-6.
74. Metals for Biomedical Applications. In Biomedical Engineering: from Theory to Applications. Hermawan H, Ramdan D, Djuansjah JRP. 2011 Fazel (Ed)
75. Preparation, characterization, and potential application of chitosan, chitosan derivatives, and chitosan metal nanoparticles in pharmaceutical drug delivery. Ahmed TA, Aljaeid BM. Drug Des Devel Ther. 2016;10:483-507
76. Application of carbohydrate polymers as corrosion inhibitors for metal substrates in different media: A review. Umoren SA, Eduok UM. Carbohydr Polym. 2016;140:314-41

77. Controlled delivery of stromal derived factor-1α from poly lactic-co-glycolic acid core-shell particles to recruit mesenchymal stem cells for cardiac regeneration. Zamani M, Prabhakaran MP, Thian ES, Ramakrishna S. J Colloid Interface Sci. 2015;451:144-52
78. Thiocarbonylthio Compounds [SdC(Ph)S-R] in Free Radical Polymerization with Reversible Addition-Fragmentation Chain Transfer (RAFT Polymerization). Role of the Free-Radical Leaving Group (R). Chong BYK, Krstina J, Le TPT, Moad G, Postma A, Rizzardo E, Thang SH; Macromolecules 2003;36:2256-2272
79. Thiocarbonylthio Compounds (SdC(Z)S-R) in Free Radical Polymerization with Reversible Addition-Fragmentation Chain Transfer (RAFT Polymerization). Effect of the Activating Group Z. Chiefari J, Mayadunne RTA, Moad CL, Moad G, Rizzardo E, Postma S, Skidmore MA, Thang SH; Macromolecules .2003;36:2273-2283
80. Biomedical applications of polymers derived by reversible addition – fragmentation chain-transfer (RAFT). Fairbanks BD, Gunatillake PA, Meagher L. Adv Drug Deliv Rev. 2015;91:141-52
81. Laboratory methods for studies of bacterial adhesion. Yuehuei H An, Friedman RJ. J Microbiol Methods.1997; 30:141 –152
82. The Influence of Scleral Flap Thickness, Shape, and Sutures on Intraocular Pressure (IOP) and Aqueous Humor Flow Direction in a Trabeculectomy Model. Samsudin AI, Eames I, Brocchini S, Khaw PT. J Glaucoma. 2015 Nov 10. [Epub ahead of print]
83. Computational Modeling of Fluid Flow and Intra-Ocular Pressure following Glaucoma Surgery. Gardiner BS1, Smith DW, Coote M, Crowston JG. PLoS One. 2010;5:1-11
84. Do shapes and dimensions of scleral flap and sclerostomy influence aqueous outflow in trabeculectomy? A finite element simulation approach. Tse KM, Lee HP, Shabana N, Loon SC, Watson PG, Thean SY. Br J Ophthalmol. 2012;96:432-7
85. Interfacial energetics of blood plasma and serum adsorption to a hydrophobic self-assembled monolayer surface. Krishnan A, Cha P, Liu YH, Allara D, Vogler EA. Biomaterials. 2006; 27:3187–3194.
86. Protein adsorption and human osteoblast-like cell attachment and growth on alkylthiol on gold self-assembled monolayers. Scotchford CA1, Gilmore CP, Cooper E, Leggett GJ, Downes S. J Biomed Mater Res. 2002;59:84-99.

87. Reduction of 3T3 Fibroblast Adhesion on SS316L by Methyl-Terminated SAMs. Raman A1, Gawalt ES. Mater Sci Eng C Mater Biol Appl. 2010;30:1157-1161.
88. Comparison of posterior capsule opacification with hydrophobic acrylic and hydrophilic acrylic intraocular lenses. Vasavada AR, Raj SM, Shah A, Shah G, Vasavada V, Vasavada V. J Cataract Refract Surg. 2011;37:1050-9
89. Collagen crosslinking of human and porcine sclera. Wollensak G, Spoerl E. J Cataract Refract Surg. 2004;30:689-95.
90. Increased resistance of crosslinked cornea against enzymatic digestion. Spoerl E, Wollensak G, Seiler T. Curr Eye Res. 2004;29:35-40.
91. Nonlinear material properties of intact cornea and sclera. Woo SL, Kobayashi AS, Schlegel WA, Lawrence C. Exp Eye Res. 1972;14:29-39.
92. Analysis of the corneo-scleral shell by the method of direct stiffness. Kobayashi AS, Woo SL, Lawrence C, Schlegel WA. J Biomech. 1971;4:323-30.
93. Experimental surface strain mapping of porcine peripapillary sclera due to elevations of intraocular pressure. Girard MJ, Downs JC, Burgoyne CF, Suh JK. J Biomech Eng. 2008;130:041017
94. Measurements of the compressive properties of scleral tissue. Battaglioli JL, Kamm RD. Invest Ophthalmol Vis Sci. 1984;25:59-65.
95. Biaxial mechanical testing of human sclera. Eilaghi A, Flanagan JG, Tertinegg I, Simmons CA, Wayne Brodland G, Ross Ethier C. J Biomech. 2010;43:1696-701
96. Numerical Study of the Turbulent Flow Past an Airfoil with Trailing Edge Separation. Rhie CM, Chow W L. AIAA Journal. 1983;21:1525-35.

Acknowledgements

SEM
Gianluca Turco, PhD
Department of Medicine, Surgery and Health Sciences, University of Trieste

Grinding Procedure
Prof. Vanni Lughi
Department of Engineering and Architecture, University of Trieste

Hydrodynamic
Luigino Zovatto and Prof. Gianni Pedrizzetti
Department of Engineering and Architecture, University of Trieste

Cell adhesion
Alessio Polacchini, PhD and Prof. Enrico Tongiorgi
Department of Life Sciences, University of Trieste

Nanocoating
Prof. Roberto Simonutti and Daniele Melodia
Department Of Materials Science, University of Milano-Bicocca

Bacteria adhesion and vitality
Monica Benincasa, PhD
Department of Life Sciences, University of Trieste

Unconditional support
Rossella D'Aloisio, MD
Eye Clinic, Department of Medicine, Surgery and Health Sciences, University of Trieste